



**UNIVERSITY OF IOANNINA**  
**FACULTY OF SCIENCES**  
**DEPARTMENT OF PHYSICS**

**Ultrafine texture of Cu-Zr Metallic Glass**  
**microstructure**

George A. Almyras

**PhD THESIS**

2014



**UNIVERSITY OF IOANNINA**  
**FACULTY OF SCIENCES**  
**DEPARTMENT OF PHYSICS**

**Ultrafine texture of Cu-Zr Metallic Glass**  
**microstructure**

George A. Almyras

**PhD THESIS**

2014

«Η έγκριση της διδακτορικής διατριβής από το Τμήμα Φυσικής της Σχολής Θετικών  
Επιστημών, του Πανεπιστημίου Ιωαννίνων δεν υποδηλώνει αποδοχή των  
γνωμών του συγγραφέα Ν. 5343/32, άρθρο 202, παράγραφος 2»

**ΠΡΑΚΤΙΚΟ**  
**ΔΗΜΟΣΙΑΣ ΠΑΡΟΥΣΙΑΣΗΣ, ΕΞΕΤΑΣΗΣ ΚΑΙ ΑΞΙΟΛΟΓΗΣΗΣ**  
**ΔΙΔΑΚΤΟΡΙΚΗΣ ΔΙΑΤΡΙΒΗΣ**

Σήμερα Τρίτη **10-09-2014**, ώρα **12.00** στην αίθουσα **Σεμιναρίων του Τμήματος Φυσικής, κτίριο Φ2**, του Πανεπιστημίου Ιωαννίνων, πραγματοποιήθηκε, σύμφωνα με το άρθρο 12, παρ. 5 του Ν.2083/92, η διαδικασία της δημόσιας παρουσίασης, εξέτασης και αξιολόγησης της εργασίας του υποψήφιου για την απόκτηση Διδακτορικής Διατριβής **κ. Γεωργίου Αλμύρα**.

Την Επταμελή Εξεταστική Επιτροπή, που συγκροτήθηκε με απόφαση της Γενικής Συνέλευσης Ειδικής Σύνθεσης του Τμήματος Φυσικής (συν. 441/23-6-2014), αποτελούν τα ακόλουθα μέλη:

- 1) Γεώργιος Ευαγγελάκης, Καθηγητής του Τμήματος Φυσικής του Παν/μίου Ιωαννίνων (Επιβλέπων)
- 2) Κώνστος Κοσμίδης, Καθηγητής του Τμήματος Φυσικής του Παν/μίου Ιωαννίνων
- 3) Θωμάς Μπάκας, Καθηγητής του Τμήματος Φυσικής του Παν/μίου Ιωαννίνων
- 4) Αλέξανδρος Δούβαλης, Επίκουρος Καθηγητής του Τμήματος Φυσικής του Παν/μίου Ιωαννίνων
- 5) Δημήτριος Βλάχος, Επίκουρος Καθηγητής του Τμήματος Φυσικής του Παν/μίου Ιωαννίνων
- 6) Χριστίνα Λέκκα, Επίκουρος Καθηγήτρια του Τμήματος Μηχανικών Υλικών του Παν/μίου Ιωαννίνων
- 7) Δημήτριος Παπαγεωργίου, Αναπληρωτής Καθηγητής του Τμήματος Μηχανικών Υλικών του Παν/μίου Ιωαννίνων

Παρόντα ήταν τα 6 μέλη της εξεταστικής επιτροπής. Ο κ. Κοσμίδης απουσίαζε λόγω σοβαρού οικογενειακού προβλήματος, όμως δήλωσε ότι γνωρίζει την εργασία του υποψηφίου καθώς και τη διατριβή του και ότι είναι άρτιες. Το θέμα της διδακτορικής διατριβής που εκπόνησε ο κ. Αλμύρας και που παρουσίασε σήμερα είναι **«Υπέρλεπτη υφή της μικροδομής μεταλλικών υάλλων Cu-Zr»**

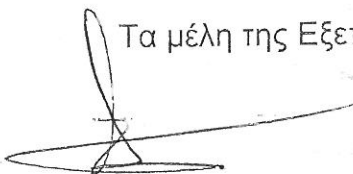
Ο υποψήφιος παρουσίασε και ανάπτυξε το θέμα και απάντησε σε σχετικές ερωτήσεις τόσο των μελών της εξεταστικής επιτροπής όσο και του ακροατηρίου. Στη συνέχεια αποσύρθηκε η εξεταστική επιτροπή και μετά από συζήτηση κατέληξε στα ακόλουθα:

- α) Η συγγραφή της διατριβής έγινε με τρόπο που δείχνει ιδιαίτερη μεθοδικότητα και πλήρη ενημέρωση του υποψήφιου πάνω στη σχετική βιβλιογραφία.
- β) Η ερευνητική εργασία καταλήγει σε σημαντικά αποτελέσματα τα οποία προάγουν την επιστήμη. Από την εργασία αυτή έχουν προκύψει επτά εργασίες δημοσιευμένες σε έγκριτα επιστημονικά και επτά ανακοινώσεις σε διεθνή συνέδρια που έγιναν από τον υποψήφιο.
- γ) Η παρουσίαση και ανάπτυξη του θέματος της εργασίας από τον υποψήφιο και οι εύστοχες απαντήσεις στις ερωτήσεις που του τέθηκαν έδειξαν πλήρη γνώση του θέματος και γενικότερων σχετικών θεμάτων.

Με βάση τα ανωτέρω, τα μέλη της Επταμελούς Εξεταστικής Επιτροπής εγκρίνουν ομόφωνα την εργασία και εισηγούνται ανεπιφύλακτα την απονομή Διδακτορικού Διπλώματος στον κ. Γεώργιο **Αλμύρα** με βαθμό **ΑΡΙΣΤΑ**

Τα μέλη της Εξεταστικής Επιτροπής

Γεώργιος Ευαγγελάκης



Κων/νος Κοσμίδης

Θωμάς Μπάκας



Αλέξανδρος Δούβαλης



Δημήτριος Βλάχος



Χριστίνα Λέκκα



Δημήτριος Παπαγεωργίου



**Ένταξη του κ. ...Γεωργίου Α. Αλμύρα... από τη Γ.Σ.Ε.Σ.: ..371../..23../..06../..2010..**

Ορισμός Τριμελούς Συμβουλευτικής Επιτροπής από τη Γ.Σ.Ε.Σ.:

**..380../..20../..12../..2010..**

**Μέλη Τριμελούς Συμβουλευτικής Επιτροπής:**

Επιβλέπων:

**Γεώργιος Ευαγγελάκης**, Καθηγητής Φυσικού, Πανεπιστήμιο Ιωαννίνων

Μέλη:

**Δημήτριος Παπαγεωργίου**, Αν. Καθηγητής ΤΜΕΥ, Πανεπιστήμιο Ιωαννίνων

**Χριστίνα Λέκκα**, Επ. Καθηγήτρια ΤΜΕΥ, Πανεπιστήμιο Ιωαννίνων

Ορισμού θέματος από τη Γ.Σ.Ε.Σ.: **..405../..19../..06../..2012..**

**Θέμα: «...Υπέρλεπτη υφή της μικροδομής μεταλλικών υάλων Cu-Zr...»**

**ΟΡΙΣΜΟΣ ΕΠΤΑΜΕΛΟΥΣ ΕΞΕΤΑΣΤΙΚΗΣ ΕΠΙΤΡΟΠΗΣ από τη Γ.Σ.Ε.Σ.:**

**..441../..23../..06../..2014..**

- 1...**Γεώργιος Ευαγγελάκης**, Καθηγητής Φυσικού, Πανεπιστήμιο Ιωαννίνων.....
- 2...**Κωνσταντίνος Κοσμίδης**, Καθηγητής Φυσικού, Πανεπιστήμιο Ιωαννίνων.....
- 3...**Θωμάς Μπάκας**, Καθηγητής Φυσικού, Πανεπιστήμιο Ιωαννίνων .....
- 4...**Αλέξιος Δούβαλης**, Επ. Καθηγητής Φυσικού, Πανεπιστήμιο Ιωαννίνων.....
- 5...**Δημήτριος Βλάχος**, Επ. Καθηγητής Φυσικού, Πανεπιστήμιο Ιωαννίνων .....
- 6...**Χριστίνα Λέκκα**, Επ. Καθηγήτρια ΤΜΕΥ, Πανεπιστήμιο Ιωαννίνων.....
- 7...**Δημήτριος Παπαγεωργίου**, Αν. Καθηγητής ΤΜΕΥ, Πανεπιστήμιο Ιωαννίνων..

**Έγκριση Διδακτορικής Διατριβής με βαθμό «...ΑΡΙΣΤΑ...» στις ..10../..09../..2014..**

**Ο Πρόεδρος του Τμήματος Φυσικής  
Ιωάννης Ρίζος**

**Η Γραμματέας του Τμήματος  
Ελένη Νικολάκη**

## CONTENTS TABLE:

<b>ABSTRACT</b> .....	<b>8</b>
<b>ΠΕΡΙΛΗΨΗ</b> .....	<b>9</b>
<b>ACKNOWLEDGMENTS</b> .....	<b>10</b>
<b>1 STATE OF ART</b> .....	<b>11</b>
1.1 THE HISTORY OF METALLIC GLASSES .....	11
1.2 APPLICATIONS OF THE METALLIC GLASSES .....	17
1.3 CRITERIA AND PROPERTIES OF THE METALLIC GLASSES .....	18
1.4 CHARACTERISTICS OF THE METALLIC GLASSES .....	30
1.5 STUDY OF THE Cu-Zr SYSTEM.....	37
<b>2 SIMULATION TECHNIQUES</b> .....	<b>40</b>
2.1 AB INITIO.....	41
2.2 MONTE CARLO .....	42
2.3 MOLECULAR DYNAMICS.....	42
2.3.1 MATHEMATICAL ANALYSIS OF MD .....	44
2.3.2 POTENTIAL MODEL BASED ON THE TIGHT BINDING SCHEME IN SECOND MOMEND APPROXIMATION .....	47
2.4 SYSTEMS PREPARATION .....	48
<b>3 STRUCTURAL STUDY OF THE SYSTEMS</b> .....	<b>50</b>
3.1 RADIAL DISTRIBUTION FUNCTION (RDF).....	50
3.2 COORDINATION NUMBER (CN).....	52
3.3 COMMON NEIGHBOR ANALYSIS (CNA) .....	53
3.4 HIGH SYMMETRY CENTERS .....	54
<b>4 RESULTS</b> .....	<b>57</b>
4.1 THE BASIC STRUCTURAL CHARACTERISTICS OF Cu-Zr .....	57
4.2 ON THE ROLE OF ICO-LIKE CLUSTERS IN THE SOLIDIFICATION AND THE MECHANICAL RESPONSE OF Cu-Zr MGs.....	64
4.3 ON THE DEPOSITION MECHANISMS AND THE FORMATION OF GLASSY Cu-Zr THIN FILMS.....	68
4.4 MICROSTRUCTURAL DIFFERENCES OF AMORPHOUS $Cu_{65}Zr_{35}$ BETWEEN RAPIDLY QUENCHED AND TOPOLOGICALLY DESTABILIZED CRYSTALLINE Cu AND Zr METALS.....	81
4.5 ANALYSIS ON THE MICRO-STRUCTURE OF $Cu_x-Zr_{(100-x)}$ , $x=65,35$ .....	88
4.6 EXTENDED ATOMIC CLUSTER ARRANGEMENTS OF Cu-Zr.....	95
4.7 THE MD MICRO-STRUCTURE ANALYSIS OF Cu-Zr USING EXAFS.....	102

4.8	CLUSTERING, MICROALLOYING AND MECHANICAL PROPERTIES IN Cu-Zr BY MD AND AB-INITIO CALCULATIONS .....	112
<b>5</b>	<b>CONCLUSIONS AND PERSPECTIVES .....</b>	<b>120</b>
5.1	CONCLUSIONS.....	120
5.2	PERSPECTIVES .....	125
	<b>REFERENCES.....</b>	<b>126</b>

## **ABSTRACT**

This work is dedicated in the investigation of the fine details of the microstructure of Metallic Glasses. The study was conducted mainly by means of Molecular Dynamic Simulations on several compositions of Cu-Zr Bulk Metallic Glasses, in comparison with experimental data, revealing their properties dependency with the existence of several Icosahedral-like clusters.

The study comprises the exploration of the microstructure evolution under three different vitrification techniques; rapid quenching, thin film deposition and mechanical alloying. The Cu-Zr Metallic Glasses were analysed during every vitrification procedure and the formation of the Icosahedral-like clusters was investigated revealing their importance on the Glass Forming Ability of the Cu-Zr systems.

Furthermore, the Icosahedral-like clusters were found to be usually distorted and interpenetrated while when the stoichiometry of these nanostructures obeyed the system's composition their size followed a sequence of magic numbers named therefore SuperClusters. It came out that these structural units embrace all the details of the microstructure of every system reflecting its ultrafine texture and thus, they can be considered as the basic structural units of the Metallic Glasses reflecting their Short and Medium Range Order. Finally, the creation and reconstruction of the Icosahedral-like clusters and the SuperClusters was found to be the way the system accommodated the stress upon deformation.

The results of the present PhD thesis can be used for the design of Metallic Glasses suitable for many technological applications.

## ΠΕΡΙΛΗΨΗ

Η εργασία αυτή είναι αφιερωμένη στην υπέρλεπτη υφή της μικροδομής των μεταλλικών υάλων. Η μελέτη έγινε κυρίως με τη βοήθεια προσομοιώσεων Μοριακής Δυναμικής διαφόρων στοιχειομετριών Cu-Zr, σε σύγκριση με πειραματικά δεδομένα, αποκαλύπτοντας την εξάρτηση των ιδιοτήτων τους με την ύπαρξη πληθώρας νανοδομών Εικοσαεδρικού τύπου.

Η μελέτη συμπεριλαμβάνει τη διερεύνηση της εξέλιξης της μικροδομής κατά την υαλοποίηση με τρεις διαφορετικές τεχνικές: με γρήγορη ψύξη υγρού, με εναπόθεση αερίου και με μηχανική κραματοποίηση. Τα μεταλλικά γυαλιά Cu-Zr αναλύθηκαν κατά τη διάρκεια κάθε τεχνικής υαλοποίησης και διερευνήθηκε ο σχηματισμός των Εικοσαεδρικού τύπου νανοδομών αποκαλύπτοντας τον πολύ σημαντικό ρόλο τους ως προς την δυνατότητα υαλοποίησης των συστημάτων Cu-Zr.

Επιπλέον, οι Εικοσαεδρικού τύπου νανοδομές βρέθηκαν να είναι συνήθως παραμορφωμένες και διεισδύοντες ενώ όταν η στοιχειομετρία αυτών των μικροδομών απαντούσε τη στοιχειομετρία του συστήματος το μέγεθος τους ακολουθούσε μία ακολουθία μαγικών αριθμών κι ονομάστηκαν ως Υπερσυσσωματώματα. Αποδείχθηκε ότι αυτές οι δομικές μομάδες εμπεριέχουν όλες τις λεπτομέρειες της μικροδομής του εκάστοτε συστήματος και μπορούν να θεωρούνται ως η βασική δομική μονάδα των Μεταλλικών Γυαλιών, αντανακλώντας τη Τάξη Κοντινής και Μεσαίας Εμβέλειας. Τελικά, η δημιουργία και επαναδημιουργία των Εικοσαεδρικού τύπου νανοδομών και των Υπερσυσσωματωμάτων βρέθηκε να είναι ο τρόπος με τον οποίο το σύστημα απορροφάει την εξωτερικά εφαρμοζόμενη παραμόρφωση.

Τα αποτελέσματα της παρούσας Διδακτορικής Διατριβής μπορούν να χρησιμοποιηθούν στο σχεδιασμό Μεταλλικών Γυαλιών κατάλληλων για πληθώρα τεχνολογικών εφαρμογών.

## ACKNOWLEDGMENTS

Finishing my PhD is the best time to express my gratitude at some very special persons in my life. Starting by my supervisor, Prof. Evangelakis, I have to point him as my mentor in my research and personal life as well. Working together for almost 8 years, he is the basic contributor to my work and I own him the most of my progress in the area of physics. Furthermore, he is one of the closest people to me being very supportive and a great consulter in my life.

Continuing, I have to acknowledge the valuable contribution in my research of Assoc. Prof. Papageorgiou and Assist. Prof. Lekka and moreover, they always provide me their motivating assistance as my supervisors.

Additionally, I would like to thank the other members of the jury, Prof. Kosmidis, Prof. Bakas, Assist. Prof. Vlachos and Assist. Prof. Douvalis, as they have been a great inspiration during my studies at Physics department of Ioannina and I am honoured as they are participating in my PhD defence committee.

Following, I could not forget my friends that were always there to support and encourage me. Elena, Marios, Stelios, Giannis, Mitsos, Ioanna, Loukas, Ourania, Pavlos, and of course Alex with whom we worked together at the same lab all these last years and she has been the most supportive co-worker and a great friend of mine.

Finishing I have to express my special gratitude to my family; my parents, Efi and Angelos and my sisters, Elena, Stella and Maria. Their support is the first ingredient of everything I have achieved in my life. Ευτυχούλα μου και Άγγελε μου είσαστε η αρχή, η μέση και το τέλος όλης αυτής της προσπάθειας. Τα λόγια δεν αρκούν για να περιγράψουν όλα όσα σας οφείλω. Σας ευχαριστώ από την ψυχή μου για όλη σας τη στήριξη και φροντίδα που μου παρέχεται και σας αφιερώνω από καρδιάς το διδακτορικό μου.

# 1 STATE OF ART

## 1.1 THE HISTORY OF METALLIC GLASSES

Metallic amorphous alloys are relatively new materials.  $\text{Au}_{75}\text{Si}_{25}$  is the first alloy reported to be made into glassy state by Duwez in 1960 [1]. He solidified metallic alloys by rapid quenching techniques at very high rates of  $10^5$ – $10^6$  K/s bypassing the process of nucleation and growth of crystalline phase to yield a super-cooled liquid, that is, metallic glass (MG). The studies on metallic glasses have attracted increasing attention because of their fundamental scientific importance and engineering potential applications [2–5]. In the early 1970s and 1980s the continuous casting processes for commercial manufacture of metallic glasses ribbons, wires, and sheets [5] was developed resulting in a significant increase of academic and industrial research in that period. However, the geometry of casted MGs was limited to thin sheets and wires basically due to the high cooling rates restrictions, thus reducing significantly the range of MGs' applications.

Metallic glasses have many similarities with other non-metallic glasses such as silicates, ceramic glasses, and polymers. Turnbull and co-worker showed that a glass transition manifested in conventional glass-forming melts could also be observed in rapid quenched metallic glasses [6,7]. The glass transition was found to occur at a rather well-defined temperature, which varied only slightly as the heating rate was changed [8]. Moreover, Turnbull predicted that the ratio of the glass transition temperature  $T_g$  to the melting point  $T_m$  of an alloy, referred to as the reduced glass transition temperature  $T_{rg} = T_g/T_m$ , can be used as a criterion for determining its glass-forming ability (GFA) [9]. According to Turnbull's criterion [10], a liquid with  $T_g/T_m = 2/3$  can be easily made to glassy state because it can crystallize only within a very narrow temperature range. Turnbull criterion

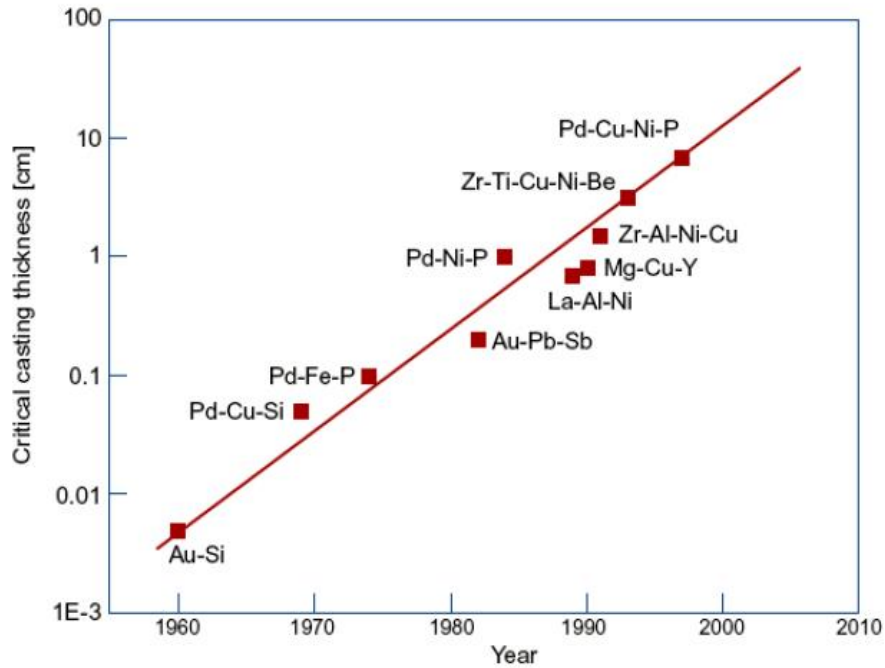
for the suppression of crystallization in undercooled melts has played a key role for predicting the GFA of any liquid [11] contributing in the development of various MGs including bulk metallic glasses (BMGs).

The first bulk metallic glass was the ternary Pd–Cu–Si alloy, prepared by Chen in 1974 [12]. In 1982, Turnbull and co-workers [13,14] used boron oxide fluxing method in order to purify the melt and to eliminate heterogeneous nucleation. They successfully prepared the Pd–Ni–P BMG and the fluxing experiments showed that the value of  $T_{rg}$  of the alloy could reach 2/3 when the heterogeneous nucleation was suppressed, allowing centimetre sized bulk glass ingot to be solidified at low the cooling rate of 10K/s. Despite the high cost of Pd metal this finding led to an increased research for developing new BMG systems. In 1980s, a variety of new techniques, such as mechanical alloying, diffusion induced amorphization in multilayers, ion beam mixing, hydrogen absorption, and inverse melting, have been developed [3]. A variety of metallic glasses in the form of thin films, or powders were obtained by interdiffusion and interfacial reaction at temperatures well below the glass transition temperatures. In late 1980s, Inoue et al. observed exceptional GFA at lower critical cooling rates in alloy systems consisting mainly of common metallic elements, for example the rare-earth-based alloys La–Al–Ni and La–Al–Cu [15,16]. By casting the alloy melt in water-cooling Cu moulds, they obtained fully glassy rods and bars of several millimetres thick. Based on this work, the researchers developed similar quaternary and quinary amorphous alloys (e.g. La–Al–Cu–Ni and La–Al–Cu–Ni–Co BMGs) at cooling rates below 100K/s and the critical casting thicknesses could reach several centimetres [17]. Some similar alloys with rare-earth metals partially replaced by the alkali-earth metal Mg, such as Mg–Y–Cu, Mg–Y–Ni, etc., were also developed [18], along with a family of multicomponent Zr-based BMGs (e.g. Zr–Cu–Ni, Zr–Cu–Ni–Al BMGs) [19].

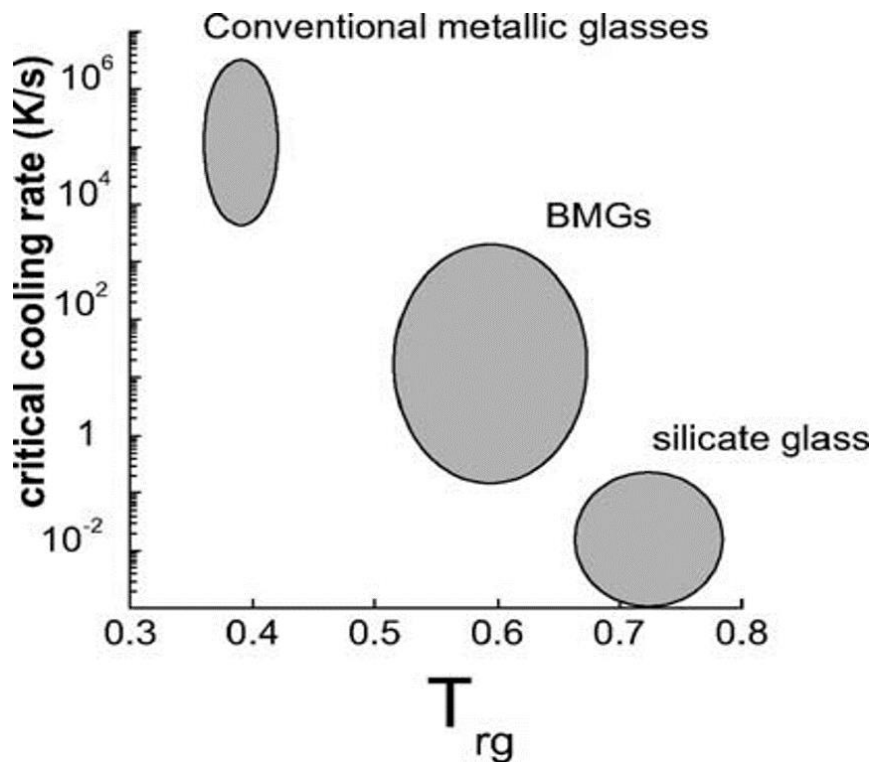
At present, the lowest critical cooling rate for BMG formation is about 0.10 K/s for the  $\text{Pd}_{40}\text{Cu}_{30}\text{Ni}_{10}\text{P}_{20}$  alloy and the maximum sample thickness is about 10 cm [20], while the  $(\text{Zr}_{82.5}\text{Ti}_{17.5})_{55}(\text{Ni}_{54}\text{Cu}_{46})_{18.75}\text{Be}_{26.25}$  alloy exhibits the largest Super-cooled Liquid Region (ScLR), which is 135 K [11]. The design of the Zr-Ti-Cu-Ni-Be glass forming alloy family was an important progress made by Peker and Johnson [21]. Vitolloy 1 (vit1), the most extensively studied BMG in the family, has the composition of  $\text{Zr}_{41}\text{Ti}_{14}\text{Cu}_{12.5}\text{Ni}_{10}\text{Be}_{22.5}$ . It has critical cooling rates for glass formation in the 1K/s range and the alloy can be casted in Cu-mould in the form of fully glassy rods with diameters ranging up to 5–10 cm. The formation of the BMGs in this family requires no fluxing or special processing treatments and can form bulk glass by conventional metallurgical casting methods. Moreover, its GFA and processability are comparable to that of many silicate glasses. This finding makes possible the processing of metallic glasses by common methods [11]. Due to their high thermal stability and superb properties, BMGs have considerable potentials as advanced engineering materials. In fact, the Zr-based BMGs found applications in industries only 3 years after their invention.

Fig. 1 shows the critical casting thickness as a function of the year in which the corresponding alloy was developed. Starting with the first metallic glass, the thickness increased by more than three orders of magnitude in the last 40 years. A fit to the data shows that it tends to increase by one order of magnitude approximately every 12 years. Moreover, table 1 lists the typical BMG systems and the year in which they were first reported. It is apparent that the BMGs were developed in the sequence beginning with the expensive metallic-based Pd, Pt and Au, followed by less expensive Zr-, Ti-, Ni- and Ln-based BMGs and then by much cheaper Fe- and Cu-based BMGs that attracted extensive interests. Furthermore, Fig. 2 shows a comparison of GFA of various glasses and one can clearly see

that some excellent bulk glass formers have GFA very close to that of silicate glasses. Table 2 lists thermal parameters and GFA represented by  $T_{rg}$  of typical BMGs.



**Figure 1.** Critical casting thickness for glass formation as a function of the year the corresponding alloys have been discovered.



**Figure 2.** A comparison of critical cooling rates and reduced glass transition temperature  $T_{rg}$  for BMG, silicate glasses and conventional metallic glasses.

**Table 1** - [22]

Bulk metallic glasses and their developed year

<b>BMG system</b>	<b>Year</b>
Pd-Cu-Si	1974
Pt-Ni-P	1975
Au-Si-Ge	1975
Pd-Ni-P	1982
Mg- <i>Ln</i> -Cu ( <i>Ln</i> = lanthanide metal)	1988
<i>Ln</i> -Al- <i>TM</i> ( <i>TM</i> = transition metal)	1989
Zr-Ti-Al- <i>TM</i>	1990
Ti-Zr- <i>TM</i>	1993
Zr-Ti-Cu-Ni-Be	1993
Nd(Pr)-Al-Fe-Co	1994
Zr-(Nb,Pd)-Al- <i>TM</i>	1995
Cu-Zr-Ni-Ti	1995
Fe-(Nb,Mo)-(Al,Ga)-(P,C,B,Si,Ge)	1995
Pd-Cu(Fe)-Ni-P	1996
Co-(Al,Ga)-(P,B,Si)	1996
Fe-(Zr,Hf,Nb)-B	1996
Co-Fe-(Zr,Hf,Nb)-B	1996
Ni-(Zr,Hf,Nb)-(Cr,Mo)-B	1996
Ti-Ni-Cu-Sn	1998
La-Al-Ni-Cu-Co	1998
Ni-Nb	1999
Ni-(Nb,Cr,Mo)-(P,B)	1999
Zr-based glassy composites	1999
Zr-Nb-Cu-Fe-Be	2000
Fe-Mn-Mo-Cr-C-B	2002
Ni-Nb-(Sn,Ti)	2003
Pr(Nd)-(Cu,Ni)-Al	2003

In the recent years some very simple binary alloys such as Ca-Al [23], Pd-Si [24], Cu-Zr [25-27] and Cu-Hf [26] BMGs with diameter up to 2 mm were produced. The results show that such alloys could exhibit unusual high GFA. However, the physical origin of the unexpectedly high GFA and the formation mechanisms of binary BMGs appear to be different from that of multicomponent BMG alloys and remains unclear so far. This remark is important because it suggests that there are many potential BMG-forming alloys to be discovered. These results also demonstrate that the empirical criteria (which are presented in the next chapter) requiring multi-components alloys with at least three components are no longer a necessary prerequisite for designing BMGs. Based on these developments, new BMGs with good glass forming abilities could be developed by means of minor additions in simple binary BMG-forming alloys. Therefore, from an engineering point of view, this

finding might provide important guidance to the research of extremely good GFA and could improve considerably the efficiency of alloy development. Furthermore, from a fundamental point of view, the simple BMGs are ideal models for the study of some longstanding issues in glasses. Modelling and computer simulation became readily tractable because of the simplicity of these alloys and the good GFA for the feasibility of making usable samples.

**Table 2** - [22]

Composition of representative BMG systems, their glass transition temperature,  $T_g$ , onset temperature of crystallization,  $T_x$ , and onset melting point,  $T_m$ , and glass-forming ability represented by the reduced glass transition temperature,  $T_{rg}$

<b>BMG</b>	<b><math>T_g</math> (K)</b>	<b><math>T_x</math> (K)</b>	<b><math>T_m</math> (K)</b>	<b><math>T_{rg}</math></b>
Mg <sub>65</sub> Ni <sub>20</sub> Nd <sub>15</sub>	459.3	501.4	743.0	0.62
Mg <sub>75</sub> Ni <sub>15</sub> Nd <sub>10</sub>	450.0	482.8	717.0	0.63
Mg <sub>65</sub> Cu <sub>25</sub> Y <sub>10</sub>	424.5	484.0	727.9	0.58
Zr <sub>41.2</sub> Ti <sub>13.8</sub> Cu <sub>12.5</sub> Ni <sub>10</sub> Be <sub>22.5</sub>	623.0	705.0	932.0	0.67
Zr <sub>46.75</sub> Ti <sub>8.25</sub> Cu <sub>7.5</sub> Ni <sub>10</sub> Be <sub>27.5</sub>	622.0	727.0	909.0	0.68
Zr <sub>57</sub> Ti <sub>5</sub> Al <sub>10</sub> Cu <sub>20</sub> Ni <sub>8</sub>	676.7	725.4	1095.3	0.62
Zr <sub>53</sub> Ti <sub>5</sub> Cu <sub>16</sub> Ni <sub>10</sub> Al <sub>16</sub>	697.0	793.0	1118.0	0.62
Zr <sub>66</sub> Al <sub>8</sub> Cu <sub>7</sub> Ni <sub>19</sub>	662.3	720.7	1117.3	0.59
Zr <sub>66</sub> Al <sub>8</sub> Ni <sub>26</sub>	672.0	707.6	1188.5	0.57
Zr <sub>65</sub> Al <sub>7.5</sub> Cu <sub>17.5</sub> Ni <sub>10</sub>	656.5	735.6	1108.6	0.59
Pd <sub>40</sub> Ni <sub>40</sub> P <sub>20</sub>	590.0	671.0	877.3	0.67
Pd <sub>81.5</sub> Cu <sub>2</sub> Si <sub>16.5</sub>	633.0	670.0	1008.8	0.63
Pd <sub>40</sub> Cu <sub>30</sub> Ni <sub>10</sub> P <sub>20</sub>	586.0	678.0	744.8	0.79
Pd <sub>77.5</sub> Cu <sub>6</sub> Si <sub>16.5</sub>	637.0	678.0	1019.4	0.62
Pd <sub>42.5</sub> Cu <sub>27.5</sub> Ni <sub>10</sub> P <sub>20</sub>	572.0	666.0	752.0	0.76
Cu <sub>60</sub> Zr <sub>30</sub> Ti <sub>10</sub>	713.0	763.0	1110.0	0.64
Cu <sub>54</sub> Zr <sub>27</sub> Ti <sub>9</sub> Be <sub>10</sub>	720.0	762.0	1090.0	0.66
Cu <sub>60</sub> Zr <sub>20</sub> Hf <sub>10</sub> Ti <sub>10</sub>	754.0	797.0	1189.0	0.63
La <sub>66</sub> Al <sub>14</sub> Cu <sub>20</sub>	395.0	449.0	681.9	0.58
La <sub>55</sub> Al <sub>25</sub> Ni <sub>20</sub>	490.8	555.1	711.6	0.69
La <sub>55</sub> Al <sub>25</sub> Ni <sub>10</sub> Cu <sub>10</sub>	467.4	547.2	662.1	0.71
La <sub>55</sub> Al <sub>25</sub> Cu <sub>20</sub>	455.9	494.8	672.1	0.68
La <sub>55</sub> Al <sub>25</sub> Ni <sub>5</sub> Cu <sub>10</sub> Co <sub>5</sub>	465.2	541.8	660.9	0.70
Nd <sub>60</sub> Al <sub>10</sub> Cu <sub>10</sub> Fe <sub>20</sub>	485.0	610.0	773.0	0.63
Nd <sub>60</sub> Al <sub>15</sub> Ni <sub>10</sub> Cu <sub>10</sub> Fe <sub>5</sub>	430.0	475.0	709.0	0.61
Nd <sub>61</sub> Al <sub>11</sub> Ni <sub>8</sub> Co <sub>5</sub> Cu <sub>15</sub>	445.0	469.0	729.0	0.61
Ti <sub>34</sub> Zr <sub>11</sub> Cu <sub>47</sub> Ni <sub>8</sub>	698.4	727.2	1119.0	0.62
Ti <sub>50</sub> Ni <sub>24</sub> Cu <sub>20</sub> B <sub>1</sub> Si <sub>2</sub> Sn <sub>3</sub>	726.0	800.0	1230.0	0.59
Au <sub>77.8</sub> Si <sub>8.4</sub> Ge <sub>13.8</sub>	293.0	293.0	606.0	0.48
Pr <sub>60</sub> Cu <sub>20</sub> Ni <sub>10</sub> Al <sub>10</sub>	409.0	452.0	705.0	0.58
Pr <sub>55</sub> Al <sub>12</sub> Fe <sub>30</sub> Cu <sub>3</sub>	551.0	626.0	845.0	0.65

## 1.2 APPLICATIONS OF THE METALLIC GLASSES

As we are going to see later, BMGs exhibit unique and unconventional characteristics making them suitable materials for applications in various fields. One of the great advantages of BMGs is the ease of formation of complicated shapes. Up to now, BMGs have already been used as die materials (Pd–Cu–Ni–P BMG), sporting equipment (Zr–Ti–Cu–Ni–Be and Zr–Ti–Ni–Cu BMGs) and electrode materials (Pd–Cu–Si–P BMG). The development of Fe-based BMGs has reached the final stage for application as soft magnetic materials for common mode choke coils. Success in this area will result in the increasing importance of BMGs in engineering. Table 3 summarizes some of the present and future potential applications of the BMGs.

**Table 3** - [22]  
Possible application fields for BMGs

<b>Properties</b>	<b>Application field</b>
High strength	Machinery structural materials
High hardness	Cutting materials
High fracture toughness	Die materials
High impact fracture energy	Tool materials
High fatigue strength	Bonding materials
High elastic energy	Sporting goods materials
High corrosion resistance	Corrosion resistance materials
High wear resistance	Writing appliance materials
High reflection ratio	Optical precision materials
Good soft magnetism	Soft magnetic materials
High frequency permeability	High magnetostrictive materials
Efficient electrode	Electrode materials
High viscous flowability	Composite materials
High acoustic attenuation	Acoustic absorption materials
Self-sharpening property	Penetrator
High wear resistance and manufacturability	Medical devices materials

Another area of commercial interest is a highly biocompatible, non-allergic form of the glassy material that would be suitable for medical components such as prosthetic implants and surgical instruments. The unique properties of BMGs for orthopaedic applications include: (1) biocompatible; (2) excellent wear resistance; (3) high strength-to-weight ratio compared to titanium and/or stainless steel; (4) more than twice the strength compared to

titanium or stainless steel; (5) possibility of precision net-shape casting with desirable surface texture that results in significant reduction in post-processing. Some of the products taking advantage of these improvements include reconstructive devices, fractured fixations, spinal implants and instrumentation. In the near future, BMGs materials will become more and more significant for basic research and applications as the science and technology of this new field undergoes continuous developments.

### ***1.3 CRITERIA AND PROPERTIES OF THE METALLIC GLASSES***

Since the discovery of metallic glasses by Duwez and co-workers, much research effort has been devoted to the study of the thermodynamics and thermophysical properties like viscosity, relaxation, diffusion, etc. of MGs. The novel BMG-forming liquids provide large experimental temperature and time windows for measuring their physical properties, as well as for studying nucleation and growth in super-cooled liquid state and glass transition. With extensive experimental data on the formation of the BMG available, empirical rules for the achievement of large GFA were proposed [11,16]. Nevertheless, the formation mechanism of the multicomponent BMGs and the main factors that influence the GFA have not been elucidated. Over time, the discovery of new and better glass formers indicated the need for a fundamental understanding for predicting the GFA, based on thermodynamic, kinetic and structural properties of alloys.

In general, the GFA in BMGs tends to increase as more components are added to the alloy. This is the so-called “confusion principle” [28], which implies that larger number of components in an alloy system destabilize competing crystalline phases that may form during cooling. This effect frustrates the tendency of an alloy to crystallize, making the melt more stable relative to the crystalline phases. Another general guiding principle for designing

alloys that form BMGs is the choice of elements with large differences in size, which leads to a complex structure that crystallizes less easily. The addition of copper, which is much smaller in size than zirconium atom, into Zr-based alloys increases the GFA significantly. Another effective step is to seek for alloy compositions with deep eutectics, which form liquids that are stable to relatively low temperatures [11]. Inoue summarized the results of glass formation in multicomponent alloys and proposed three empirical rules [16]:

- (1) Multicomponent systems consisting of more than three elements
- (2) Significant difference in atomic sizes with the size ratios above about 12% among the main constituent elements
- (3) Negative heats of mixing among the three main constituent elements.

He claimed that the alloys satisfying the three empirical rules have special atomic configurations in the liquid state that are significantly different from those of the corresponding crystalline phases. These atomic configurations favour the glass formation in terms of thermodynamics, kinetics as well as microstructural development.

A good approximation of the microstructure of metallic glasses was given by Cohen and Turnbull (1959) [29,30] with the theory of “Free Volume - Diffusion” which considers that the molecules in a liquid act like “hard” spheres. According to this theory, the molecules move with the kinetic energy of the gas, but most of the time in a limited space because of the nearest neighbours. In some cases, the variation in density of the system can create a “hole” of sufficient size allowing a movement of a molecule thereto, thus enhancing the effect of diffusion in the liquid. As seen from the image bellow in metallic glasses there is the so-called “free volume”, i.e. that part of the site nearest the neighbourhood where the atom can be moved without changing the total energy of the system.

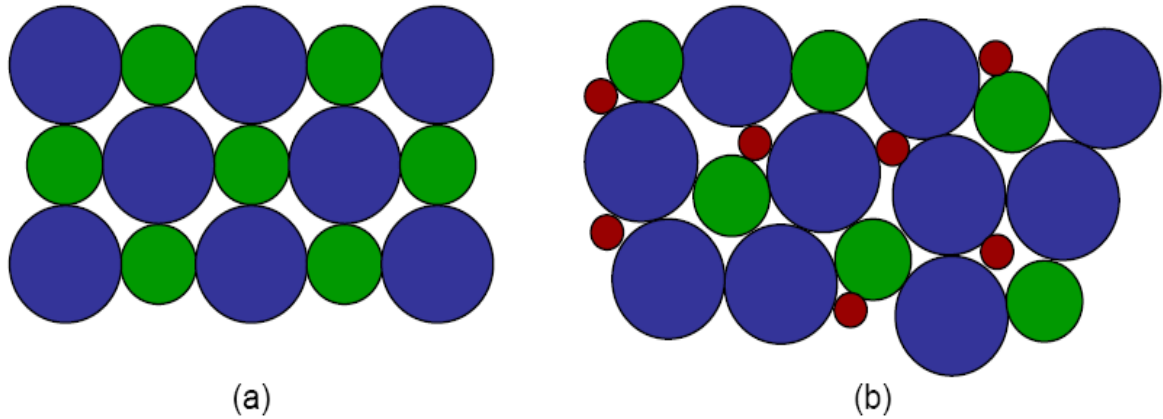


**Figure 3.** Schematic representation of atoms (represented by the green and blue circles) in (a) a crystalline structure (b) a metallic glass. (The asymmetric gaps (pointed as red circles) between the different atoms is called “free volume”)

The two basic principles of the “Free Volume” theory are:

- 1) A molecular transfer (transition) happens only if an empty space (gap) with a volume greater than a characteristic value has been created.
- 2) It is not required any energy supply for the redistribution of free volume.

The diffusion equation is:  $D = g_{CT} \exp\left(-a u^c / u_f\right)$ , where  $u_f$  is the free volume per molecule,  $u^c$  is the characteristic volume per molecule,  $a$  one adjustable parameter and  $g_{CT} = g C a(p)$ , wherein  $g$  is a geometric factor,  $a(p)$  is the diameter of the generated “gap” and  $C$  is the average kinetic energy of the gases.

From thermodynamic considerations, bulk glass formers naturally exhibit a low driving force for crystallization in the Super-cooled Liquid Region (ScLR). The low driving force results in low nucleation rates and therefore improved GFA. If a liquid is cooled below the melting point, the free energy difference between the liquid and a crystal provides a driving force for crystal nucleation, while the creation of the liquid–crystal interface creates a positive interfacial energy that disfavours nucleation. This is an energy barrier that a local composition fluctuation needs to overcome in order to form a nucleus. To enable the growth of such a nucleus, atoms within the liquid need to be rearranged. The rate of such atomic

transport is described by the atomic diffusivity,  $D$ , or viscosity,  $\eta$ . The resulting crystal nucleation rate,  $I_v$ , per unit volume is the product of a thermodynamic term, which depends on the probability of a fluctuation to overcome the nucleation barrier, and a kinetic term that depends on atomic diffusion (or viscosity) [22]:

$$I_v = \frac{A_v}{\eta(T)} \exp\left(-\frac{\Delta G^*}{k_B T}\right) \quad (1)$$

The parameter  $A_v$  is a constant on the order of  $10^{32}$  Pa·s/(m<sup>3</sup>s) and  $k_B$  is the Boltzmann constant.  $\Delta G^* = (16/3)\pi\sigma^3/(\Delta G_{l-s})^2$  is the nucleation barrier for forming a spherical nucleus,  $\sigma$  is the interfacial energy between the liquid and the nuclei and  $\Delta G_{l-s} = G_l - G_s$  is the free-energy difference between the liquid state  $G_l$  and crystalline state  $G_s$ . Generally, it has been found that high GFA is favoured by small values of  $\Delta G_{l-s}$ , which can be calculated by integrating the specific heat capacity difference  $\Delta C_p^{l-s}(T)$  according to the equation [22]

$$\Delta G_{l-s}(T) = \Delta H_f - \Delta S_f T_0 - \int_T^{T_0} \Delta C_p^{l-s}(T) dT + \int_T^{T_0} \frac{\Delta C_p^{l-s}(T)}{T} dT \quad (2)$$

where  $\Delta H_f$  and  $\Delta S_f$  are the enthalpy and entropy of fusion, respectively, at the temperature  $T_0$ , the temperature at which the crystal and the liquid are at equilibrium. A low  $\Delta G_{l-s}$  means small enthalpy of fusion  $\Delta H_f$  and large entropy of fusion  $\Delta S_f$ . The large  $\Delta S_f$  is expected to be associated with multicomponent alloys because  $\Delta S_f$  is proportional to the number of microscopic states [18]. The free energy at constant temperature also decreases in the case of low chemical potential caused by the low enthalpy and high value of  $T_{rg}$  as well as the large liquid/solid interfacial energy [18]. Therefore, the increase in the number of alloy components leads to the increase in  $\Delta S_f$  and causes the increase in the degree of dense random packing in the liquid state. This is favourable for the decrease in  $\Delta H_f$  and the

solid/liquid interfacial energy. The concept is consistent with the “confusion principle” [28] and Inoue’s first empirical rule [16].

The multicomponent alloys with excellent GFA have low melting temperature as has been shown in Table 2. In view of this, high GFA alloys can be found among alloy compositions with deep eutectics, which form liquids that are stable to relatively low temperatures. Therefore,  $T_{rg} = T_g / T_m$  is a key parameter for glass formation, and the homogeneous nucleation rate in the undercooled melt is a strong function of the parameter [9]. Searching through binary phase diagrams, one finds that the best candidates for good glass formers are systems like Pd–Si, Pd–P, Ni–Nb, Cu–Zr and Zr–Be, which all exhibit deep eutectics. In the ternary Zr–Ti–Cu, one can find the composition at the deeper eutectic that has better GFA [31]. The situation is further improved by taking quaternary alloys of Cu–Ti–Ni–Zr [11,32]. Apart  $T_{rg}$ , another extensively used parameter for GFA is the difference between the onset temperature of the first crystallization peak ( $T_x$ ) and the glass transition temperature, i.e.  $\Delta T_x = T_x - T_g$ . However, the comparison of GFA based on  $T_{rg}$  and  $\Delta T_x$  shows significant discrepancies in some alloy systems. A refined parameter taking  $T_x$ ,  $T_g$  and  $T_l$  into account was therefore proposed by Lu and Liu [33]. They found that the parameter  $\gamma = T_x / (T_g + T_l)$  gave better reference for judging the GFA among metallic glasses.

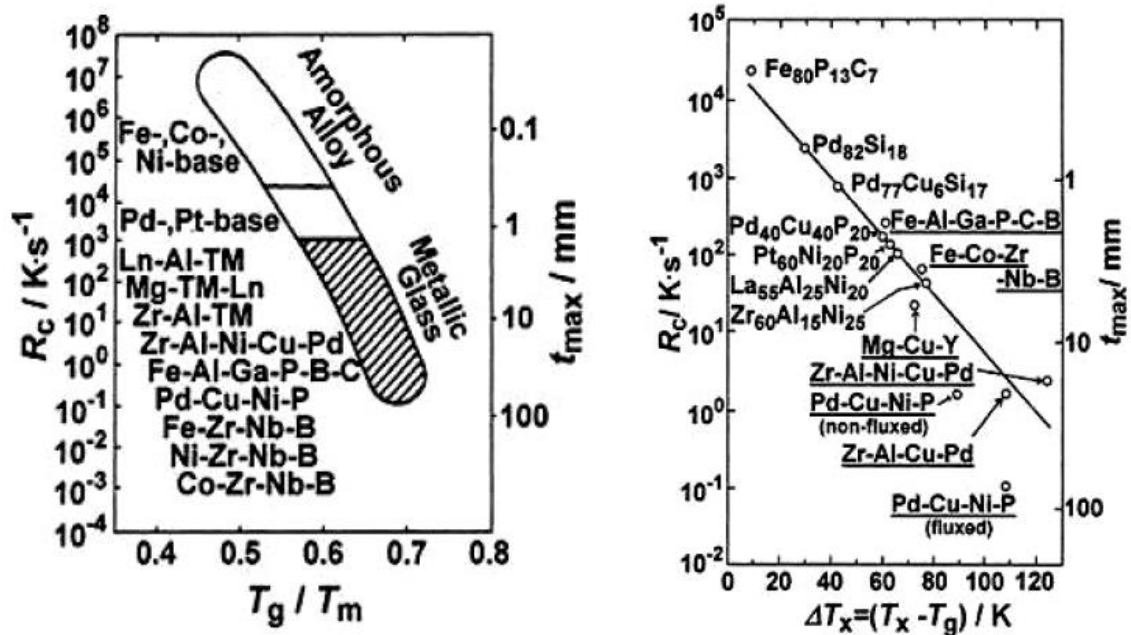


Figure 4. The critical cooling rate ( $R_c$ ) and the thickness ( $t_{max}$ ) of various MGs as a function of (a)  $T_g$  (left graph), (b)  $\Delta T_x$  (right graph). [18]

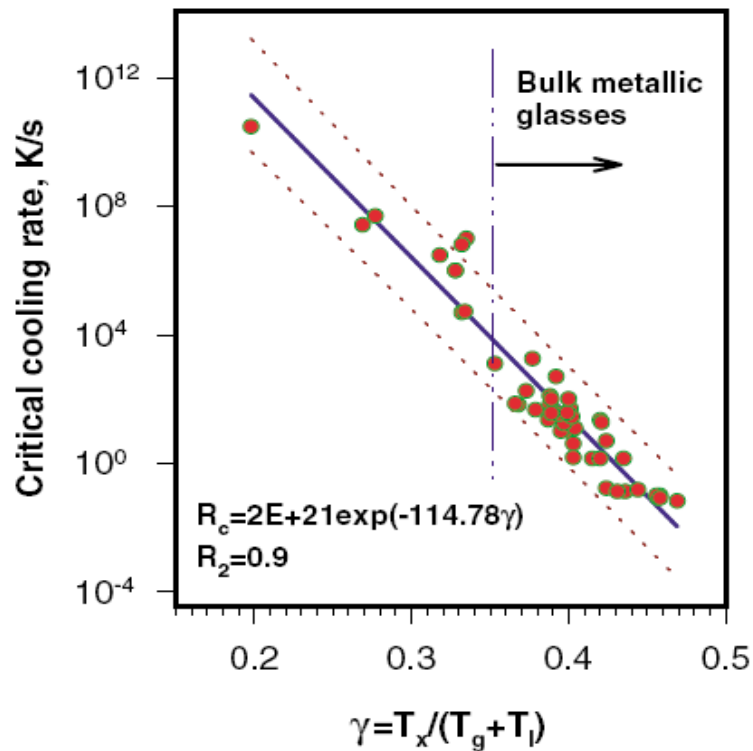


Figure 5. The critical cooling rate ( $R_c$ ) as a function of  $\gamma$ .  
Z. P. Lu and C.T. Liu Phys. Rev. Lett. 91, 11 2003

Glass transition from liquid to glassy state cannot be described as a thermodynamic phase transition, despite the deviation from linearity in the specific heat observed at the glass transition temperature. To better characterize the GFA of BMG systems, one needs to study the crystallization kinetics in these alloys. From the perspective of kinetics, parameters like viscosity have a significant influence on the GFA of an alloy system. A variety of techniques have been applied to measure viscosity from the equilibrium liquid down to the deeply undercooled liquid near  $T_g$  [34-36]. Since the undercooled liquid alloys are relatively stable with respect to crystallization on laboratory time scales, viscosity can be measured in bulk glass-forming systems in much wider temperature and time scales than before.

Viscosity and diffusivity are often related by the Stokes–Einstein relation  $D = k_b T / (3\pi\eta(T)l)$ , where  $l$  is the average atomic diameter. Viscosity of liquids is commonly described by a modified Vogel–Fulcher–Tamman (VFT) relation [37],

$$\eta(T) = \eta_0 \exp\left(\frac{D^* T_0}{T - T_0}\right) \quad (3)$$

where  $D^*$  is the fragility parameter ( $1 \leq D^* \leq 100$ ),  $T_0$  is the VFT temperature, and  $\eta_0$  is a constant inversely proportional to the molar volume of the liquid. Physically,  $T_0$  is the temperature where the barrier with respect to flow becomes infinite. The change of viscosity of a liquid as a function of undercooling can be used to characterize and classify the different liquids [37], because it reflects the change of the atomic mobility during super-cooling and in addition, the fragility describes the degree with which the viscosity of a super-cooled liquid deviates from an Arrhenius behaviour. Fig. 6 compares the viscosities of some typical BMGs with a selection of typical non-metallic liquids [38].  $\text{SiO}_2$  is the strongest glass former with the fragility  $D^*$  of about 100. It exhibits a very small VFT temperature and a very high melt viscosity. At the opposite, *O*-terphenyl is the typical fragile glass with a fragility of 5

[39] and low melt viscosity. It shows a more abrupt change in the kinetics close to the glass transition. The available viscosity data of BMG forming liquids show that they behave closer to strong glasses than fragile glasses and have fragility approximately equal to 20. The melt viscosity of BMGs is in the order of 2–5 Pa·s and is about three orders of magnitude more viscous than pure metals, which usually have viscosities of the order of  $10^{-3}$  Pa·s [11].

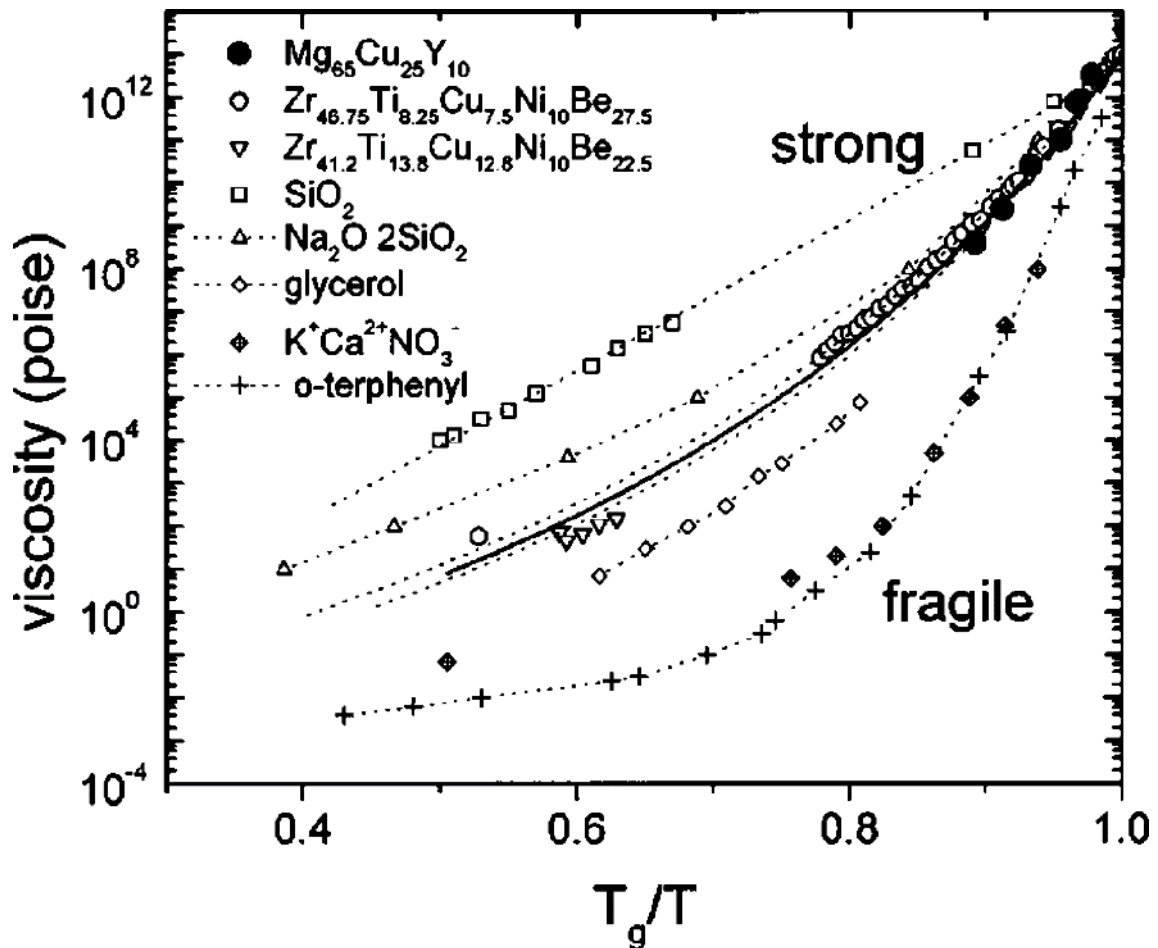


**Figure 6.** Comparison of viscosity of various glass-forming liquids. The plot shows that a BMG forming liquid can be classified into strong liquid [38].

The relaxation behaviour of the BMG forming liquids studied by neutron scattering is also similar to the nature of strong liquids [40,41]. The strong liquid behaviour implies high viscosity and sluggish kinetics in the super-cooled liquid state. This significantly prevents the formation of stable nuclei in the melt. The growth of the thermodynamically favoured

phases is inhibited by the poor mobility of the constituents. The nucleation and growth of the crystalline phase in the super-cooled liquid state is very difficult and thus it leads to large GFA and high thermal stability of the super-cooled liquid state. The conventional metallic glasses have nucleation kinetics in the undercooled region such that the onset time for crystallization is in the regime of  $10^{-4}$  to  $10^{-3}$  s. For BMG forming systems, the time scale can be of the order from 100 to 1000 s.

Nevertheless, the stabilization factors of atomic structures, a priori, originate from the electronic structure of a metallic glass. Heading in this direction, Nagel and Tauc treated metallic glasses as a nearly free electron metal and they used the influence of the conduction electrons on the structure factors in order to understand the stability of a metallic glass against crystallization [42]. They proposed that a metallic glass is stabilized when the Fermi surface and the diffused pseudo-Brillouin zone boundary of the glassy phase coincide, i.e. the Fermi level ( $E_F$ ) is located at a minimum in the density-of-state curve. In such a case, the basic characteristic wave numbers, the diameter of the Fermi sphere and the first peak of the static structure factor, are equal,  $2k_f = k_p$ . As a sequence, they argued that the effect of alloying would cause the rigid shift of  $2k_f$  with respect to  $k_p$ . As  $2k_f$  moves away from  $k_p$ , the system would become less stable against crystallization and thereby will have a lower  $T_g$  [43,44]. The criterion implies that the pseudogap in the density-of-states curve is a necessary condition. Under this situation, the falling of the Fermi level on the declining slope of the pseudogap naturally contributes to lowering of the total kinetic energy of electrons thereby reducing the system's energy.

Haeussler et al. [45] deduced from measured ultraviolet photoelectron spectra the presence of a structure-induced density-of-states pseudogap in the vapour-deposited amorphous Cu–Sn and Au–Sn thin films. This is also the basic feature of most of the noble metal-simple polyvalent metal alloys, and the glass-forming composition with the

concentration of conduction electrons ( $e/a$ , electron concentration per atom) of 1.8 is proposed as the “ideal amorphous state” [46]. For the electronically simple metallic glasses,  $2k_f$  is well defined. Mizutani [47] constructed a two-dimensional map in terms of  $2k_f/k_p$  and the size ratio of the two different elements,  $r/R$ , and they summarized that glass formation, as obtained by liquid quenching, occurs at an extended  $2k_f/k_p$  span between 0.8 and 1.2 when  $r/R$  is in the range 0.5–0.8.

However, for alloys containing transition metals (*TMs*), the total density-of-states deviates significantly from the near-free-electron parabola due to the existence of the  $d$ -states in their valence bands and the rather small effect induced by structure would be masked if the Fermi level falls in the  $d$ -band. Experimentally, pseudogaps were not observed in the Cu–Zr [47] and Pd–Si [48] metallic glasses, and not even in the Cu-containing Hume-Rothery-type Au–Cu–Mg metallic glasses [49]. In the following figures we can see the variation of the logarithm of the cooling rate ( $\log(R_c)$ ) versus the ratio  $e/a$ , the  $T_{rg}$  and the change in entropy for various metallic glasses.

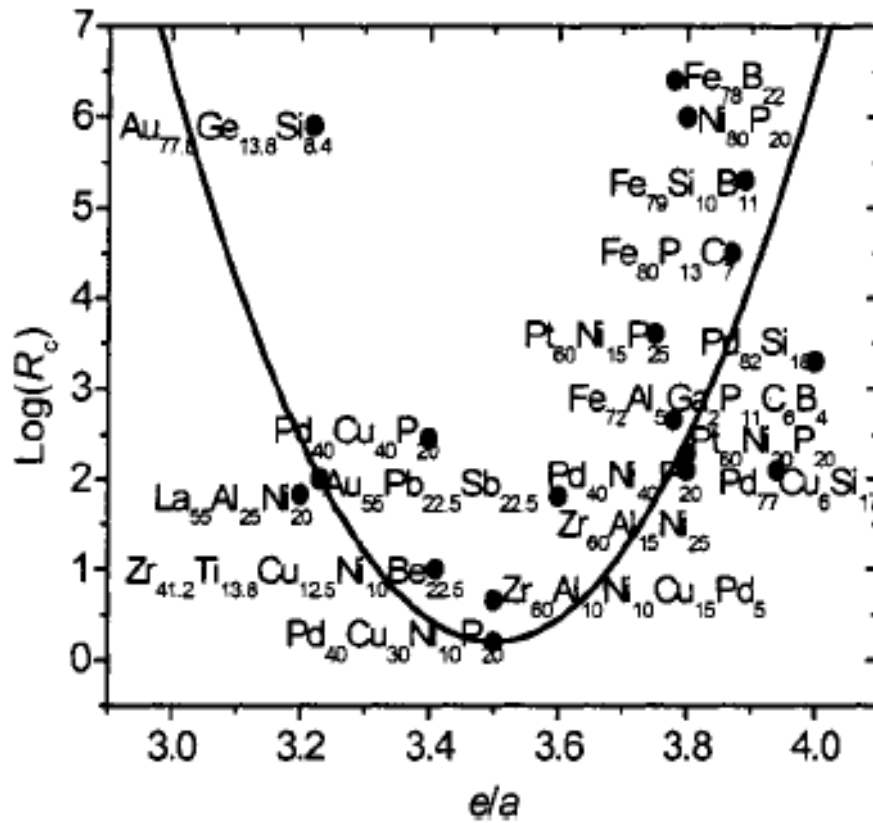


Figure 7a. Logarithm of the cooling rate as a function of the ratio  $e/a$   
*Q. Jiang, B. Q. Chi, J. C. Li vol. 82, 18A.P.L.*

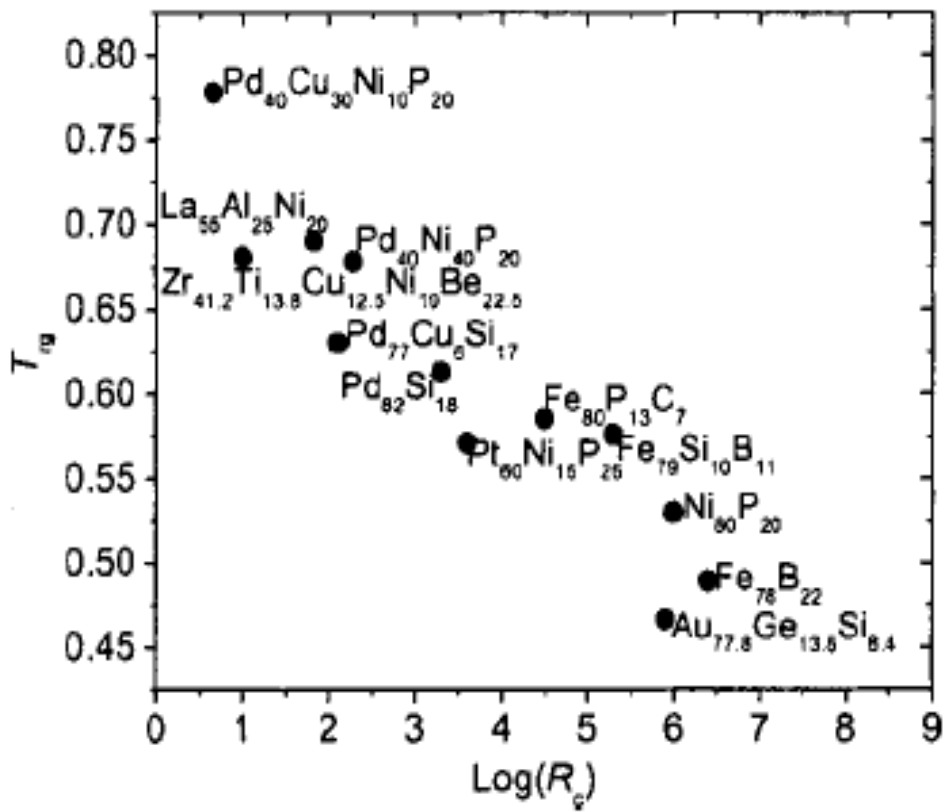


Figure 7b.  $T_g$  temperature versus the cooling rate.  
*Q. Jiang, B. Q. Chi, J. C. Li vol. 82, 18 A.P.L.*

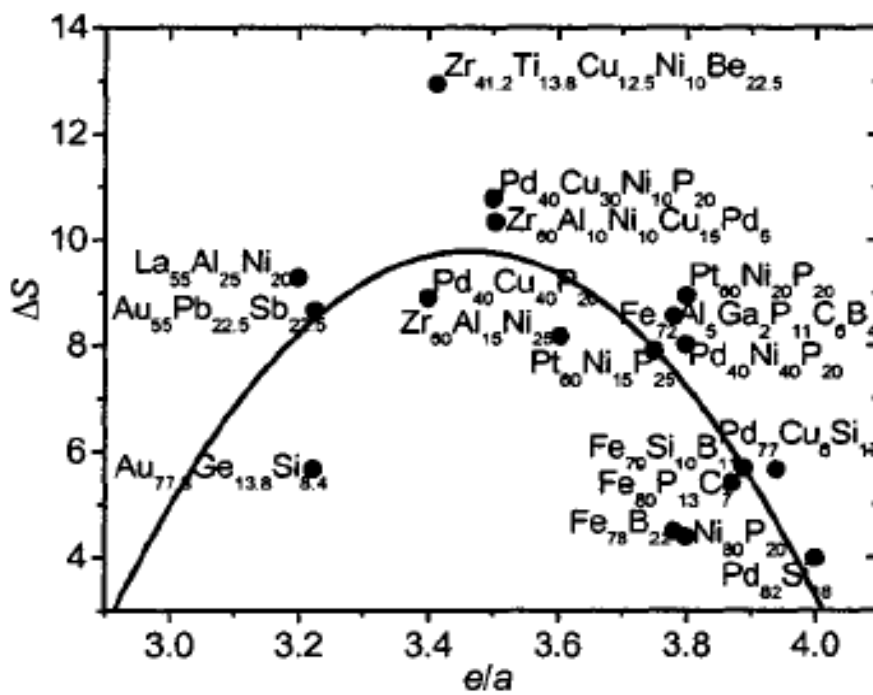
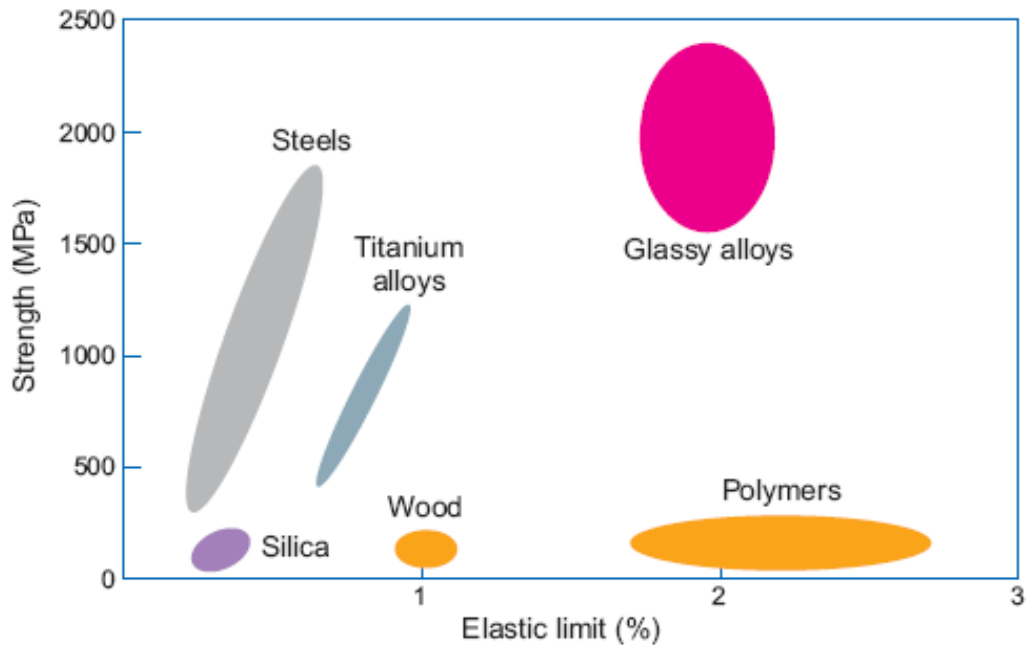


Figure 7c. Entropy change as a function of the ratio  $e/a$ .  
*Q. Jiang, B. Q. Chi, J. C. Li vol. 82, 18 A.P.L.*

#### 1.4 CHARACTERISTICS OF THE METALLIC GLASSES

The superior mechanical properties of bulk metallic glasses are the most promising for applications. Due to the absence of dislocation plastic deformation is not easy and thus metallic glasses are high-strength materials. Fig. 8 shows the relationship between the elastic limit and the strength for BMGs and other materials, while Fig. 9 summarizes the relationship between Young's modulus ( $E$ ) and tensile fracture strength ( $\sigma_{t,f}$ ) or Vickers hardness ( $H_v$ ) for typical BMGs [50,51]. It can be seen that the tensile fracture strength and  $H_v$  of BMGs have a roughly linear relationship with  $E$ . Similar trend is also evident in ordinary crystalline alloys shown in the figure, but the slopes of the linear region for the BMGs are much steeper than that of the crystalline alloys, indicating larger elastic limits of



**Figure 8.** Tensile strength of various materials versus their elastic limit.

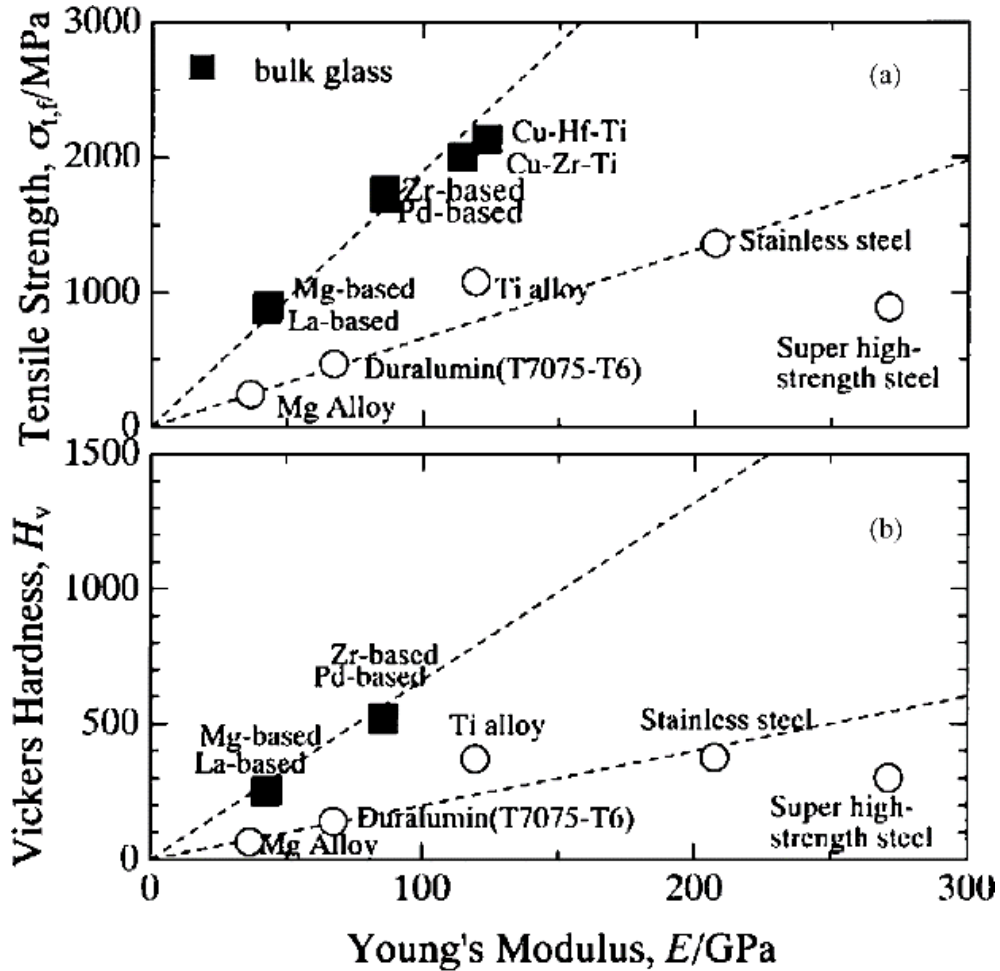


**Figure 9.** The relations between mechanical properties of typical BMGs: (a) tensile fracture strength ( $\sigma_{t,f}$ ) with Young's modulus ( $E$ ); (b) Vickers hardness ( $H_v$ ) with Young's modulus ( $E$ ). [51]

the BMGs compared with those of the crystalline alloys [52,53]. The much better linearity of the lines for BMGs is attributed to the formation of an ideally homogenized solid solution over the whole composition range which is one of the typical features of glassy alloys.

It can be summarized that BMGs have much higher tensile strengths and much lower Young's moduli. The difference in these values between the BMG and crystalline alloys is as large as 60%. The significant difference in the mechanical properties is thought to be a reflection of the difference in the deformation and fracture mechanisms between BMGs and crystalline alloys. Plastic deformation in metallic glasses is generally associated with inhomogeneous flow in highly localized shear bands. Under high strain rate conditions, local melting occurs during unstable fracture [54]. Even under slower loading rates, a veined

fracture surface indicates a decrease in the glass viscosity. Due to the highly localized nature of flow and the lack of microstructural features in the metallic glass to divert the flow, shear band formation typically leads to catastrophic failure.

In addition to the high static mechanical strength, the Zr-based BMGs exhibit high Charpy impact fracture energies ranging from 110 to 140 kJ/m<sup>2</sup> and high fracture toughness limit [55]. The fatigue limit is nearly the same as those of the crystalline alloys. Considering that the tensile fracture strength of the BMG is about double that of the crystalline alloys, the fatigue endurance stress level is also much higher for the BMGs. It is also found that the difference in BMG and crystalline structure does not have a dominant role in the propagation velocity of fatigue cracks, though the deformation and fracture behaviour under a uniaxial applied load is clearly different from those for crystalline alloys [55]. Imposing mechanical deformation in the metallic glasses results in the formation of narrow regions where the plastic flow is detected without affecting the rest of the material. These areas are called shear transformation zones and it is believed that under strong mechanical deformation these zones are joined together to form the so-called shear bands, which are located throughout the plastic deformation leaving the other materials intact. In Fig. 10 is given an experimental confirmation of the presence of deformation zones and their role in the catastrophic collapse of a metallic glass.

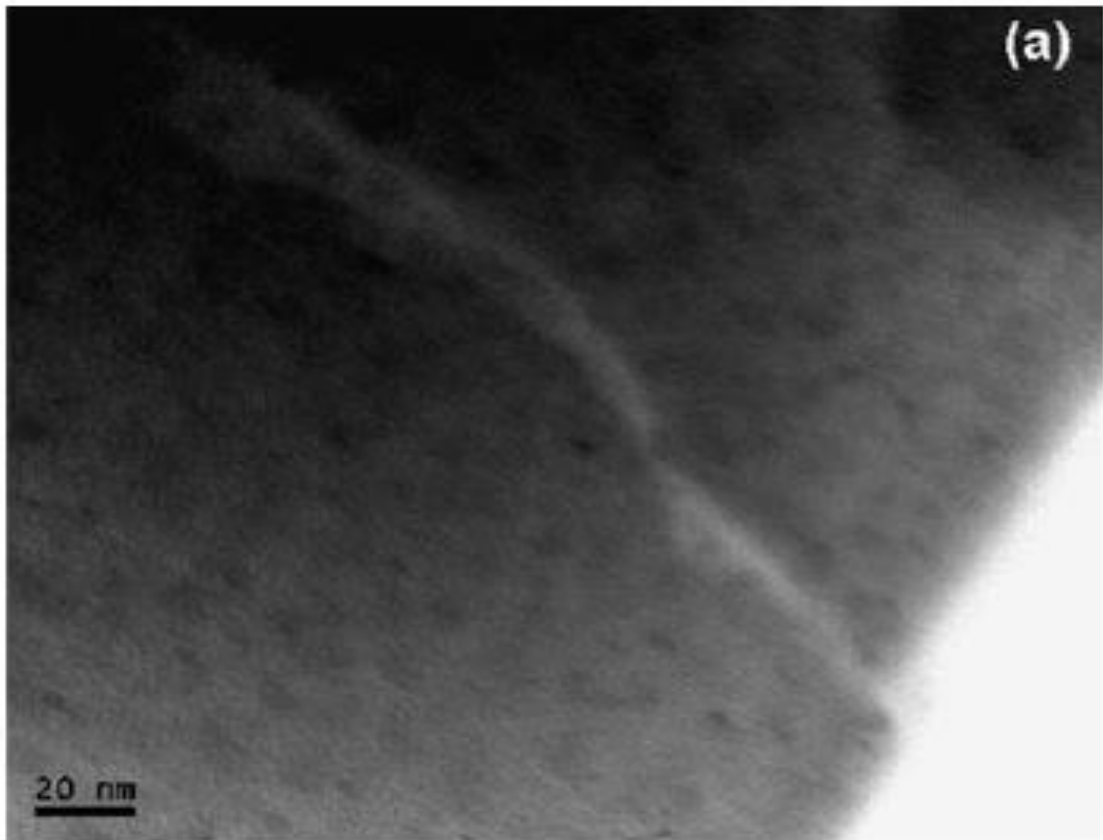


**Figure 10.** TEM image showing the formation of a deformation zone  
*K. Hajlaoui et al. Scripta Materialia 54 (2006) 1829-1834*

The acoustic features of BMGs are measured and compared with those of other glasses. Table 4 lists the acoustic data, Debye temperature and elastic constants for typical BMGs and oxide glasses. In table 4,  $\sigma$  characterizes the relative value of the compressive and shear deformation of a solid [56]. The values of  $\sigma$  for various BMGs ranges from 0.3 to 0.4, which are close to that of crystalline metals [57], e.g. 0.37 for copper and 0.33 for Monel, which is a crystalline copper alloy. On the other hand, conventional metallic glasses have higher value of  $\sigma$  ( $\approx 0.40$ ) [58], while typical oxide glasses have  $\sigma$  ranges from 0.15 to 0.25 (see Table 4). The oxide glasses are brittle, since atoms or molecules can hardly rearrange themselves to shear strains without a drastic disturbance in bonding configurations. In contrast, the metallic glasses with higher values of  $\sigma$  have larger plastic deformation indicating the ease

of atomic rearrangement in the materials. The comparison indicates that  $\sigma$  bears certain relationship with the atomic configuration in these amorphous materials. The GFA also has relation with the value of  $\sigma$  of a glass-forming system. The conventional metallic glasses have poor GFA (the critical cooling rate,  $R_c$ , for the glass formation, which represents the GFA of an alloy, is from  $10^4$  to  $10^7$  K/s). The GFA of the BMGs ( $R_c$  ranges from 1 to 100 K/s; for vit1,  $R_c$  is even lower than 1 K/s [11]) is much better than that of the conventional metallic glasses and approaches that of oxide glasses whose  $R_c$  is less than 1 K/s. A smaller  $\sigma$  may result in high GFA in a glass-forming system.

**Table 4** - [22]

The thermal parameters in relation to their thermal stabilities and GFAs.

Sample	$\rho$ (g/cm <sup>3</sup> )	$v_l$ (km/s)	$v_s$ (km/s)	$E$ (GPa)	$G$ (GPa)	$K$ (GPa)	$\sigma$	$\theta_D$ (K)	$v_l/v_s$	$K/G$
Zr <sub>41</sub> Ti <sub>14</sub> Cu <sub>12.5</sub> Ni <sub>10</sub> Be <sub>22.5</sub>	6.125	5.174	2.472	101.0	37.4	114.1	0.350	327	2.09	3.06
Zr <sub>46.75</sub> Ti <sub>8.25</sub> Cu <sub>7.5</sub> Ni <sub>10</sub> Be <sub>27.5</sub>	6.014	5.182	2.487	100.5	37.2	111.9	0.350	327	2.08	3.01
Zr <sub>45.4</sub> Ti <sub>9.6</sub> Cu <sub>10.15</sub> Ni <sub>8.6</sub> Be <sub>26.25</sub>	6.048	5.171	2.485	100.9	37.3	111.9	0.350	327	2.08	3.00
Zr <sub>48</sub> Nb <sub>8</sub> Cu <sub>12</sub> Fe <sub>8</sub> Be <sub>24</sub>	6.436	4.994	2.338	95.7	35.2	113.6	0.359	306	2.13	3.22
(Zr <sub>0.59</sub> Ti <sub>0.06</sub> Cu <sub>0.22</sub> Ni <sub>0.13</sub> ) <sub>85.7</sub> Al <sub>14.3</sub>	6.608	4.890	2.269	92.7	34.0	112.6	0.363	291	2.15	3.31
Cu <sub>60</sub> Zr <sub>20</sub> Hf <sub>10</sub> Ti <sub>10</sub>	8.315	4.620	2.108	101.1	36.9	128.2	0.368	282	2.02	3.47
Pr <sub>60</sub> Cu <sub>20</sub> Ni <sub>10</sub> Al <sub>10</sub>	6.900	3.030	1.406	37.2	13.6	45.2	0.363	160	2.16	3.31
Pd <sub>39</sub> Ni <sub>10</sub> Cu <sub>30</sub> P <sub>21</sub>	9.152	4.740	1.960	98.2	35.1	159.1	0.400	280	2.42	4.52
Float glass	2.518	5.850	3.470	74.5	30.3	45.7	0.230	320	1.69	1.50
Ti-glass	2.196	5.745	3.615	67.3	28.7	34.2	0.170	330	1.59	1.20
Window glass	2.421	5.593	3.385	67.2	27.7	38.7	0.211	–	1.65	1.40
Water-white glass	2.479	5.836	3.423	71.9	29.1	45.7	0.238	–	1.70	1.57
Fused quartz	2.201	5.960	3.750	72.7	31.0	36.9	0.170	496	1.59	1.16
Microcrystal glass	2.556	6.490	3.666	87.0	34.4	61.9	0.266	–	1.77	1.80
Borosilicate glass	2.320	5.640	3.280	61.9	24.9	40.5	0.240	–	1.72	1.60
Carbon glass	1.560	3.880	2.407	21.4	9.01	11.4	0.187	338	1.61	1.26

The nature of the chemical bonds in a solid determines the microstructure of the solid, thus the difference in microstructure will influence the mechanical properties of a solid and then result in the variation of the acoustic parameters. Compared with oxide glasses, BMGs have large values of elastic constants  $E$ ,  $K$ ,  $G$  and  $K/G$ .  $K/G$  are between 1.16 and 1.8 for the covalent bond oxide glasses and 3.0 and 4.5 for various BMGs which is similar to metals, such as Cu and steel ( $K/G$  is about 2.5) [58] and is markedly different from those of oxide glasses. The relatively larger values of  $G$  and  $E$  for the BMG compared to oxide glasses means that the bond length and bond angle of the structure in the BMGs cannot be changed

easily.

Table 5 exhibits the acoustic and elastic parameter changes after crystallization in vit1. The changes are not simply attributed to the small density difference between the amorphous and crystalline states; instead, it is mainly related to the unique microstructural characteristics of the metallic glassy state. The softening may have close link with the excellent glass-forming ability of the glass-forming system [59].

**Table 5** - [22]

Comparison of the properties of metallic glasses state ( $Y_a$ ) and fine-grained crystallized state ( $Y_c$ ) of  $Zr_{41}Ti_{14}Cu_{12.5}Ni_{10}Be_{22.5}$  alloy.

Alloy	$\rho$ (g/cm <sup>3</sup> )	$v_l$ (km/s)	$v_s$ (km/s)	$K$ (GPa)	$G$ (GPa)	$\theta_D(T)$ (K)
Glassy state	6.125	5.174	2.472	114.1	37.41	326.8
Crystallized state	6.192	5.446	2.807	118.6	48.80	370.9
$(Y_c - Y_a)/Y_a$ (%)	1.1	5.2	13.5	3.9	30.3	13.4

The different responses to pressure of silicate and metallic glasses are due to completely different structural characteristic of BMGs (random close packing (RCP) atomic configuration) and oxide glasses (continuous-random networks (CRN)). Oxide glass is a covalent-bonded glass with a significant spread in Si–O–Si bond angles. Under high pressure, the change of the bond angles between atoms in oxide glass leads to negative pressure-dependent velocities. For BMGs with RCP structure, however, the nature of metallic bond is retained in the BMGs, although atomic long-range order is lacking. In the transition process from the glass to crystalline state, there is no significant change of the nearest-neighbour atoms and the distance between atoms. However, the small change of the volume can sensitively induce changes in the electron configuration, atomic interaction force and the relative flow between atoms. So BMGs have a large shear modulus change upon crystallization.

The above results therefore imply that the short-range order structure of the BMG has close correlation with the atomic configurations in their metallic components. Since those

metallic components are of cubic close-packed structures, it is very likely that the similar atomic close-packed configurations dominate the short-range structure of the BMGs. These highly packed structures have also been confirmed by density measurements. The relative density change of the BMGs between amorphous and fully crystallized states is less than 1.0% [60].

The conventional metallic glasses with poor GFA have their corresponding crystalline compounds similar to the amorphous alloys in their local structures and compositions [61]. For these alloys, the cooling rates are the most important factor to inhibit the nucleation and growth of the competing crystalline phases. For the BMG formers, however, the critical cooling rates are much lower, and their local microstructural characteristics therefore become a decisive factor for their glass-forming abilities. The fivefold symmetry at their short range order, presented in the form of icosahedral (ICO) clusters, in the amorphous state would provide an additional barrier for nucleation of the crystalline phases. From kinetics point of view, the crystallization of BMG requires a substantial redistribution of the constituent elements across the icosahedral liquid. The highly dense, randomly packed structure of the BMG in its ScLR results in extremely slow atomic mobility [62], thus making the redistribution of atoms on a large scale very difficult. This fundamental structural discontinuity between the crystalline and the amorphous state suppresses the nucleation and growth of the crystalline phase from the ScLR and results in an excellent GFA.

In order to understand the origin of the high thermal stability and excellent glass forming ability, it is very important to clarify the crystallization behaviours at the ScLR. BMGs with very stable super-cooled liquid state and high thermal stability against crystallization offer a large experimentally accessible time and temperature window to investigate the nucleation and growth of crystals under various conditions in the ScLR. Extensive investigations of the crystallization process in BMG were carried out and a lot of interesting features were

reported. The results are important for a number of aspects, namely, the understanding of the nucleation and growth in the metallic super-cooled liquid, the evaluation of the glass-forming ability of the melts and the thermal stability of metallic glasses, as well as the production of bulk nanocrystalline and composites from controlled crystallization [63–76].

### ***1.5 STUDY OF THE Cu-Zr SYSTEM***

Summarizing, to fully investigate the vitrification procedure and to better characterize the GFA of BMG systems, one needs to understand the origin of their high thermal stability and it is very important to clarify the crystallization behaviour in the ScLR. The nucleation and growth of several nanostructures, i.e. clusters, in the metallic super-cooled liquid play an important role to the GFA of these alloys. The ability to form a glass by cooling from the equilibrium liquid is equivalent to suppressing crystallization within the ScLR. Even the mechanical properties during deformation of BMGs are generally associated with inhomogeneous flow in highly localized shear bands due to the lack of microstructural features, i.e. the nanostructures composing the BMGs lead to highly localized nature of flow. The above results therefore imply that the short-range order structure of the BMG has close correlation with the atomic configurations in their metallic components.

Cu-Zr MGs respond to all these structural characteristics and moreover, compared with other binary alloys, they are attracting attention because of their simplicity and despite the relatively weak interaction between the components [77], they exhibit a tendency to pass in vitreous state in a wide compositional range.. As a consequence they have being used as the basis for a large number of amorphous materials such as Cu-Zr-Al, Cu-Zr-Ni, Cu-Zr-B, Cu-Zr-Ga, Cu-Zr-Al-Ni, Cu-Zr-Al-Co-Ni, Cu-Zr-Al-Ni-Pd, Cu-Zr-Ti-Ni-Be [78,79] etc. Furthermore, the Cu-Zr phase diagram is known (Fig. 11) making it more accessible for

study.

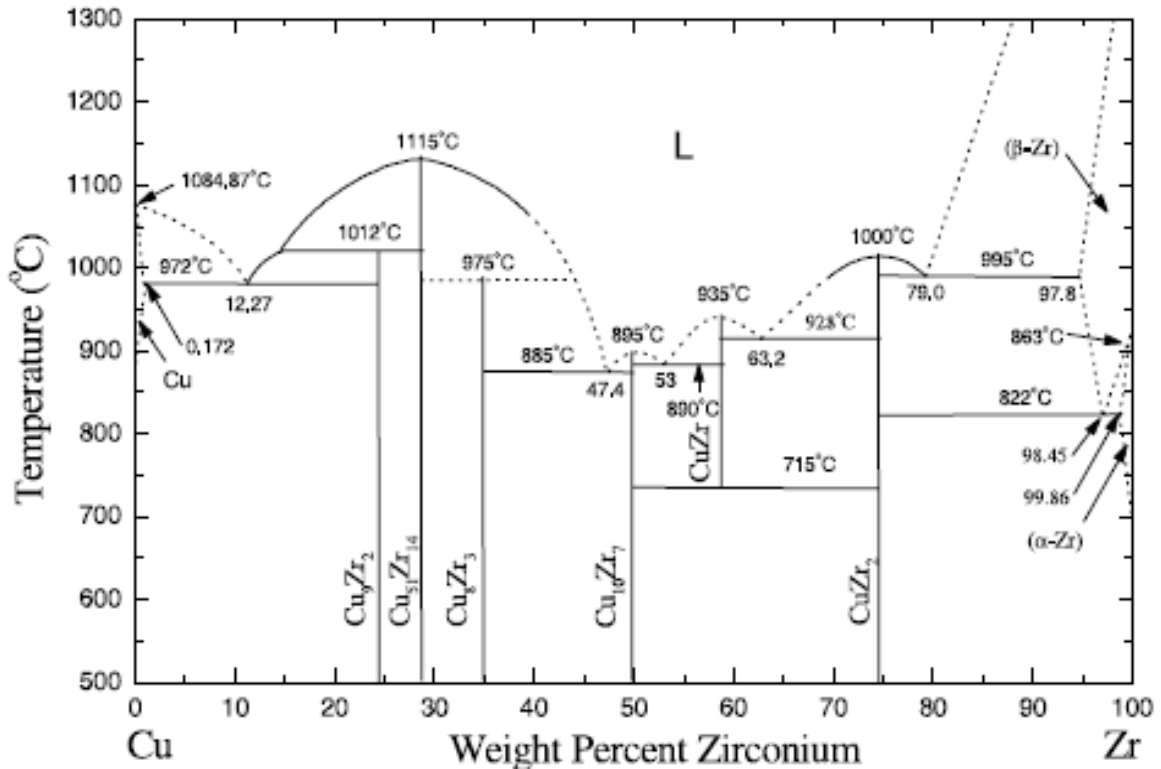


**Figure 11.** Phase diagram of Cu-Zr  
*H.R. Wang et al. Journal of Non-Crystalline Solids 311 (2002) 36-41*

Cu and Zr satisfy the second and third rule of GFA after the ratio of their sizes is 1.28, i.e. 12.8%, and the enthalpy of mixing is negative and equal to -23 kJ / mol. Furthermore, the produced Cu-Zr alloys exhibit large GFA; the  $T_{rg}$  ratio is about 0.583, very close to the desired 0.6-0.7 that favours the GFA. Another important feature is their capability to be prepared in the form of fully amorphous strips with a bronze casting process matrix [80].

Here we study in details the behaviour of the microstructure of Cu-Zr MGs during solidification and we clarify the way that the formation of nanostructures, i.e. clusters, affect the GFA of these materials. We answer also another important issue concerning the

interaction between these clusters and we found the driving force that leads them to combine into larger structures, i.e. SuperClusters. We are going to show how the vitrification of the microstructure occurs at the ScLR, as well as the role of these nanostructures in absorbing an external deformation. The research that includes all these findings was mainly performed by molecular dynamic simulations allowing us to reveal all the information hidden in the details of the atomistic configurations.

## 2 SIMULATION TECHNIQUES

For many years materials science research attends in establishing accurate correlations between the properties and the microstructure of materials. Due to the complexity of the interactions among the ingredients, theoretical investigations are basically restricted to some simple models, which could only provide some approximate descriptions of the real materials [81]. In recent decades, the significant increase in computational resources provided the capability for more detailed studies, i.e. from macroscopic to atomic and even down to electronic scales, a new and exciting interdisciplinary scientific field has been rapidly developed, i.e. the Computational Materials Science. The computational materials science has been playing an important role in promoting the development of materials science, since it bridges the theory with the real experiment. As the computation deals with the detailed mechanism down to atomic scale or even to a depth of the electronic structures of solids, significant progress has been achieved and therefore made it possible to approach a quantitative understanding of the correlation between the micro-structure and property of metals and alloys [82]. The final goal of computational materials science is to help the researchers to acquire the knowledge and design materials with desired microstructure and properties.

The correlation between the microstructure and the properties of a material is generally studied at four different scales: the electronic, atomic, mesoscopic and macroscopic scale [82,83]. For instance, the electronic and magnetic properties of matter should be investigated by *ab initio* calculations, while the atomic scale simulations, i.e. molecular dynamics simulation or Monte Carlo methods, concentrate on the microstructure and dynamical properties. Comparatively, simulations in mechanical engineering focus on large-scale construction problem at macroscopic scale, e.g. using finite elements methods [83].

## ***2.1 AB INITIO***

An accurate prediction of the correlation between the microstructure and the properties of a material requires the solution of the Schrodinger equation for about 1000 nuclei and the electrons of each one of these. Moreover, the Hamiltonian describing all these particle interactions involved in the problem must be known. Such a calculation requires a huge computational effort and it is hardly possible to directly solve the Schrodinger equation for real materials. However, the ab initio calculations have incorporated some reasonable assumptions and approximations. For example, almost all ab initio calculations based on the density functional theory use the adiabatic Born–Oppenheimer approximation. The ab-initio calculations can generally classified into three major groups [84]:

- (1) The first group consists of approaches starting from the Hartree–Fock approximation, which offers a rigorous one-electron approximation.
- (2) The second group consists of approaches based on the density functional theory, which offers an exact background for a many-body problem, yet can only be solved approximately. The resulting equation is again one-electron-like.
- (3) The third group consists of the quantum Monte Carlo method.

However, due to the high computational cost, ab initio calculations are still limited to the study of static properties of systems involving only a few tens of atoms. Other methods, such as the Monte Carlo or molecular dynamics simulations are very powerful and are therefore are extensively used in the rapidly growing field of computational materials science [83,85].

## ***2.2 MONTE CARLO***

The Monte Carlo (MC) method represents a variety of stochastic techniques which are based on the use of probability statistics to investigate the issues in many fields such as economics, nuclear physics and flow of traffic. Concerning materials science, the physical and chemical properties of a system can be obtained as statistical averages over stochastically generated conformations of particles [83,84]. The MC is therefore a stochastic method, assuming some idealized or simplified atomic interactions and thus, it is able to deal with large number of atoms. In practice, the MC method is often used to determine equilibrium states for known distribution functions or to directly solve the integral formulation of the equation of motion [86].

A well-known MC method for structural analysis based on experimental data is the Reverse Monte Carlo (RMC) modelling. RMC modelling can be applied to many different sorts of data, simultaneously if required. Powder and single-crystal neutron diffraction (including isotopic substitution), x-ray diffraction (including anomalous scattering) and electron diffraction, extended x-ray absorption fine structure and nuclear magnetic resonance (magic angle spinning and second moment) have already been used to provide data [87].

## ***2.3 MOLECULAR DYNAMICS***

In addition to the MC methods, the molecular dynamics (MD) simulation represents another major simulation scheme for accessing the microstructure at atomic scale [83,88]. The MC methods is a statistical and probabilistic approach that explores the phase space in a stochastic manner, while the MD simulation is a deterministic scheme, which is capable of tracking the motion of each individual particle. In fact, the MD simulation mimics the elementary atomistic path-dependent process by solving the motion equations of all involved

particles. It can be shown that a quasi-classical treatment of the atomic interactions and the resulting dynamics in terms of the potentials and classical equation of motion is consistent with the solution of the time-dependent Schrodinger equation for all atoms within some limitations. The analogy can essentially be derived by separating the time-dependent part from the time-independent part of the Schrodinger equation, using the adiabatic Born–Oppenheimer approximation for splitting the wave function into one part to describe the dynamics of the light electrons and another part to describe the dynamics of the heavy nuclei, respectively, and by replacing the quantum-mechanical expression for the kinetic energy by the classical momentum term. Under such treatment, simulation of the atomic configurations with instantaneously equilibrated electrons in their ground state merely requires an adequate incorporation of the forces among the atoms. The time evolution of the ensemble is then computed by integrating the equations of motion in a discrete fashion using the time steps of  $10^{-14}$  to  $10^{-15}$  s [83]. The position and velocity of each individual atom, as well as the physical properties of the system, can then be retrieved from the calculation results. The first MD simulation was reported by Alder and Wainwright in 1957 [89]. With outstanding contributions from such as Rahman [90], Verlet [91,92], Andersen [93], Hoover [88,94–96], Nose [97], and Parrinello [10,98,99], among others, the MD simulation has become a powerful method for detailed microscopic modelling at atomic scale and has been applied to many basic issues in the fields of materials science and condensed matter physics.

The forces exerted on each atom of a system can be calculated from the interactions between atoms. In classical and semi-classical simulations, these interactions are expressed in terms of potential functions that describe how the potential energy of a system depends on the coordinates of the atoms. It is well-known that in MD simulation, the interatomic potential plays a fundamental role, as the accuracy of the simulation in reproducing the

experimental observations depends mainly on the accuracy of the potential model used. Consequently, a great effort has been made in developing reliable interatomic potentials and several models have been proposed [11,100–103].

The simplest one is the Lennard-Jones potential, i.e. the L-J or 6–12 potential, which has extensively been applied in a wide range of research. Because the L-J potential is a pair potential, i.e. two-body potential, which does not incorporate the many-body effect, there are some inherent drawbacks. For example, the pair potential of metals neither has environmental dependence nor accounts for the directional nature of the bonding. The L-J potential could therefore be a first choice for studies, in which the focus is on fundamental and qualitative issues, rather than on properties of a specific material. In the 1980s, significant progress was made by developing many-body potentials, especially for metals, based on the concept of the local electron density [104]. The main physical feature of a many-body potential is that the bonds become weaker when the local environment becomes more crowded. A variety of interatomic potentials have now been developed and are currently used in computational materials science, such as the embedded atom method (EAM) [104-106], the modified embedded atom method (MEAM) [107,108], the Finnis–Sinclair potential (F–S) [109], and the second moment approximation of tight-binding potential (TBSMA) [110]. Even if they share some similar analytical forms, these models differ vastly in the procedures to build the potential functions, often resulting in rather different parameterizations for the same material. In many cases, researchers could guess the functions and fit the parameters to available and reliable experimental data.

### **2.3.1 MATHEMATICAL ANALYSIS OF MD**

In order to recall the basic principles of the MD, we will give a systematic representation of MD for the simple case of a simulation in micro-canonical statistical ensemble, i.e. an

isolated system of  $N$  atoms contained in a volume  $\Omega$  having energy  $E$ . Assuming that we deal with a classical system, i.e. that the phenomena we shall study are not influenced from QM effects and so the simulations are meaningful for temperatures above the Debye temperature of the material and the examined phenomena cannot be faster than  $10^{-16}$  sec. Under these conditions, we apply Newtonian dynamics for  $N$  particles contained in a box of volume  $\Omega$  and which is repeated periodically in order to simulate an infinite system. We have therefore  $3N$  coupled differential equations which we solve numerically:

$$m \frac{d^2 r_i}{dt^2} = F_i \quad (11)$$

To solve these we need  $6N$  initial conditions. Since we are dealing with solid state systems, we can use the  $3N$  lattice positions of the atoms, and  $3N$  initial velocities which can be selected from a random distribution of Maxwell-Boltzmann, so that the mean momentum of the particles corresponds to the temperature at which we want to perform the simulation. As integration step we select one that is about one hundred times smaller than the inverse of the maximum oscillation frequency of the atoms. An evaluation of this value is the maximum phonon frequency of the material under study.

The successive integrations of the equations of motion produce the trajectory of the system in the phase space, i.e. the positions and velocities of the atoms for the duration in which the system was simulated. The processing of these quantities with the aid of statistical thermodynamics allows for the calculation of thermodynamic equilibrium parameters, such as temperature, pressure, local density distribution function and many useful dynamic quantities like phonon density of states, memory functions, etc.

For example, the temperature of the system is calculated as follows:

$$T = \frac{2}{3Nk_B} \left\langle \sum_{i=1}^N \frac{P_i^2}{2m_i} \right\rangle \quad (12)$$

where  $k_B$  is the Boltzmann constant,  $N$  the number of atoms,  $P_i$  the momentum of atoms and  $m_i$  their mass. And the system pressure can be calculated using the Virial theorem:

$$P = \left\langle \frac{N}{\Omega} k_B T \right\rangle - \left\langle \frac{1}{3\Omega} \sum_{i=1}^N \sum_{j=1}^N r_{ij} \frac{\partial \Phi(r_{ij})}{\partial r_{ij}} \right\rangle \quad (13)$$

where  $\Omega$  is the system volume,  $\Phi(r_{ij})$  is the interaction potential between atoms  $i$  and  $j$  and  $r_{ij}$  is their distance.

The described MD simulation technique refers to micro-canonical statistical ensemble. The method can be easily extended to the isothermal canonical ensemble considering a virtual variable,  $s$ , that scales the real time [111]. There are various schemes for simulations of this type. Here we present the first appeared in the literature by Nose. The corresponding Hamiltonians as well as the equations of motion are derived from:

The Hamiltonian of the micro-canonical ensemble is:

$$H = \sum_{i=1}^N \frac{P_i^2}{2m_i} + \Phi(r_{ij}) \quad (14)$$

In the isothermal canonical statistical ensemble we consider a virtual variable for the time

$t' = \int \frac{dt}{s}$  and the other variables become  $r'_i = r_i$ ,  $P'_i = \frac{P_i}{s}$ . Thus, the Hamiltonian is:

$$H = \sum_{i=1}^N \frac{P_i^2}{2m_i s^2} + \Phi(r_{ij}) + \frac{P_i^2}{2Q} + g k_B T \ln s \quad (15)$$

In these relations,  $\Phi(r_{ij})$  represents the potential interaction between the atoms  $i$  and  $j$  and  $P_i$  and  $r_i$  are the momentum and positions of particle  $i$ , respectively. The variable  $P'$  and  $r'$  are scaled variables associated with the constant  $Q$  which has the role of the pseudo mass of the Nose scheme. This hypothetical mass determines the dynamics of the temperature fluctuations, and its value should be selected properly so that the physical quantities will be reproduced satisfactorily ensuring constant enthalpy of the system. Finally,  $g$  is the degrees

of freedom of the system and the constant  $k_B$  is the Boltzmann constant.

In the general case of isothermal and isobaric statistical ensemble (NPT), the equations of motion are:

$$\frac{d^2 r_i}{dt'^2} = -\frac{1}{m\Omega^{1/3}} \frac{\partial \Phi}{\partial r_{ij}'} - \frac{1}{s} \frac{ds}{dt'} \frac{dr_i}{dt'} - \frac{2}{3} \Omega \frac{d\Omega}{dt'} \frac{dr_i}{dt'} \quad (16)$$

$$\frac{d^2 s}{dt'^2} = -\frac{s}{Q} \Omega^{2/3} \sum_{i=1}^N m_i \left( \frac{dr_i}{dt'} \right)^2 - \frac{gK_B T s}{Q} + \frac{1}{s} \left( \frac{dr_i}{dt'} \right)^2 \quad (17)$$

$$\frac{d^2 \Omega}{dt'^2} = -\frac{s^2}{3WQ^{1/3}} \sum_{i=1}^N m_i \left( \frac{dr_i}{dt'} \right)^2 - \frac{s^2}{3WQ} + \frac{1}{s} \sum_{i=1}^N r_i' \frac{\partial \Phi}{\partial r_i'} + \frac{1}{s} \frac{ds}{dt'} \frac{d\Omega}{dt'} - P_{ext} \frac{s^2}{W} \quad (18)$$

where  $P$  and  $T$  in the above formulas represent the external pressure and temperature respectively.

### 2.3.2 POTENTIAL MODEL BASED ON THE TIGHT BINDING SCHEME IN SECOND MOMEND APPROXIMATION

The key of a realistic simulation is the interactions between atoms. The form of the potential we used is a Rosato-Guillope-Legrand (RGL) [112] type and it is in analogy to the TBSMA [110]. The equations of motion were integrated using the Verlet algorithm with integration step of 5 fs. The total energy of the system is given by:

$$\Phi = \sum_{\alpha} \sum_{i_{\alpha}=1}^{N_{\alpha}} \left\{ \sum_{\beta} \sum_{\substack{j_{\beta}=1 \\ j_{\beta} \neq i_{\alpha}}}^{N_{\beta}} A_{\alpha\beta} \cdot e^{-\rho_{\alpha\beta} \left( \frac{r_{ij}^{\alpha\beta}}{d_{\alpha\beta}} - 1 \right)} - \sqrt{\sum_{\beta} \sum_{\substack{j_{\beta}=1 \\ j_{\beta} \neq i_{\alpha}}}^{N_{\beta}} \xi_{\alpha\beta}^2 \cdot e^{-2q_{\alpha\beta} \left( \frac{r_{ij}^{\alpha\beta}}{d_{\alpha\beta}} - 1 \right)}} \right\} \quad (19)$$

where  $\alpha$  and  $\beta$  refer to two different kinds of atoms and  $r_{ij}^{\alpha\beta}$  is the distance between  $i_{\alpha}$  and  $j_{\beta}$  atoms, while the indices  $i_{\alpha}$  and  $j_{\beta}$  run on all individuals.

From both terms of the potential, the term:

$$\sum_{\beta} \sum_{\substack{j_{\beta}=1 \\ j_{\beta} \neq i_{\alpha}}}^{N_{\beta}} A_{\alpha\beta} \cdot e^{-p_{\alpha\beta} \left( \frac{r_{ij}^{\alpha\beta}}{d_{\alpha\beta}} - 1 \right)} \quad (20)$$

is the term having the character of many-body interactions, while the term:

$$\sum_{\beta} \sum_{\substack{j_{\beta}=1 \\ j_{\beta} \neq i_{\alpha}}}^{N_{\beta}} \xi_{\alpha\beta}^2 \cdot e^{-2q_{\alpha\beta} \left( \frac{r_{ij}^{\alpha\beta}}{d_{\alpha\beta}} - 1 \right)} \quad (21)$$

stands for the repulsive interaction between pairs of atoms (Born-Mayer type). The parameter  $d$  is the distance of the first neighbours and, the parameters  $p$ ,  $q$ ,  $A$  and  $\xi$  are usually adjusted to available experimental values of cohesive energy, elastic constants, lattice constants of the pure elements and their alloys. In table 6 is give the TBSMA parameters we used for the Cu-Zr systems simulation.

**Table 6** - [80]  
Parameters for the RGL-type potential of Cu-Zr

Bond type	$d$ (Å)	$A$ (eV)	$\xi$ (eV)	$p$	$q$
Zr - Zr	3.2100	0.3688	2.3365	7.9273	2.0250
Cu - Cu	2.6356	0.2149	1.3483	10.2215	2.7490
Zr - Cu	2.9086	0.3615	2.0100	8.6020	2.7960

## 2.4 SYSTEMS PREPARATION

We studied a wide range of alloys: Zr<sub>20</sub>Cu<sub>80</sub>, Zr<sub>30</sub>Cu<sub>70</sub>, Zr<sub>35</sub>Cu<sub>65</sub>, Zr<sub>40</sub>Cu<sub>60</sub>, Zr<sub>46</sub>Cu<sub>54</sub>, Zr<sub>50</sub>Cu<sub>50</sub>, Zr<sub>54</sub>Cu<sub>46</sub>, Zr<sub>60</sub>Cu<sub>40</sub>, Zr<sub>65</sub>Cu<sub>35</sub>, Zr<sub>70</sub>Cu<sub>30</sub>, Zr<sub>80</sub>Cu<sub>20</sub>, Zr<sub>50</sub>Cu<sub>40</sub>Al<sub>10</sub> and Zr<sub>30</sub>Cu<sub>65</sub>Al<sub>5</sub>. All binary systems were simulated by means of two potential schemes, the Tight Binding potential in the Second Moment Approximation (TBSMA) and the Embedding Atom Method (EAM) [113], while for the ternaries we used the EAM potential. Each simulated system consisted of several thousands of atoms; the TBSMA simulated systems consisted of

128,000 atoms, while the binary and ternary EAM systems of 78,608 and 54,000 respectively. As starting point, these atoms were placed in a B2 grid (a representative structure is given in Fig. 12) and we applied periodic boundary conditions in three directions.

Aiming in the simulation of the process of metallic glasses formation by rapid quenching, we had to solidify these systems from a higher of their melting point temperature ( $T_m \approx 1200$  K) down to room temperature (300 K (RT)) applying a high cooling rate. Thus, we started by bringing our systems in liquidus form, temperature 2000K where we equilibrated them for more than 25ps. Subsequently, we reduced gradually the systems' temperature down to RT imposing a cooling rate of 2.5K/ps. The cooling rate is by orders of magnitude larger than the experimental one ( $\sim 1$  K/ms) because the use of a more realistic cooling rate would require enormous computational time. Naturally, this high cooling rate may affect the structural features of the systems but the essential structural characteristics are expected to be reproduced satisfactorily. Finally, we equilibrated the produced bulk systems for 50ps or more.

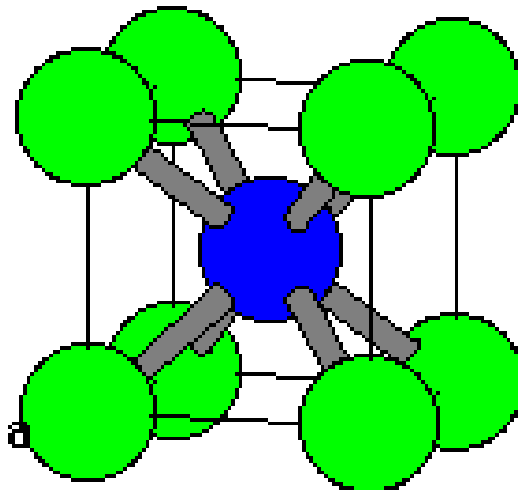


**Figure 12.** Schematic representation of the B2 (CsCl) structure.

### 3 STRUCTURAL STUDY OF THE SYSTEMS

#### 3.1 RADIAL DISTRIBUTION FUNCTION (RDF)

The basic method for recording structure characteristics of a simulated system is the pair Radial Distribution Function (RDF) [114]. It is a pair correlation representing the probability of finding atoms as a function of distance  $r$  from an average central atom. The distribution of interatomic distances, the shell-like structure in the radial direction, and its fading out with increasing distance, can be clearly seen in the RDF of a liquid/glass. The  $\alpha$ - $\beta$  partial RDF (i.e., the element-specific RDF) is defined as [115]:

$$g_{\alpha\beta}(r) = \frac{V}{N_{\alpha}N_{\beta}} \left\langle \sum_{i=1}^{N_{\alpha}} \frac{n_{i\beta}(r)}{4\pi r^2 \Delta r} \right\rangle \quad (22)$$

where  $N_{\alpha}$  and  $N_{\beta}$  is the number of atoms of element A and B respectively,  $V$  is the volume of the cell and  $n_i(r)$  is the number of the atoms that found in the spherical shell of thickness  $\Delta r$ . If the species are not differentiated, or in a monatomic system, we have [115]:

$$g(r) = \frac{V}{N^2} \left\langle \sum_{i=1}^N \frac{n_i(r)}{4\pi r^2 \Delta r} \right\rangle \quad (23)$$

As an example, in a crystalline solid such as FCC, if we consider  $D$  the diameter of the hard spheres that we consider as distributed atoms in a dense array, then  $D$  is the distance between the nearest neighbours in the lattice. First let us consider a very thin spherical shell with variable radius  $r$  located at an occupied grid position. As the radius increases, starting from  $r = 0$ , the shell surface is increasing too, but it does not intersect neighbouring lattice sites just until  $r = D$ . The spherical shell with radius  $D$  intersects the first 12 neighbours of the FCC lattice; 12 is substantially the coordination number, i.e. the number of atoms in the first neighbourhood. If we continue increasing the radius the spherical shell will intersect a second set of grid positions, the second neighbourhood. With similar considerations as the

value of the radius increases in the cases of perfect crystals we are able to identify the third, fourth and further neighbours. Beyond the twelfth neighbourhood the identification is not easy because the boundaries of neighbourhoods are coming very close, thus becoming significantly blurred.

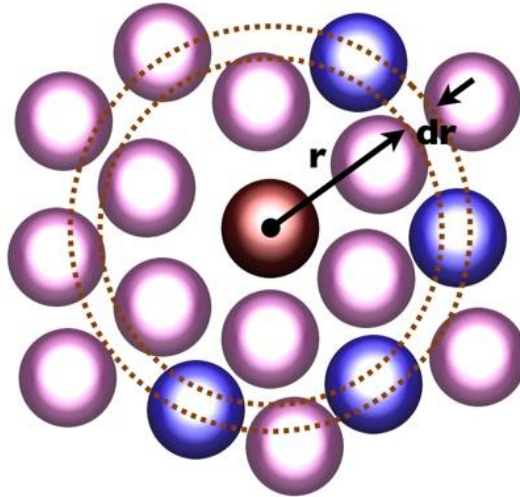


**Figure 13.** Schematic representation of finding the neighbours of a central atom at a distance  $r + dr$ .

Using the RDF one can identify the system's structure as each neighbourhood are represented by a defined peak and the distances between them denote the distances between neighbours. Specifically, the first peak corresponds to the distance of the nearest neighbours, while the area below the first peak corresponds to the number of the occupied sites, i.e. atoms. If the material is homogeneous and uniform, the partial RDFs would be very helpful in reconstructing the 3-D structure. Two indicative RDFs of a crystalline and an amorphous structure equilibrated at RT are presented in the following figure.

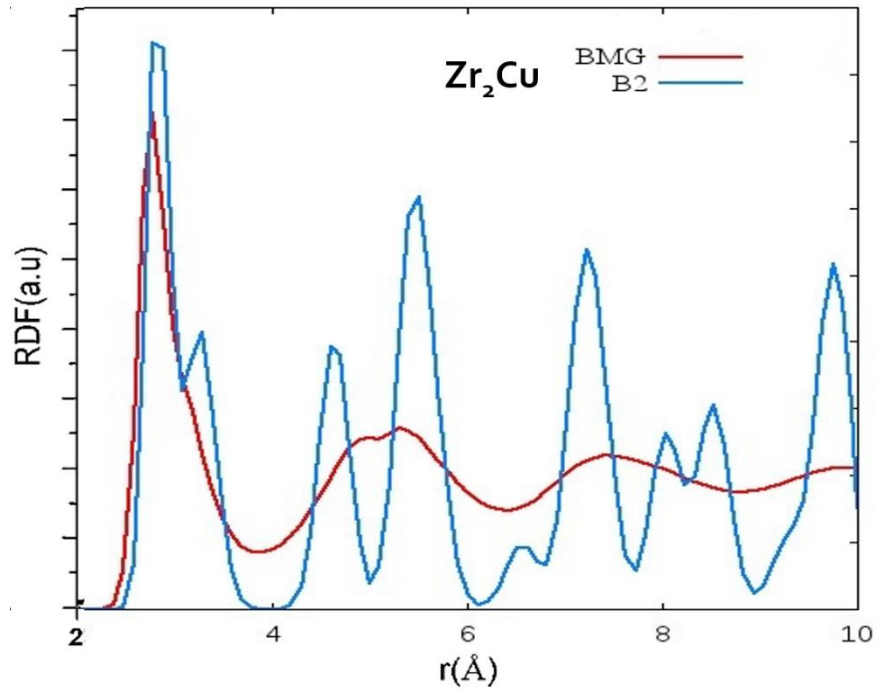


**Figure 14.** Representative RDFs of the crystalline B2 structure (blue line) and the relative BMG (red line)

The RDF is directly related to partial structure factors in reciprocal space via Fourier transformation [115]:

$$S(Q) = 1 + \rho_0 \int [g(r) - 1] e^{-iQr} dr \quad (24)$$

where  $\rho_0$  is the mass density of the system and  $Q$  is the variable in the reciprocal space, which, in an X-ray scattering experiment, corresponds to the magnitude of the diffraction vector ( $4\pi \sin \theta / \lambda$ ). With the structure factor measured in an X-ray or neutron experiment, one can perform Fourier transformation to obtain the RDF in real space.

### 3.2 COORDINATION NUMBER (CN)

The coordination number (CN) is the number of atoms that are in the nearest-neighbour distance. For network glass with covalent bonding, a low CN value (e.g., CN = 4) is common (open environment), while for MGs with metallic bonding and dense packing, a

high CN (e.g., CN = 12) is expected. There are several different ways to identify the nearest neighbours, such as the distance cutoff method and Voronoi tessellation method. For example, by setting a cutoff in the RDF (usually at the minimum after the first peak), all atoms contributing to the first peak (up to the cutoff distance) are considered nearest neighbours. A specific cutoff can be assigned for each partial RDF to obtain the partial CN. The nearest neighbours contributing to the CN are often regarded as “bonded”. A “bond” drawn between two atoms has clear physical meaning for covalent glasses, but not for MGs, because metallic bonds are not localized in nature, and the bonding electrons are itinerant rather than shared by the atom pair only.

### **3.3 COMMON NEIGHBOR ANALYSIS (CNA)**

Common Neighbour Analysis (CNA) [116,117] is a widely used method for accessing the microstructure of simulated systems. The information one can derive from CNA is mostly confined to the study of the short-range order and so the location of the first minimum, usually provided by the RDF (r-cutoff,  $r_c$ ), which generally defines the limit of the first neighbourhood, is used as the upper limit for the analysis. CNA provides information about every bond between a couple of atoms and their neighbourhood within a sphere with radius  $r < r_c$ . It should be noted here that we refer to each “atomic couple” simply suggesting a geometric rather than a chemical bond. Every atomic couple is represented by a set of three indices **jkl** which define the local environment.

- 1) The index **j** represents the number of common neighbours for the coupled atoms
- 2) The index **k** is the bonds between these common neighbours
- 3) The index **l** is the number of the bonds in the longest possible chain composed by the **k** bonds of the common neighbours.

Table 7 provides the CNA indexes of some known structures.

It should be noted here that CNA is a very strict process regarding the criteria of finding local structures. This led us to use a second, more flexible, method for identifying clusters of the system, the High Symmetry Centre Method.

**Table 7** – [118]  
CNA jkl indexes for various structures.

Environment	# of CNA bonds	1 <sup>st</sup> index set (#)	2 <sup>nd</sup> index set (#)	3 <sup>rd</sup> index set (#)	4 <sup>th</sup> index set (#)	5 <sup>th</sup> index set (#)
FCC bulk (a)	12	421 (12)				
FCC (100) surface (b)	8	421 (4)	211 (4)			
FCC (111) surface (c)	9	421 (3)	311 (6)			
FCC (111)-(100) edge (d)	7	421 (2)	311 (2)	211 (3)		
FCC (111)-(111) edge (e)	7	421 (1)	311 (4)	200 (2)		
truncated octahedron vertex <sup>a</sup> corner (f)	6	421 (1)	311 (2)	211 (2)	200 (1)	
icosahedral internal twinning plane (g)	12	422 (6)	421 (6)			
icosahedral spine <sup>b</sup> (h)	12	555 (2)	422 (10)			
icosahedral surface edge (i)	8	422 (2)	322 (2)	311 (4)		
icosahedral central atom (j)	12	555 (12)				
icosahedral surface vertex or decahedral axial vertex (k)	6	555 (1)	322 (5)			
truncated icosahedral vertex or decahedral notch vertex <sup>c</sup> (l)	7	422 (1)	322 (1)	311 (2)	300 (1)	200 (2)
decahedral notch edge <sup>d</sup> (m)	10	422 (2)	421 (2)	311 (4)	300 (2)	
tetrahedral edge (n)	6	311 (4)	211 (2)	311 (4)	300 (2)	
BCC bulk (o)	14	666 (6)	444 (8)			

### 3.4 HIGH SYMMETRY CENTERS

In order to obtain information of as many as possible clusters existing in our systems and taking into account that most of them may be distorted and/or truncated, we used as prototypes perfect shaped 13-atom Icosahedral (ICO), 13-atom Cuboctahedral (CO), 13-atom truncated Tetrahedral (TT), 15-atom Rhombic Dodecahedral (RD) and 21-atom

Dodecahedral (DH) clusters and we analyse our configurations according to the following procedure.

For each system, we considered every atom as a potential centre of a cluster and we looked in its first neighbourhood for atoms that could match one of these prototypes. The procedure involved non-linear fitting. As objective function we considered the root mean square of the distances,  $R$ , between the locations of all atoms of a candidate cluster from the atoms of each prototype cluster. In this way the fitting of the cluster atoms are permitted to have deviations from their perfect positions. In fact, the quantity  $R$  provides information about the amount of deformation of the candidate cluster. Indeed, taking into account that the average bond length in these systems is about  $2.8\text{\AA}$  and that the first neighbourhood extends up to  $3.4\text{\AA}$ , a bond length change of  $0.3\text{\AA}$  would result in  $R$  value of  $0.52\text{\AA}$  corresponding to a cluster deformation of about 10%. In addition, we allowed the consideration of truncated clusters accepting candidate clusters having up to 25% non-well-fitted atoms, e.g. we considered 10 atoms for a 13-atoms cluster or 11 for a 15-atoms RD as being sufficient for the fitting. This compromise increases the number of possible clusters without affecting qualitatively the results. The procedure yielded Gaussian-like distributions of possible clusters as a function of  $R$ , which in fact is the Root Mean Square (RMS) error of the candidate clusters from the perfect prototype configurations. We adopted to accept a cluster when the (RMS) effective distance was less than the full width at half maximum of the error distribution. We note here that although this choice appears somehow arbitrary, it affects only the absolute number of the clusters, their relative occurrences remaining unaltered. It turns out that most of the systems' atoms may be considered as centres of a possible cluster and that around 45% of them are under significant strain that exceeds 10%. Two representative clusters for the case of ICO and RD symmetry are presented in Fig. 15.

A verification of the procedure was done by performing CNA that yielded that the method was apt in capturing all cases of perfect clusters.

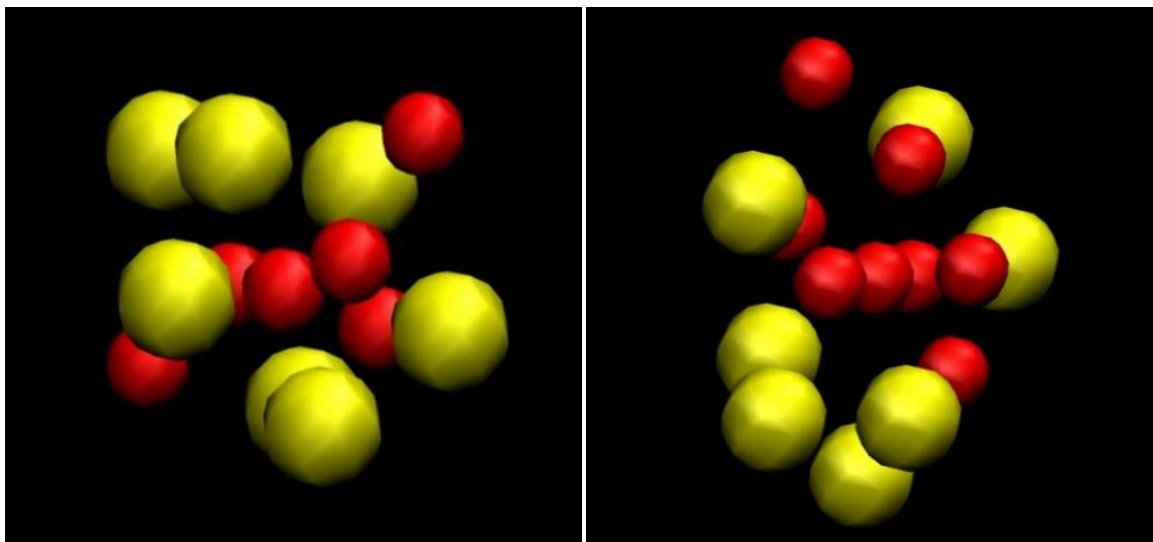


**Figure 15.** On the left is presented a typical Icosahedral 13-atoms cluster while on the right is shown a Rhombic-dodecahedron 15-atoms cluster. The yellow spheres stand for Zr atoms while the red one for Cu.

## 4 RESULTS

### 4.1 THE BASIC STRUCTURAL CHARACTERISTICS OF Cu-Zr

In order to reveal the structural correlation of metallic glasses with the system's stoichiometry and temperature, the first step of our study on  $\text{Cu}_x\text{-Zr}_{(100-x)}$  was to investigate in depth the presence of the familiar Icosahedral (ICO) clusters upon the solidification process. We examined in depth seven of the TBSMA simulated stoichiometries ( $x = 20, 30, 40, 50, 60, 70$  and  $80$ ) at 18 different temperatures, i.e. every 100K upon cooling from 2000K to 300K. Conducive to assess the microstructure characteristics and to verify the glassy nature of our simulated systems, we calculated their RDF at RT. As we can see by the RDFs of some representative compositions in Fig. 16, our Cu-Zr systems exhibit typical amorphous characteristics unheedingly to the stoichiometry, demonstrating the remarkable preference of these alloys for amorphization. Moreover, the existence of peaks in short distances in the RDFs reflects the existence of first and second neighbourhood and is pointing directly to the presence of short- and medium-range order in these systems. The stoichiometry's influence in the microstructure is also apparent by the shift of the positions of the total RDF peaks to shorter distances upon Cu increment. As we are going to show later, the origin of what we see as shift is not the changes of the bonds' distances but it originates by the increment of the Cu-Cu bonds against to Zr-Zr bonds. In fact, this provides a strong indication that the alteration of the elemental ratio, due to stoichiometry changes, influences significantly the resulting microstructure of the glass and apparently, its GFA.

Therefore, in order to understand the correlation of the stoichiometry with the GFA it is essential to gain further insight about the details of the fine structure of the developed glassy systems. Hence, we performed detailed Common Neighbour Analysis (CNA) [116,117] in every system and the analysis shown that 555 was the prevailing index in all stoichiometries,

while further detailed inspection of the results confirmed the presence of ICO 13-atom clusters, in line with previous studies [119]. It is remarkable that in all compositions studied, approximately 25% of the atoms belong into these perfectly shaped ICO clusters. This fact amplifies their important role in the short-range order of these glasses and explains the good GFA exhibited by all Cu-Zr alloys.

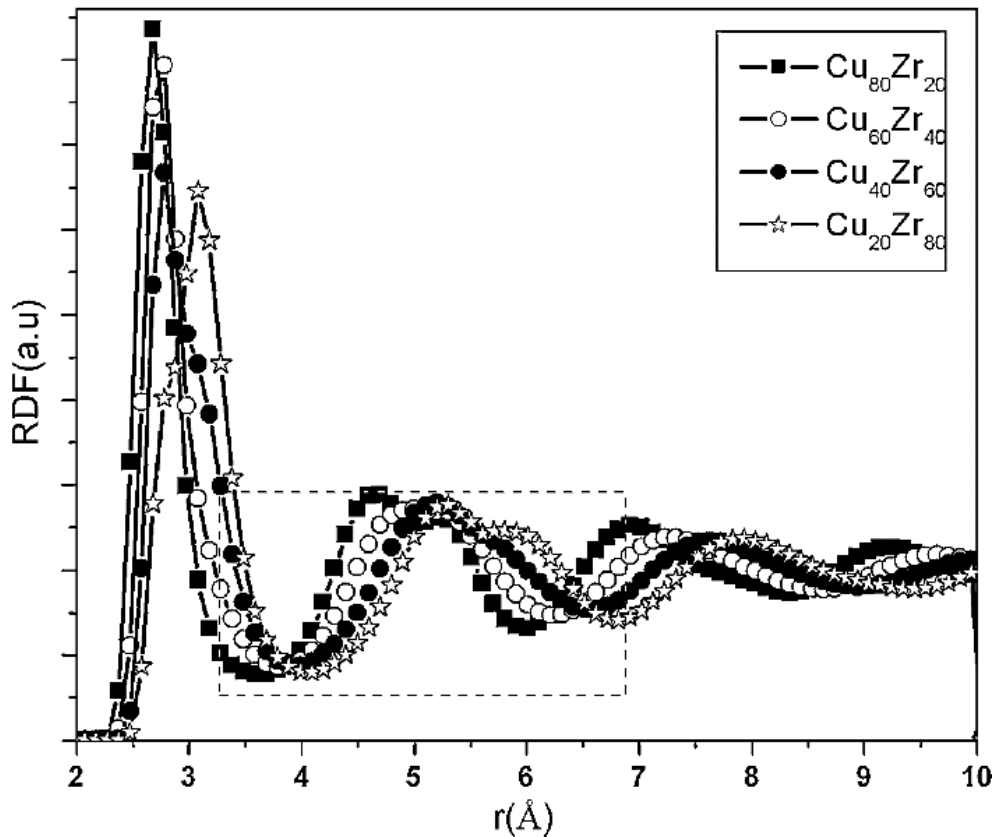
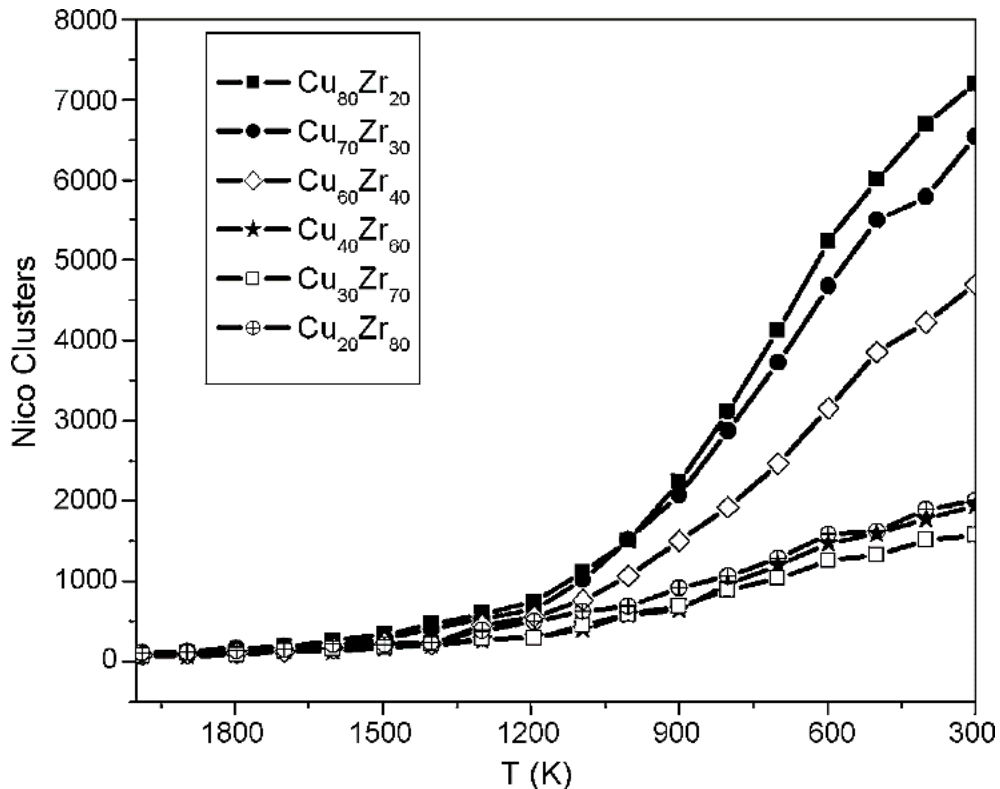


Figure 16. Radial distribution functions for various stoichiometries [120]

After revealing the glassy nature of all systems at RT, we proceeded in the detailed structural analysis of the configurations acquired during the solidification process. For each one of the stoichiometries studied, we calculated the population of the ICO clusters every 100K and we plotted their evolution as a function of the temperature (Fig. 17). It turns out that in all compositions the population of ICO clusters increases as the temperature drops. Again, this result is in agreement with recent findings according to which the number of

pentagons as counted by a Voronoi analysis increases upon cooling resulting in microstructural changes of the glass. What we must notice is the significant change of the ICO clusters population that takes place between  $T_m$  and  $T_g$  delineating the temperature region where the major change in the microstructure takes place upon the system's transformation. Another important remark refers to the apparent correlation between the population of the ICO clusters and the Cu percentage of the system (Fig. 18). We evaluated this correlation for the various stoichiometries at RT and we can conclude that Cu enrichment favours the formation of ICO clusters. This fact is directly correlated with the shift of the peaks in Fig. 16 explicating the tendency of Cu to form more dense structures and more specifically, in the case of MGs, it enhances the formation of ICO clusters.



**Figure 17.** Temperature evolution of the number of icosahedral clusters ( $N_{ICO}$ ) upon cooling [120]

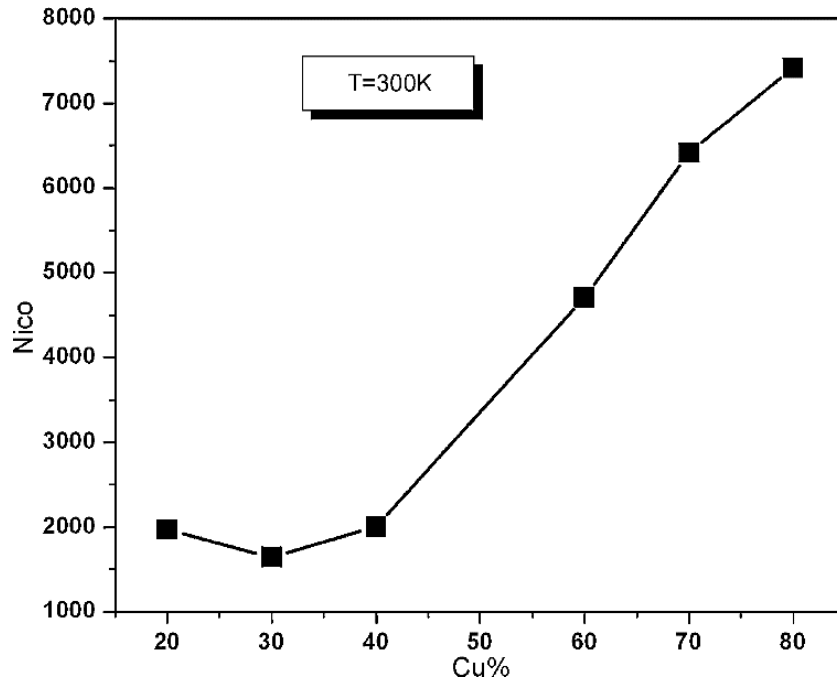


**Figure 18.** Concentration dependence of the number of icosahedral clusters ( $N_{ICO}$ ) at 300K [120]

Aiming in resolving the role of Cu in the formation of these 13-atoms ICO clusters, we calculated, for all compositions, the average numbers of Cu-centred and Zr-centred clusters along with their compositions; the results are gathered in Table 8. It came out that Cu-centred ICO clusters are much more preferred compared to the Zr-centred, in an abundance that in the case of Cu-rich systems approaches 100%; only exception is the  $Cu_{20}Zr_{80}$  system, which is very pure in Cu favouring Zr-centred clusters. Interestingly, we can notice that independently of the cluster's centre, the composition of the clusters seems to be correlated with the stoichiometry of the system; this is more apparent in Zr-rich systems in which the statistics are better, due to the significant abundance of the Zr-centre clusters. The fact that Cu atoms are unquestionably preferred as centres for the ICO cluster, even in Zr-rich systems albeit their small percentage in the clusters, is nevertheless indicative for the ICO cluster forming ability of this element. Moreover, considering the high packing of the ICO clusters, in conjunction with their tendency in Cu enrichment, this finding explains also why the Cu-rich compositions exhibit lower free volume than the Zr-rich counterparts [119].

**Table 8** – [120]

Number of Cu and Zr-centred ICO clusters, along with the average cluster atomic compositions

Composition	Cu-ICO			Zr-ICO		
	Abundance (%)	Average Cluster stoichiometry		Abundance (%)	Average Cluster stoichiometry	
		Cu atoms	Zr atoms		Cu atoms	Zr atoms
Cu <sub>80</sub> Zr <sub>20</sub>	99.6	9.9	3.1	0.4	11.6	1.4
Cu <sub>70</sub> Zr <sub>30</sub>	99.3	8.4	4.6	0.7	10.0	3.0
Cu <sub>60</sub> Zr <sub>40</sub>	98.7	7.1	5.9	1.3	8.3	4.7
Cu <sub>40</sub> Zr <sub>60</sub>	89.1	4.6	8.4	10.9	4.7	8.3
Cu <sub>30</sub> Zr <sub>70</sub>	65.9	3.3	9.7	34.1	3.0	10.0
Cu <sub>20</sub> Zr <sub>80</sub>	30.2	2.2	10.8	69.8	1.7	11.3

Taking into account the transferability issues related with the potential model we used, in particular when dealing with systems of lower dimensions and in order to validate the findings of the MD simulations, we validated our analysis by performing DFT calculations for the ICO clusters that were resolved from the semi-empirical computations. We performed energy minimization in all ICO clusters studied and the results are gathered in Table 9.

**Table 9** – [120]

DFT binding energies for the ICO clusters studied; (\*) indicates Zr centred cluster.

Composition	MD simulation	DFT binding energy (eV)	
	Cu-ICO clusters	Cu-centred	Zr-centred
Cu <sub>80</sub> Zr <sub>20</sub>	Cu <sub>10</sub> Zr <sub>3</sub>	- 4.744	- 4.957
Cu <sub>70</sub> Zr <sub>30</sub>	Cu <sub>8</sub> Zr <sub>5</sub>	- 5.389	- 5.528
Cu <sub>60</sub> Zr <sub>40</sub>	Cu <sub>7</sub> Zr <sub>6</sub>	- 5.730	- 5.667
Cu <sub>40</sub> Zr <sub>60</sub>	Cu <sub>5</sub> Zr <sub>8</sub>	- 6.313	- 6.255
Cu <sub>30</sub> Zr <sub>70</sub>	Cu <sub>3</sub> Zr <sub>10</sub>	- 6.928	- 6.854
Cu <sub>20</sub> Zr <sub>80</sub>	*Cu <sub>2</sub> Zr <sub>11</sub>	- 7.288	- 7.238

We can see that with the exception of the last two Cu-rich cases the DFT results are in agreement with the MD findings. Nevertheless, even this exception does not necessarily reflect deficiency of the semi-empirical model used; we have to point out that all DFT computations refer to free-standing clusters, while the MD simulations concern clusters that may be touching and/or interpenetrating each other and in any case embedded in the amorphous environment of the glassy matrix, suggesting that the elemental concentration of

the latter may also play a significant role in the cluster's composition. In addition, in Figs. 19a and b we present the electronic charge distributions at the HOMO states for a representative ICO cluster from every system studied. In all cases it is visible that the Zr–Zr and/or Zr–Cu orbital overlap is favoured compared to the Cu–Cu, suggesting stronger atomic bonding in the former type of interactions.

Combining the results from our MD simulations and DFT calculations, we can say that in the Cu-Zr systems the formation of ICO clusters depends on the existence of Cu atoms, as their small size enhances the efficient packing model and therefore they are preferred as centres. Moreover, the Zr atoms play important role concerning the stability of the clusters due to the strong Zr-Zr and Zr-Cu interactions. The importance of the formation of the ICO clusters in the resulting microstructure, as well as the correlation of the nature of their bonds with the stability of the Cu-Zr systems, must play an important role in the distortion of the systems during solidification and probably, during deformation too.

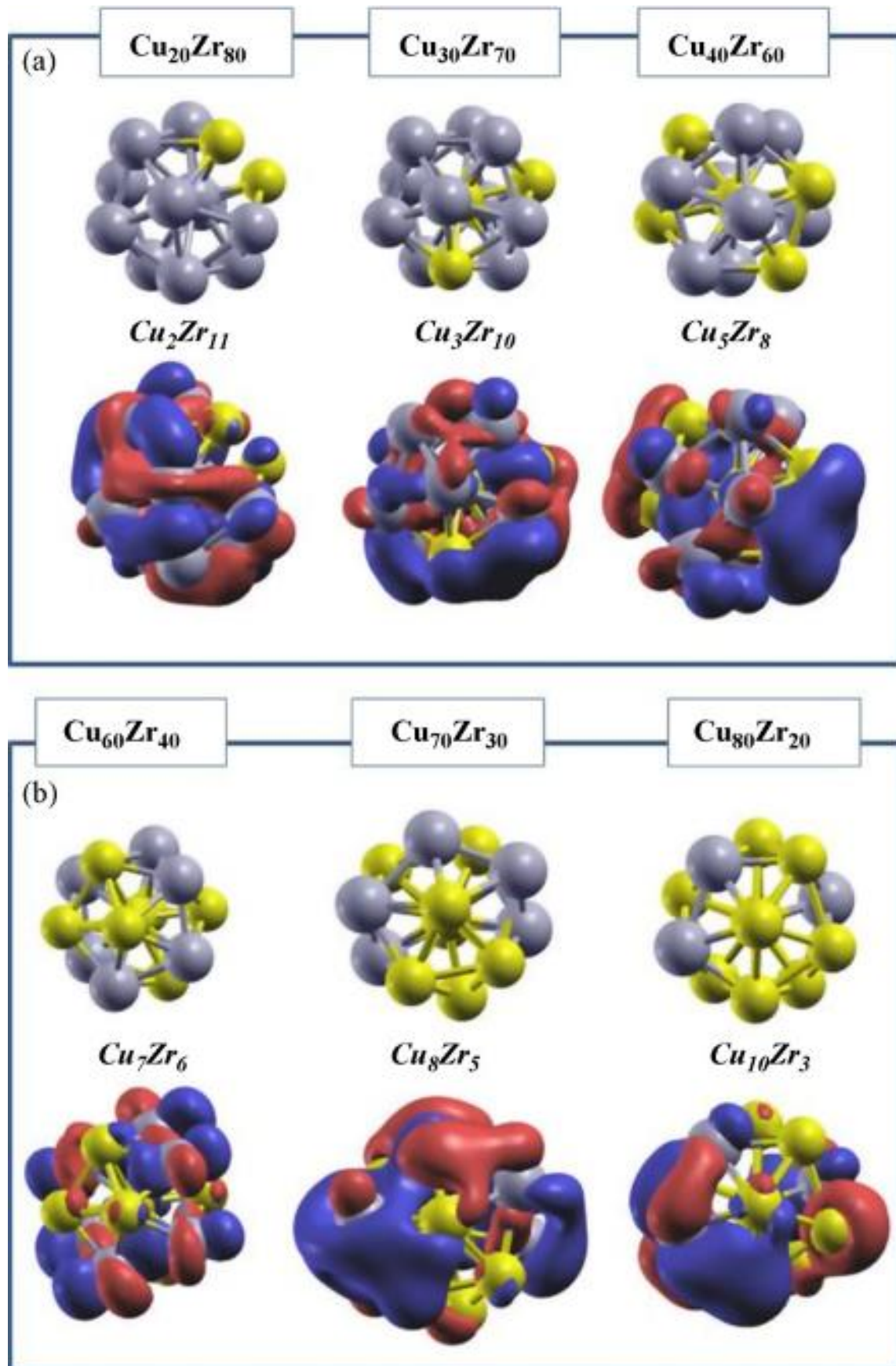


**Figure 19.** ICO clusters studied by DFT along with their ISO-surface electronic charge distributions. [120]  
 (a) Zr-rich; (b) Cu-rich

## 4.2 ON THE ROLE OF ICO-LIKE CLUSTERS IN THE SOLIDIFICATION AND THE MECHANICAL RESPONSE OF Cu-Zr MGs

From the MD trajectories analysis of the EAM simulated configurations we have found that upon quenching the ICO clusters population increases, in line with previous studies [120-122], while the systems become denser as illustrated by the decrease of the mean atomic distances. In the case of  $\text{Cu}_{65}\text{Zr}_{35}$  we know that these clusters are mainly Cu-centred and their Cu content ranges mostly from 7 to 9 atoms, with  $\text{Cu}_8\text{Zr}_5$  being the dominant one [121]. We proceeded in a more detailed inspection of the partial bond lengths and it was revealed that these atomic distance changes are due to core-Cu shell and Cu-Cu shell bond shortening, while the Zr-Zr and core-Zr shell bonds remain approximately unchanged (Fig. 20). These results demonstrate that the origin of the clusters' distortion steams not only from their geometrical differences, Zr is almost twice as large as Cu [123], but also from the elemental chemistry and the associated electronic interactions, thus evidencing once more the role of electronic contributions in these processes.

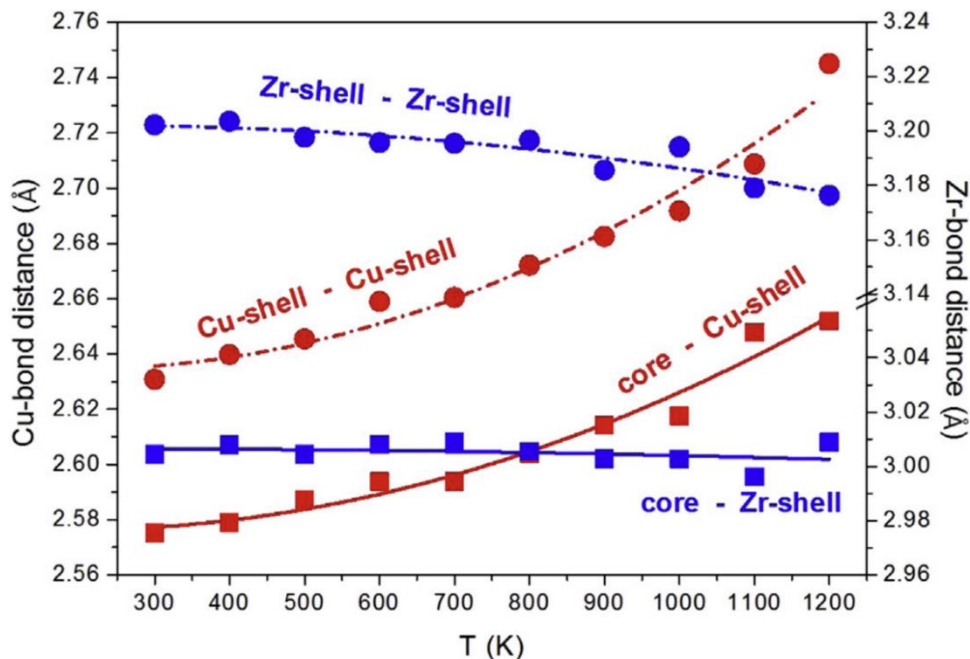


**Figure 20.** Cluster bond lengths in  $\text{Cu}_{65}\text{Zr}_{35}$  MG as a function of temperature upon quenching [124]

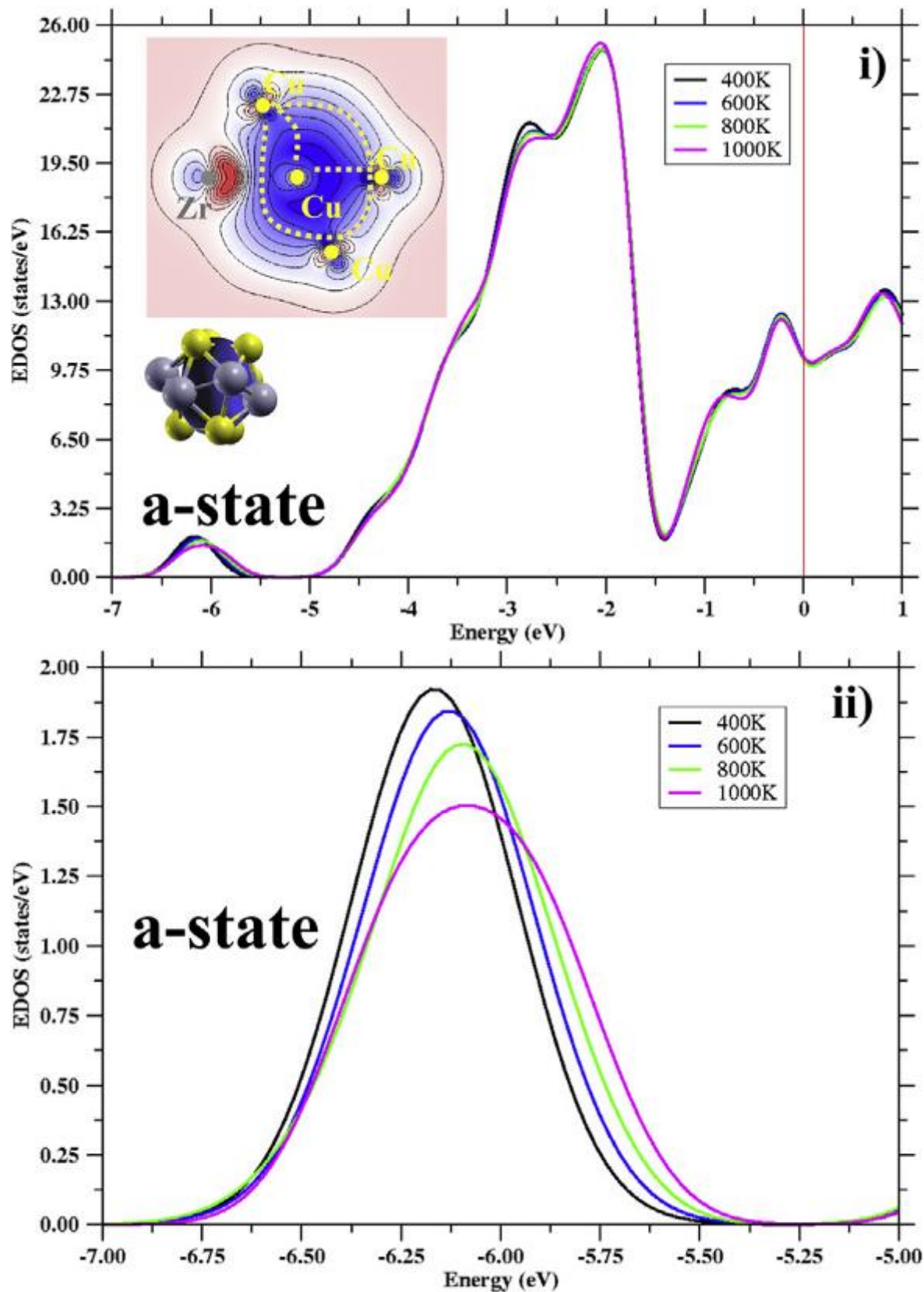


**Figure 21.** i) Averaged EDOS of  $\text{Cu}_8\text{Zr}_5$  ICO clusters and ii) close view of the *a*-state at representative temperatures. The vertical line in Fig. 21.i indicates the Fermi Energy [124]

In order to obtain more insight of the effects of the bond-length changes in the clusters and understand in depth the bonding nature between their atoms, we calculated the averaged electronic density of states (EDOS) of the  $\text{Cu}_8\text{Zr}_5$  clusters. In line with previous work [125], it came out that the density of states in the region between -4 eV and -2 eV are due to Cu-Cu (shell-shell)  $d-d$  hybridization, while the low states are attributed to  $s-s$   $\sigma$ -like strong bonds (denoted as a-state) and  $s-d$  hybridization between the Cu-core and Cu-shell atoms, respectively (Fig. 21.i). A close view of the evolution of the a-state at various temperatures is provided in Fig. 21.ii. We can notice that upon solidification the a-state peak is sharpened and clearly shifted towards lower energies, indicating larger electronic Cu-Cu (core-shell)  $s-s$  overlaps, bond strengthening and therefore shorter bond distances. Similar effect, although less visible, is also found around -4.5 eV corresponding again to core-Cu and Cu-Cu shell atoms, but through  $s-d$  hybridization this time, which also moves towards lower energies. We note at this point that these alterations are also responsible for the changes of the clusters' shape and size [125]. At higher energies and close to the Fermi level, no noticeable changes are visible; atomic bonds at these energies are due to abundant  $d-d$  hybridization between shell atoms and any possible alteration, e.g. in the case of Cu-Cu shell atoms cannot be visible.

Turning to the microscopic mechanisms acting in the accommodation of the mechanical solicitation and the possible alterations induced in the EDOS, we focussed on the TBSMA simulated  $\text{Cu}_{50}\text{Zr}_{50}$  system in order to ensure no influence of the results from any elemental preference, e.g. preferential diffusion or segregation. We applied tensile load with a strain rate of  $10^9$  ( $\text{sec}^{-1}$ ) in one direction and Poisson ratio of 0.34 in the other two. We calculated and averaged the ICO clusters' EDOSes that were extracted from MD simulations trajectories for tensile strains up to 40%. We note here that Cu centred ICO clusters of the same composition (or close to that), although less than in the Zr rich case, are still the

majority in between the cluster types present in the system. The strain-stress curve along with the ICO evolution is depicted in Fig. 22. We can see that

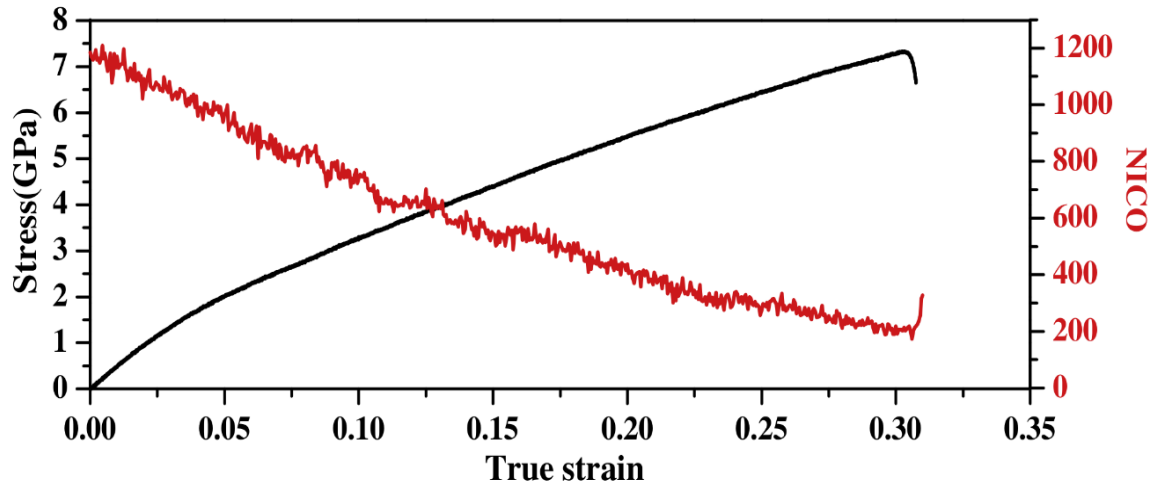


**Figure 22.** Strain-Stress curve for the  $\text{Cu}_{50}\text{Zr}_{50}$  system along with the ICO clusters number evolution. [124]

in the elastic region (up to strain of 2.5%) the ICO clusters number remains constant, in line with previous calculations [126], while in the plastic region there is a continuous decrease of the population of the ICO clusters until fracture that occurs at strain of 32%. Taking into account that the perfect ICO clusters that we are considering in our analysis represent only 10% of the system's atoms and in order to ensure that these findings are representative of the systems response under tensile deformation, we calculated the mean atomic distances in these clusters and the average first neighbour distances obtained from the Radial Distribution Functions (RDF) of the system versus strain (Fig. 23). As we can see, these quantities exhibit almost identical behaviour upon tension. More specifically, inside the elastic region both quantities remain practically constant (ICO clusters are destroyed and recreated with the same rates [126]), while they both exhibit continuous increase with the same slope in the plastic region, followed by a sharp drop at failure.

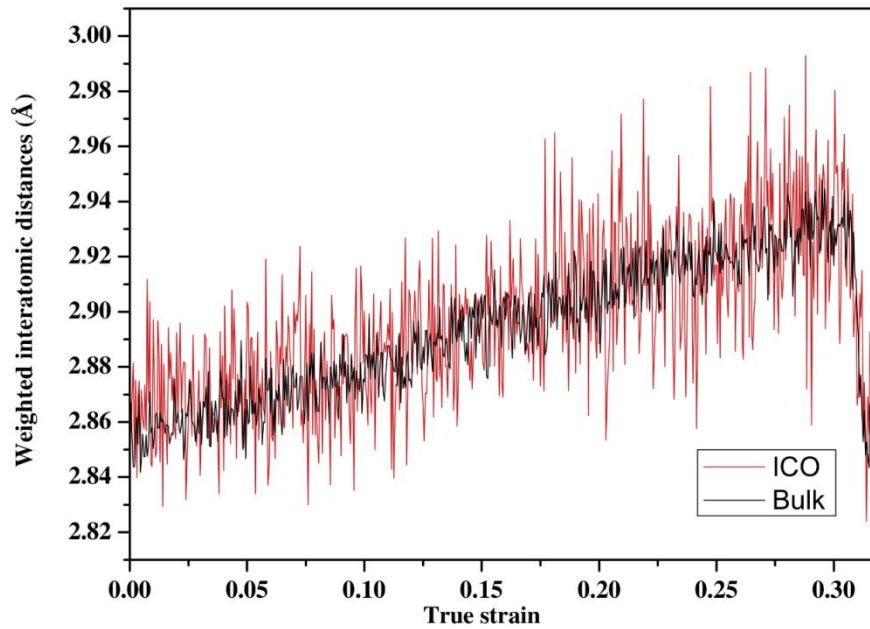


**Figure 23.** Averaged atomic distances in ICO clusters and in the bulk system (obtained from the RDF) under tensile deformation [124]

Aiming in capturing the essence of the microstructural alterations under tensile deformation we also looked at the “distorted” ICO clusters and their evolution. We clarify at this point that by “distorted” we consider ICO clusters that are not identifiable by the CNA at a given strain-step but they were present in just a previous one. It came out that their behaviour is quite similar with the one described for the perfect ICO clusters, the effects being slightly enhanced, while their EDOSes yielded a small shift of the a-state towards higher energies and smaller occupation at the Fermi level, indication of less stable systems.

### ***4.3 ON THE DEPOSITION MECHANISMS AND THE FORMATION OF GLASSY Cu–Zr THIN FILMS***

Solidification by rapid quenching is not the only way to produce a MG. In order to clarify that the nature of the microstructure in the MGs does not depend on the vitrification procedure, we decided to simulate the growth of a Cu-Zr glassy thin film and to investigate the details of the structural evolution during the deposition process. We used as substrate a Cu(111) crystal, consisting of 18432 atoms on top of which we deposited a total of 26600

atoms (40% or 20% Cu) in bunches of 100 atoms every 3000 time-steps. Two different types of depositions were applied: in the first one (D1) the Cu and Zr atoms were landing simultaneously (co-deposition), while in the second (D2) the two elements were deposited sequentially, i.e. in alteration of a few Zr monolayers (ML) followed by some Cu ML. In the latter case, two Cu compositions [40% (D2a) and 20% (D2b)] have been used. The structures of the deposited thin films were evaluated by means of the RDF.

In order to verify our theoretical results, films were also experimentally grown by pulsed laser deposition (PLD) and dual-cathode confocal magnetron sputtering (DCMS). For the PLD experiments three types of targets were employed:

- (1) Sectorized rotating (0.35 Hz) targets consisting of plates of pure (99.95% or better) metals (Zr, Cu); in this configuration the two metal species were sequentially deposited changing the kinetics of growth
- (2) Melt spun ribbons of BMGs of desired composition ( $Zr_{70}Cu_{30}$ )
- (3) Polycrystalline, single-phase, intermetallic tetragonal (*t*, C11b structure)  $Zr_2Cu$  targets produced by vacuum arc melting of pure (99.95% or better) metals (Zr,Cu).

The second harmonic ( $\lambda = 532$  nm) of a Nd: yttrium aluminium garnet laser (pulse energy 120 mJ, pulse duration 4 ns, repetition rate 10 Hz) in hard focusing has been used for the ablation at a working pressure of  $\sim 10^{-3}$  Pa. For the DCMS experiments two 2 in. equipotential, unbalanced DC magnetrons with pure (99.995%) Zr and Cu cathodes were employed, resulting in films with composition  $Zr_{60}Cu_{40}$ . The two magnetrons were placed at an angle of incidence of  $45^\circ$  with respect to the substrate normal. The substrates were electrically floating in order to minimize ion-solid interactions at the growing film surface. Films of pure Cu and Zr have been also grown by DCMS with identical conditions (working pressure = 0.8 Pa, target power) for comparison purposes.

The film and target compositions were measured by energy dispersive x-rays in a JEOL

scanning electron microscope. The microstructure of the films and the targets was evaluated by X-ray diffraction (XRD) in Bragg–Brentano geometry and transmission electron microscopy (TEM) techniques. Specimens for TEM and high-resolution TEM (HRTEM) in plan view and cross section geometries were prepared using mechanical thinning followed by ion beam milling up to electron transparency. TEM and HRTEM observations were performed using a JEOL 2011 transmission electron microscope.

Microstructure snapshots of the MD simulated TFMG systems in plan view and cross section geometries are presented in Fig. 24. The structural analysis of the equilibrium MD configurations yielded that the D1 process leads to purely amorphous film, with no short or medium range order (Figs. 24a and b). Interestingly, some of the D2 cases exhibit crystalline characteristics (Figs. 24c–f). The degree of the crystalline features in D2 deposition strongly depends on the composition of the films and the relative thickness of the individual Cu and Zr deposited layers. Thus, the cross section snapshots (Figs. 24d and f; D2b, i.e. Zr-rich case) reveal that the layering and the crystalline features are more pronounced; this effect is attributed to the fact that the interdiffusion of Cu into Zr layers is not sufficient to consume completely the Zr layer.

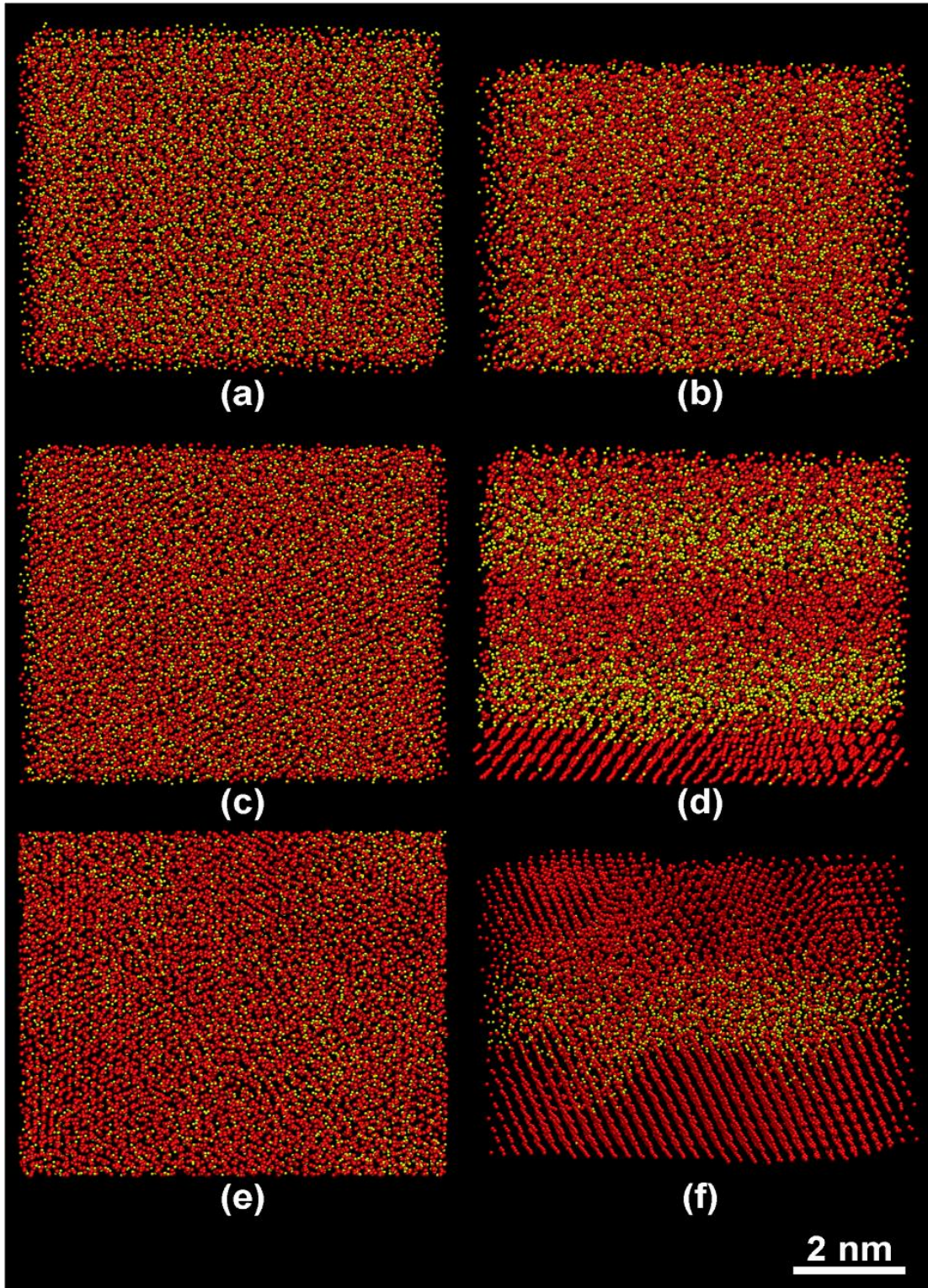


**Figure 24.** Results of MD-simulations of Zr–Cu growth  
 (Red and yellow spheres stand for Zr and Cu atoms, respectively)  
 a) D1 deposition  $\text{Cu}_{40}\text{Zr}_{60}$ , plan view; b) D1 deposition  $\text{Cu}_{40}\text{Zr}_{60}$ , cross section;  
 c) D2a deposition  $\text{Cu}_{40}\text{Zr}_{60}$ , plan view; d) D2a deposition  $\text{Cu}_{40}\text{Zr}_{60}$ , cross section;  
 e) D2b deposition  $\text{Cu}_{20}\text{Zr}_{80}$ , plan view; f) D2b deposition  $\text{Cu}_{20}\text{Zr}_{80}$ , cross section.

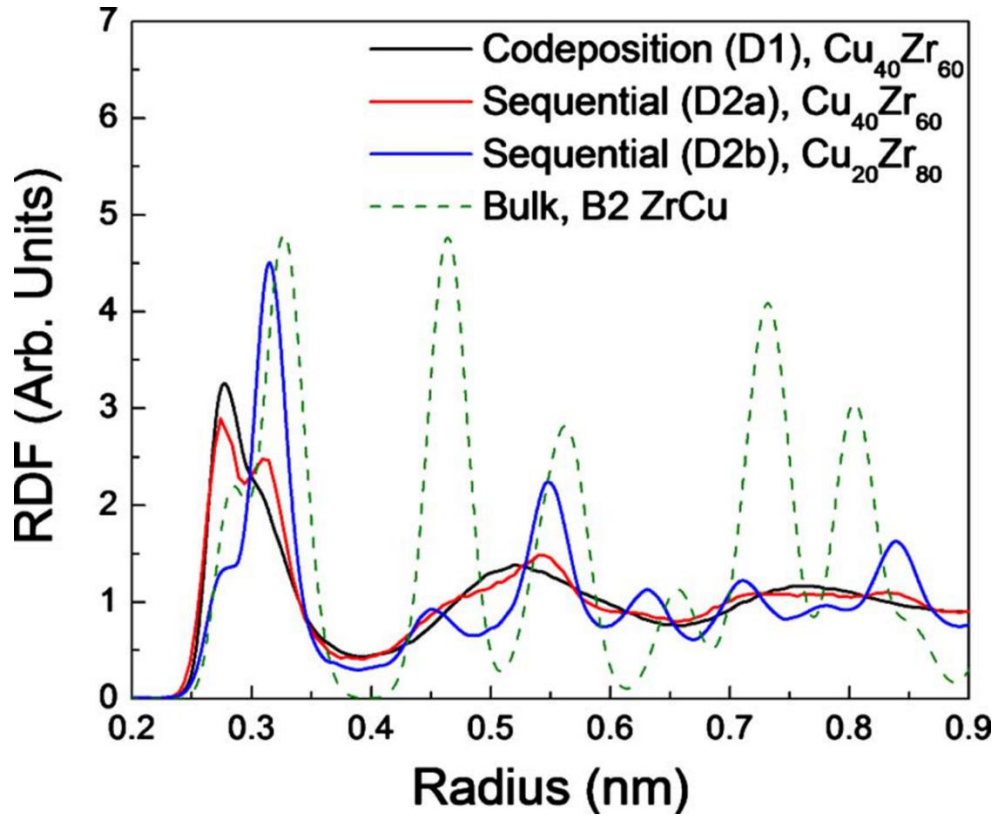


**Figure 25.** RDFs of the simulated depositions of Cu–Zr TFMG for co-deposition of Cu and Zr (D1) and sequential depositions (D2) of different Cu and Zr layers; the RDF of the crystalline ZrCu (B2 structure) is also shown for comparison

From the RDF (Fig. 25), it is clearly seen that the D2b overlayer exhibits the characteristics of the ZrCu crystalline structure (B2), Fig. 24f, while the complete absence of crystallinity is demonstrated in the D1 add-layer (Fig. 24a). The RDFs of the two D2 depositions are slightly shifted compared to the RDF of the single crystal B2 phase (Fig. 25, green dashed line). This is a very serious indication of the existence of growth stress, in agreement with the experimental observations. In addition, it can be seen that in both D2 cases layering occurs in the very first stages of the deposition (up to thickness of about 1 nm), an effect that is more pronounced in the D2b case.

In order to elucidate the origin of structural differences in the D1 and D2 processes, we performed detailed structural analysis to the corresponding equilibrium configurations, employing the method of CNA [116]. The CNA analysis revealed that in the case of the D1

deposition, the amorphous film consists of ICO clusters that may be distorted, truncated and/or interpenetrating (Fig. 26a) [117], while in the D2 case clear manifestation of the BCC B2 (which is very similar to the tetragonal C11b at atomic level) and HCP structures are indicated. In Figs. 26 we present the evolution of the basic CNA indices with the simulated film thickness for all films, in which it can be seen that the amorphous film D1 exhibits an increasing number of ICO clusters that reaches a plateau value around 13%, in agreement with the value of the Cu–Zr BMG case [119,120] (the reported number of clusters corresponds to perfect undistorted clusters, and therefore, the real total number of clusters is much higher). The D2 films demonstrate the coexistence of the B2 and HCP structures that correspond to nanocrystalline  $Zr_2Cu$  and Zr, respectively. It is worth pointing out that the existence of ICO clusters in the interfacial areas of the D2b films demonstrates the role of the diffusion mechanism in forming the amorphous phase.

Moreover, simulations with different plasma temperatures (from RT to 12000 K) and compositions (30% and 40% content in Cu) yielded similar results, indicating that the creation of glassy films does not depend on the plasma conditions and it is mainly due to the formation of the ICO clusters that play the role of nucleation barrier, thus impeding the crystallization processes.

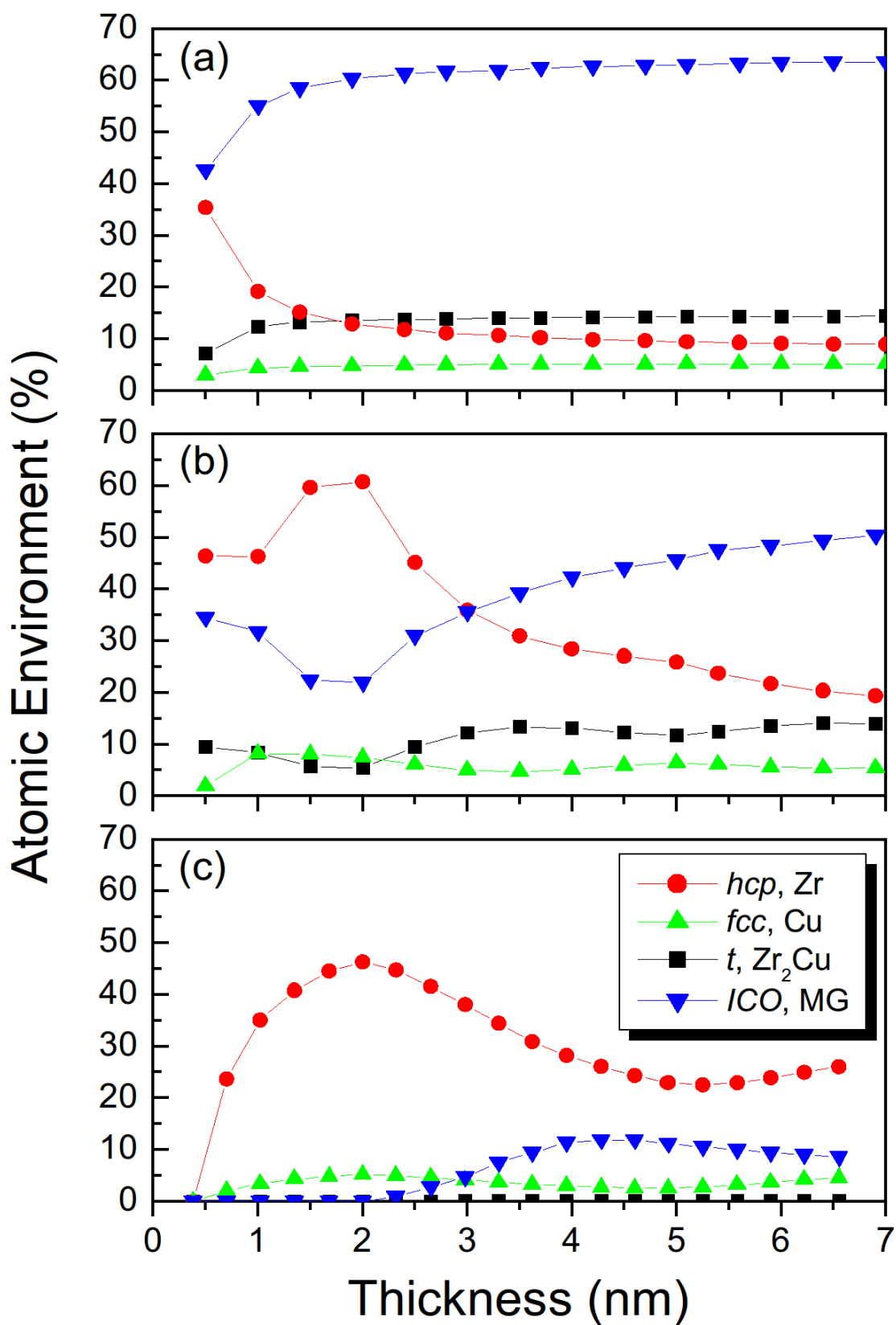


**Figure 26.** The evolution of the atomic environment of the deposited atoms during the simulated Cu-Zr deposition based on the CNA analysis. [128]  
 a) D1 deposition, Cu<sub>40</sub>Zr<sub>60</sub>; b) D2a deposition, Cu<sub>40</sub>Zr<sub>60</sub>; c) D2b deposition, Cu<sub>20</sub>Zr<sub>80</sub>

PLD has been used as a model film growth technique due to its well-known ability to produce films with homogeneous chemical composition of a multi-elemental target, like our case of Cu–Zr. In order to identify the possible effect of the target’s structure to the structure of the produced Zr–Cu films, we used three types of targets:

- (1)  $Zr_{70}Cu_{30}$  BMG
- (2) Polycrystalline intermetallic ( $t$ - $Zr_2Cu$ )
- (3) Sectored target consisting of plates of pure Zr and Cu.

The plan view HRTEM in Fig. 27a illustrates the amorphous structure of the BMG target. The Zr–Cu films grown from the  $Zr_{70}Cu_{30}$  BMG ribbon are purely glassy and resemble the BMG target, as revealed in the plan view HRTEM image shown as inset in Fig. 27a. The structure of the thin film is identical to the BMG target. The pure glassy state has been also confirmed with selected area electron diffraction (SAED), as shown in the upper right side inset of Fig. 27a. Cross section HRTEM images (Fig. 27b) have clearly demonstrated a perfect glassy structure in the films grown by PLD from a  $t$ - $Zr_2Cu$  polycrystalline target. The structural difference between the glassy film and the crystalline Si is evident. The comparison of the films grown by the two different targets demonstrates that the structure of the target does not influence the structure of the films grown by the PLD technique as long as the Zr and Cu species are ablated simultaneously. Consequently, the experimental evidence supports the MD predictions that the film structure is determined by the diffusion of arriving species on the film surface. In both cases the composition of the target has been retained in the produced films ( $Zr_{70}Cu_{30}$  and  $t$ - $Zr_2Cu$ , respectively), which are in the usual composition range for glassy Zr–Cu [125], and lies within the range of compositions used for the MD simulations in this work.

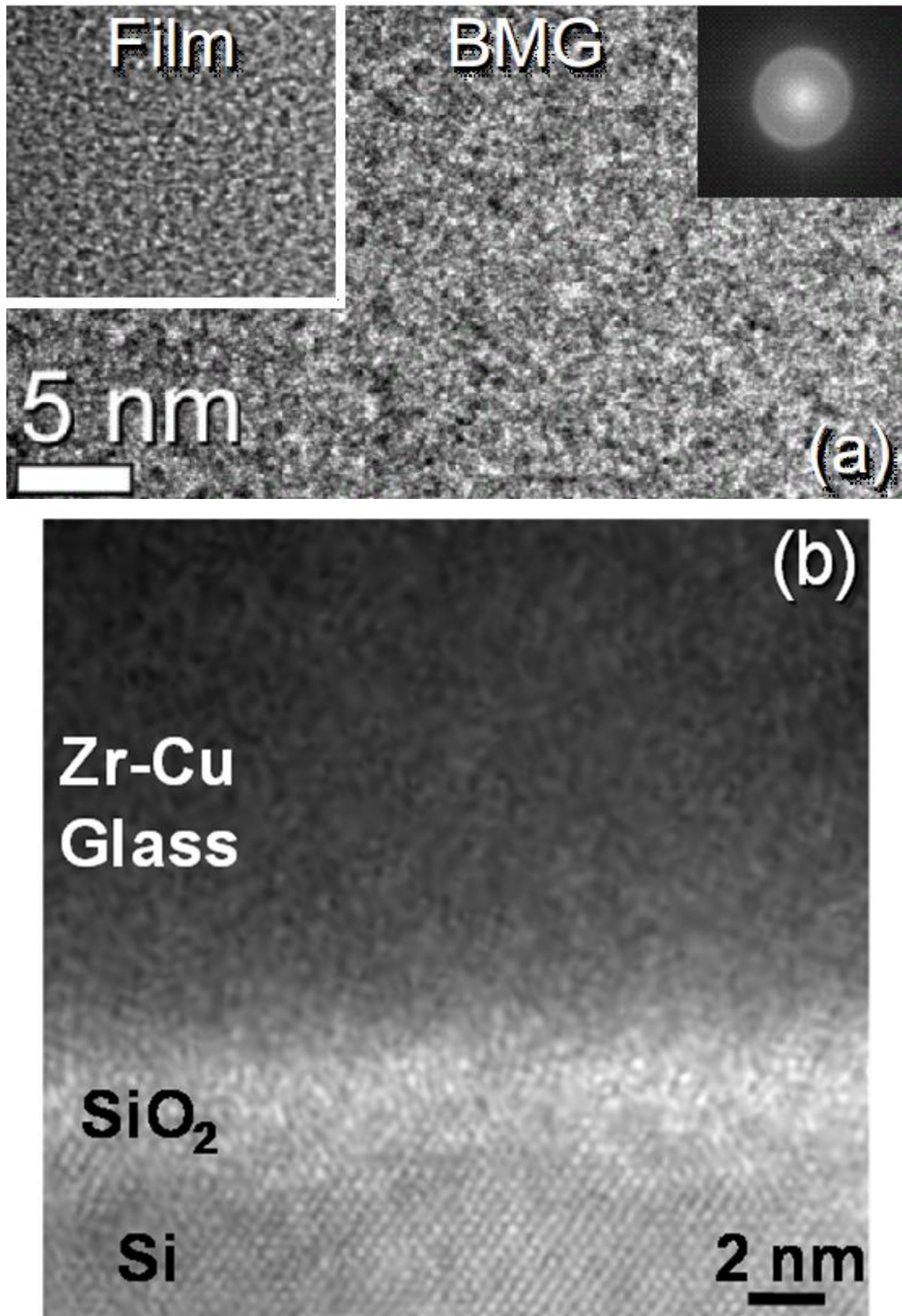


**Figure 27.** a) Plan view HRTEM image showing the amorphous structure of the BMG target. The pure glassy state of the Zr–Cu films grown from the BMG ribbon is depicted in plain view HRTEM image and the corresponding SAED are shown in the insets; the same scale bar applies to both images. b) Cross-section HRTEM image from a Zr–Cu glass film grown from a t-Zr<sub>2</sub>Cu target. [128]

In order to investigate the effects of the adatoms' mobility and surface diffusion we also performed PLD experiments using the rotating, sectored Zr–Cu target. In that case the grown films were not glassy; instead, they exhibited a nanocrystalline structure as shown in the HRTEM plan view image of Fig. 28. The film consists of nanograins of the stable  $t$ -Zr<sub>2</sub>Cu (Fig. 28 grain A), and hexagonal  $\alpha$ -Zr (Fig. 28 grain B) embedded in an amorphous matrix. No trace of Cu grains was detected over the whole studied area.

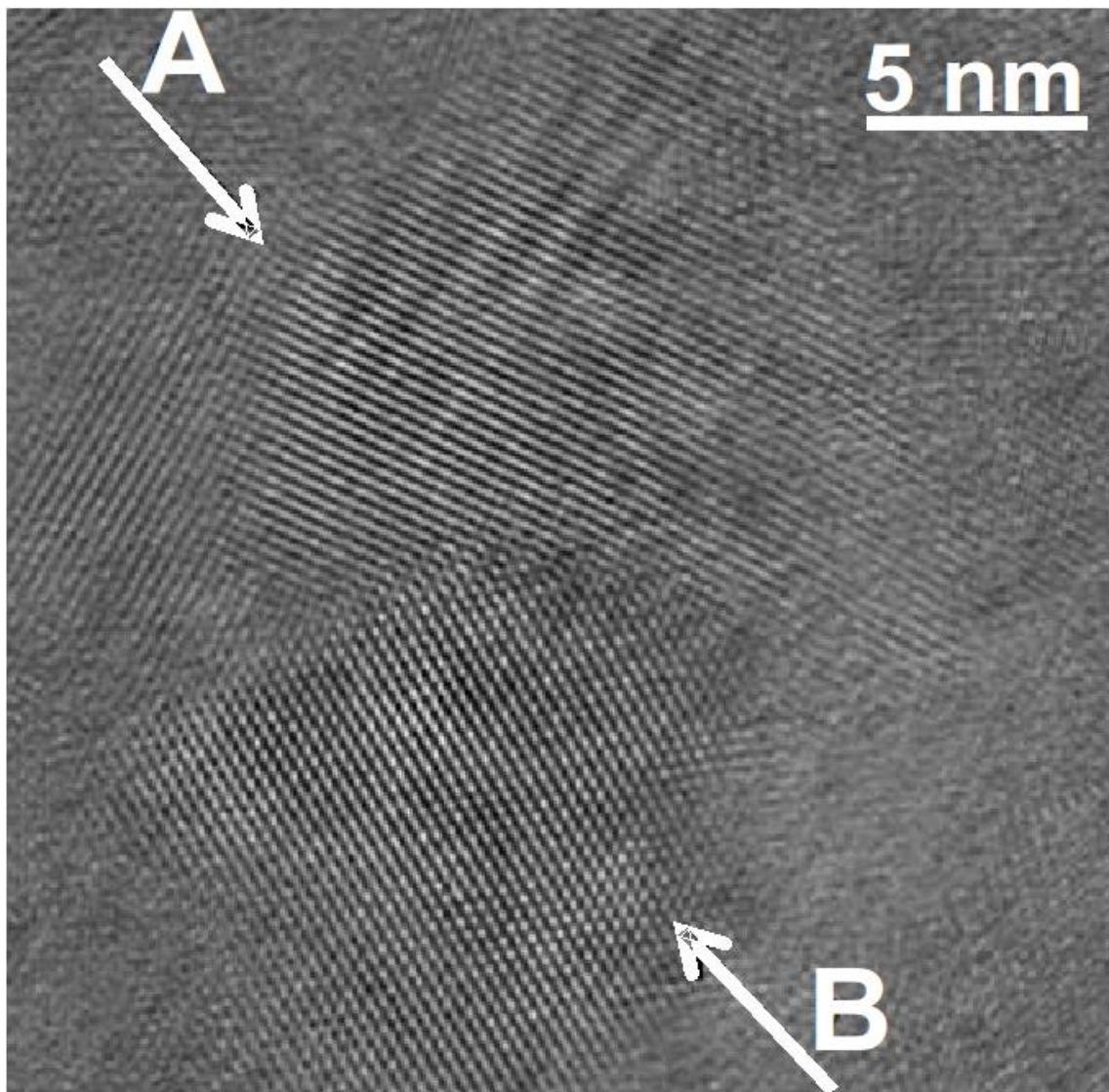


**Figure 28.** The nanocrystalline structure of a Zr–Cu film grown using a target consisting of Zr and Cu plates (sequential deposition). [128]  
region A: a tetragonal C11b Zr<sub>2</sub>Cu(101) grain; region B: a hexagonal  $\alpha$ -Zr(100) nanograin

This confirms experimentally our MD simulations as well as recent predictions based again on MD [129]. Accordingly, in the case of Cu deposition on a Zr-Cu glass surface, the resulting ad-layer is mixed, exhibiting partial layering and structuring that occurs at the expense of Zr atoms in the BMG. When Zr atoms are deposited on the same BMG surface, the mixing is restricted close to the interface area, while pure Zr ad-layers crystallize in the energetically favoured (111) face. Amazingly this effect occurs well below the glass transition temperature and it can be observed even at RT, demonstrating clearly that the surface diffusion of adatoms is significant even at RT, in agreement to our MD simulation findings. The corresponding experimental results (Fig. 28), are in very good agreement with the MD predictions (Figs. 24). By combining experimental and MD results it is clearly shown that the surface diffusion during growth is not sufficient for the adatoms to migrate into the bulk (the maximum interfacial layer observed in MD is of the order of a few ML) and therefore, when the thickness of the individual Cu layer exceeds this limit, crystalline residuals are observed (Fig. 24c), such layering has been also observed in sequential sputter deposition experiments [130]. Otherwise, when a pure mixture occurs (i.e., the individual layers are very thin) the film consists of a mixture of amorphous,  $\alpha$ -Zr and  $t$ -Zr<sub>2</sub>Cu phases as revealed by both MD (Fig. 24b) and HRTEM (Fig. 28).

We should also point out that the self-organization of the Zr and Cu adatoms observed in the experiment takes place for immensely high real deposition rates. Although the apparent deposition rate for PLD is very low (compared to other PVD techniques, such as sputtering) and in our case is of the order of 6 nm/min, the real deposition rate is order of magnitudes higher due to the pulsed character of the deposition. Thus, the deposition takes place in a time interval that is comparable to the pulse duration (4 ns), followed by a dead time which is 100 ms for the 10 Hz repetition rate. Consequently, the real deposition rate during the laser pulse is  $10^{-2}$  nm/ pulse, which is equivalent to  $3 \times 10^6$  nm/s and it is much

higher than any other PVD technique. Assuming a gas to solid phase transition that takes place in few nanoseconds, the equivalent cooling rate is immensely higher than in BMG growth cases; the self-organization of Zr and Zr<sub>2</sub>Cu is, therefore, of special importance since from the thermodynamic point of view a glassy phase would be favoured. This is even more important if we compare their structure with that of glassy films grown by simultaneous Zr and Cu deposition (Figs. 27) with the same growth rate.

**Table 10** – [128]

Comparison of the main kinetic and thermodynamic parameters for the formation of Zr–Cu glass in PLD, sputtering, and bulk casting

	<b>PLD</b>	<b>Sputtering</b>	<b>Bulk casting</b>
Kinetic energy of species (eV)	~ 100	~ 5	-0.15
Pressure (mbar)	$1 \times 10^{-5}$	$7.5 \times 10^{-3}$	1013
Real deposition rate (nm/s)	$3 \times 10^6$	4	...
Substrate-target distance/Mean free path ratio <sup>a</sup>	$5 \times 10^{-3}$	5	...

<sup>a</sup>Equivalent to the mean number of collisions per atom occurring in gas phase between sputtering/ablation and deposition

The sputter deposition is a process in which the deposition rate, the working pressure, and the kinetic energy of the deposited atoms are immensely different than in PLD and in bulk casting, as summarized in Table 10. This has severe consequences to the kinetics (growth rate), thermodynamics (pressure), and energetics (kinetic energy of add-atoms) of growth. In addition, the co-sputtering from two individual metal targets ensures that the mixing of species takes place on the film surface and not in the gas phase (as it would happen for PLD [131]). The assumed scenario of glass formation driven by a stochastic mixing can be confirmed by studying the sputter deposition of Zr–Cu. A similar behaviour in PLD and sputtering would imply the elimination of all the other possible mechanisms and growth parameters (growth rate, pressure and energetics) to the glass formation. Indeed, co-depositing Cu and Zr from two individual magnetron sources, with the minimum sputtering power density ( $0.5 \text{ W/cm}^2$ , target voltage = 250 V) which stabilizes the plasma, resulted in

Zr<sub>60</sub>Cu<sub>40</sub> films exhibiting XRD patterns characteristic of pure glass (Fig. 29a) with a broad peak due to first neighbour distance located at  $d = 0.255$  nm; this  $d$  value is characteristic of the Zr–Cu bonds in an ICO cluster [125]. Similar glassy structure has been observed

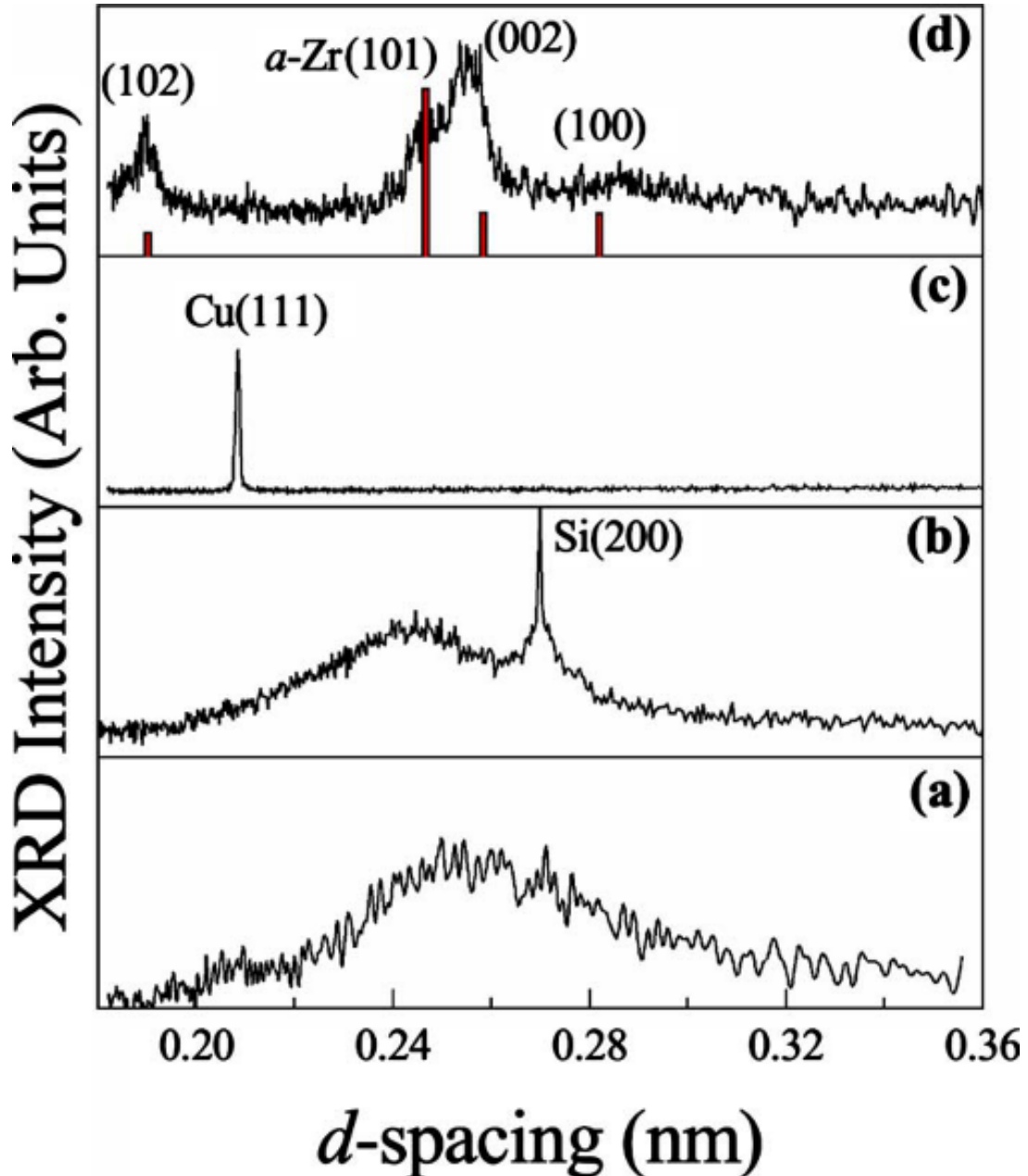


**Figure 29.** XRD patterns from sputtered Zr–Cu films grown using (a) 0.5 W/cm<sup>2</sup> and (b) 4 W/cm<sup>2</sup>. Pure Cu (c) and Zr (d) films grown with identical conditions with Zr–Cu are displayed for comparison. [128]  
The vertical bars indicate the powder diffraction pattern for  $\alpha$ -Zr [134]

for higher sputtering power densities up to 4 W/cm<sup>2</sup> (e.g., see Fig. 29b, the Si(200) XRD

peak from the substrate has been also observed [132]), the only difference is a shift of the XRD peak to 0.245 nm, which is attributed to stress induced by the deposition of highly energetic species [133] and it is also consistent with the presence of distorted ICO-like clusters [127].

The stochastic character of the glass formation is supported by the structure of sputtered films of pure Cu and pure Zr grown using identical power density ( $4 \text{ W/cm}^2$ ) and working pressure with the  $\text{Zr}_{60}\text{Cu}_{40}$  case. The Cu and Zr films are clearly polycrystalline and textured along the Cu(111) and Zr(002) [134] orientations, which are the closest-packing orientations of the FCC and the hexagonal crystals, respectively. This observation clearly indicates that no thermodynamic or energetic mechanism is responsible for the glass formation for the given deposition rate and substrate temperature in sputter growth, since Zr, Cu, and  $\text{Zr}_{60}\text{Cu}_{40}$  growths have taken place in almost identical conditions.

#### ***4.4 MICROSTRUCTURAL DIFFERENCES OF AMORPHOUS $\text{Cu}_{65}\text{Zr}_{35}$ BETWEEN RAPIDLY QUENCHED AND TOPOLOGICALLY DESTABILIZED CRYSTALLINE Cu AND Zr METALS***

Following the previous intriguing result, we focused our next step in revealing the origin of the structural differences between two different amorphization routes; we compare quenched produced  $\text{Cu}_{65}\text{Zr}_{35}$  BMG with BMGs produced by mechanical alloying. We focused on the topological instability of the original Cu or Zr lattices induced by pure straining caused by incrementally added substitutional atoms, thus following the approach proposed by Egami and Waseda for the topological destabilization of a crystalline lattice [123]. Considering that the main mechanism acting upon mechanical alloying is related to the gradual elemental substitution in a host lattice, the  $\text{Cu}_{65}\text{Zr}_{35}$  MGs were prepared by successive substitutions of Cu by Zr atoms in an FCC lattice, or Zr by Cu atoms in a HCP

lattice, followed by sufficient relaxation (i.e. zero pressure, temperature and energy stabilization) at 300K and we compare them with the quenched  $\text{Cu}_{65}\text{Zr}_{35}$  EAM simulated system, (called S and Q systems hereafter). For the S- $\text{Cu}_{65}\text{Zr}_{35}$  system the following procedure was applied for both FCC-Cu and HCP-Zr lattices containing 16,000 atoms each.

a) The perfect crystalline lattice was equilibrated at 300K in the canonical isothermal-isobaric (NPT), followed subsequently by an equilibration in the microcanonical ensemble (NVE). b) In this system we incrementally substituted at steps of 2 at % the original lattice positions by the substitutional atoms. After each substitution, we applied the previously described equilibration procedure at 300K until the final chemical composition  $\text{Cu}_{65}\text{Zr}_{35}$  was reached.

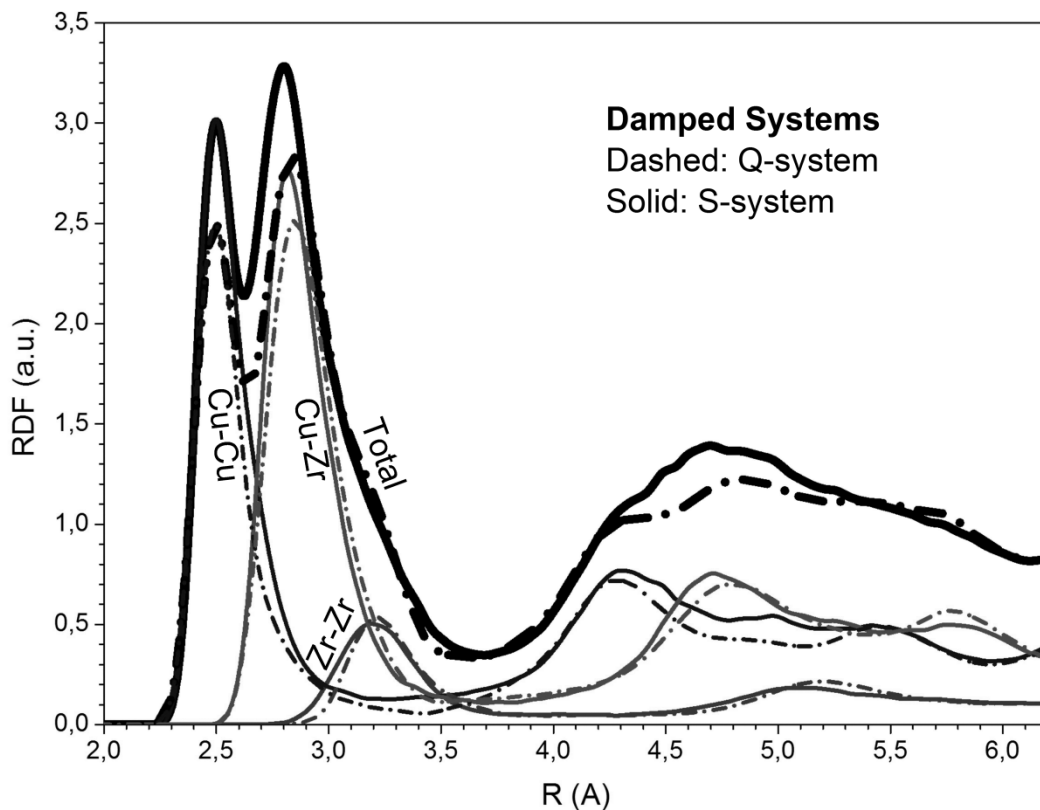


**Figure 30.** Radial Distribution Functions of the as-quenched (Q-system)  $\text{Cu}_{65}\text{Zr}_{35}$  amorphous alloy (dashed lines) and the amorphous system produced by topological destabilization (S-system) of the crystalline Cu or Zr (solid lines). [135]

In Fig. 30 we present the RDFs of Q and S systems (dashed and solid lines respectively) after relaxation at 300K. We can see that there are small differences, basically in the Cu-Zr and Zr-Zr bonds, which become more significant in the region of the second peak, with the Q system exhibiting some splitting, thus indicating some “ordering” at these distances, contrary to the S case that appears less “ordered”. It is also interesting to notice that exactly the same RDF was found for the S systems produced from FCC-Cu or HCP-Zr pure lattices, i.e. the same amorphous structure was obtained from the topological destabilization of both systems by means of the incremental addition of substitutional atoms, Fig. 31.

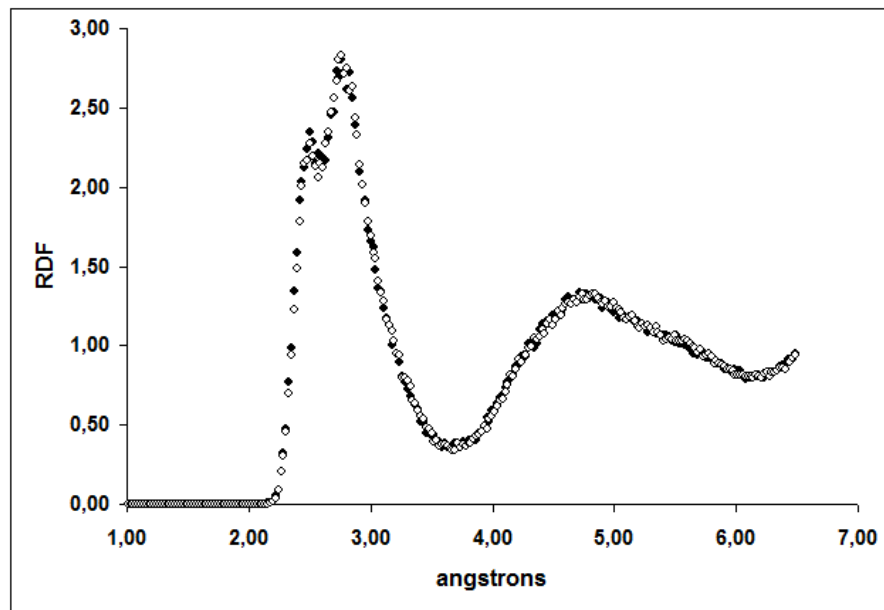


**Figure 31.** Radial Distribution Functions (RDF) of the amorphous  $\text{Cu}_{65}\text{Zr}_{35}$  alloy produced by the topological destabilization of the FCC-Cu lattice (filled symbols) and HCP-Zr lattice (open symbols). [135]

These structural differences between Q and S systems could be attributed to incomplete relaxation of the S system (due to the limited diffusion at 300K). Indeed, upon annealing of both systems at 800K for 1ns their RDFs came much closer, Fig. 32. We have to notice here

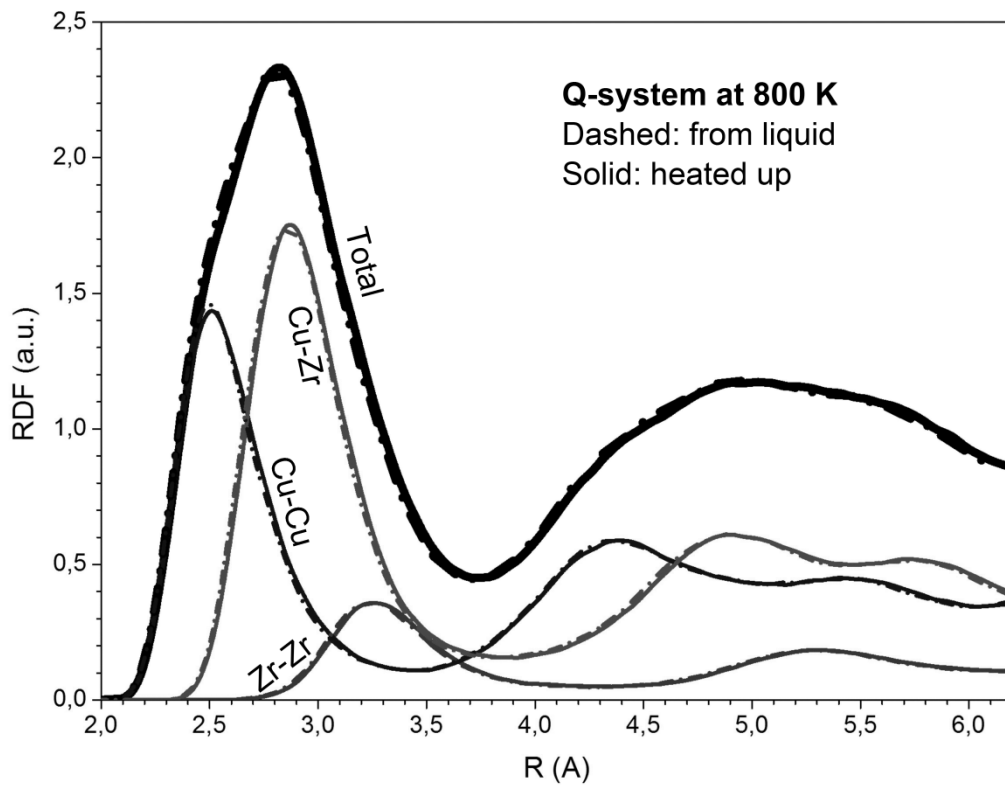
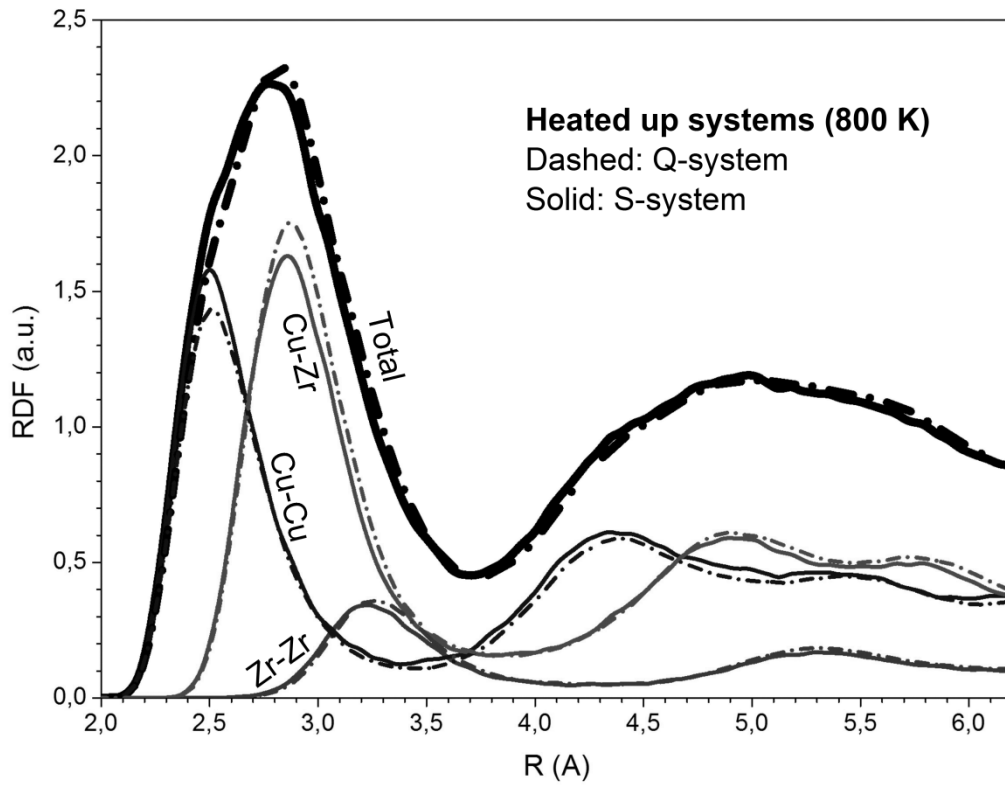


**Figure 32.** Radial Distribution Functions of (upper): annealed samples produced by rapid quenching (Q-system) and topological destabilization of the crystalline lattice (S-system) and (lower): no significant difference between the annealed and as-quenched conditions for Q-system. [135]

that crystallization cannot occur within the time scale of a usual MD simulation since an impractical large number of time steps would be necessary. Interestingly, the Q system does not exhibit any significant structural difference between the original quenched and the annealed system at 800 K, Fig. 32, denoting that the relaxation was completed in the super-cooled region within the simulation time.

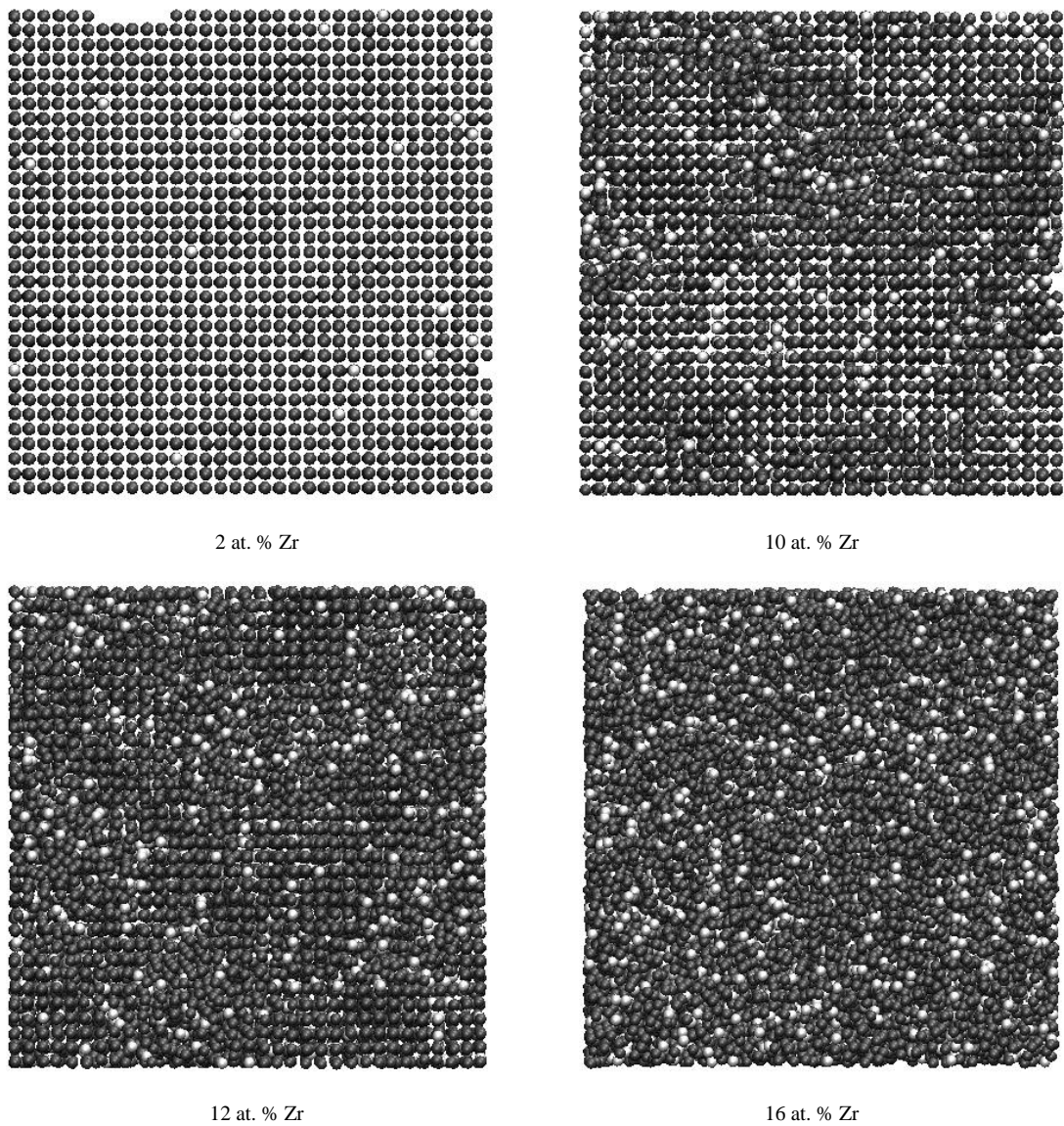


**Figure 33.** (100) crystalline plane view of FCC-Cu as a function of different Zr solute concentrations (white atoms). [135]

The amorphization of the crystalline structure in the S systems, promoted by the

systematic addition of solute atoms, starts with isolated islands of amorphous structure embedded in the crystalline matrix as shown in Fig. 33. As the local strains increase in volume and intensity, Fig. 34, those amorphous islands percolates and the entire crystalline structure collapses. This behaviour was observed for both S cases, solute Cu in HCP-Zr matrix as well as solute Zr in FCC-Cu, resulting in final alloys with exactly the same structure as shown in Fig 31.

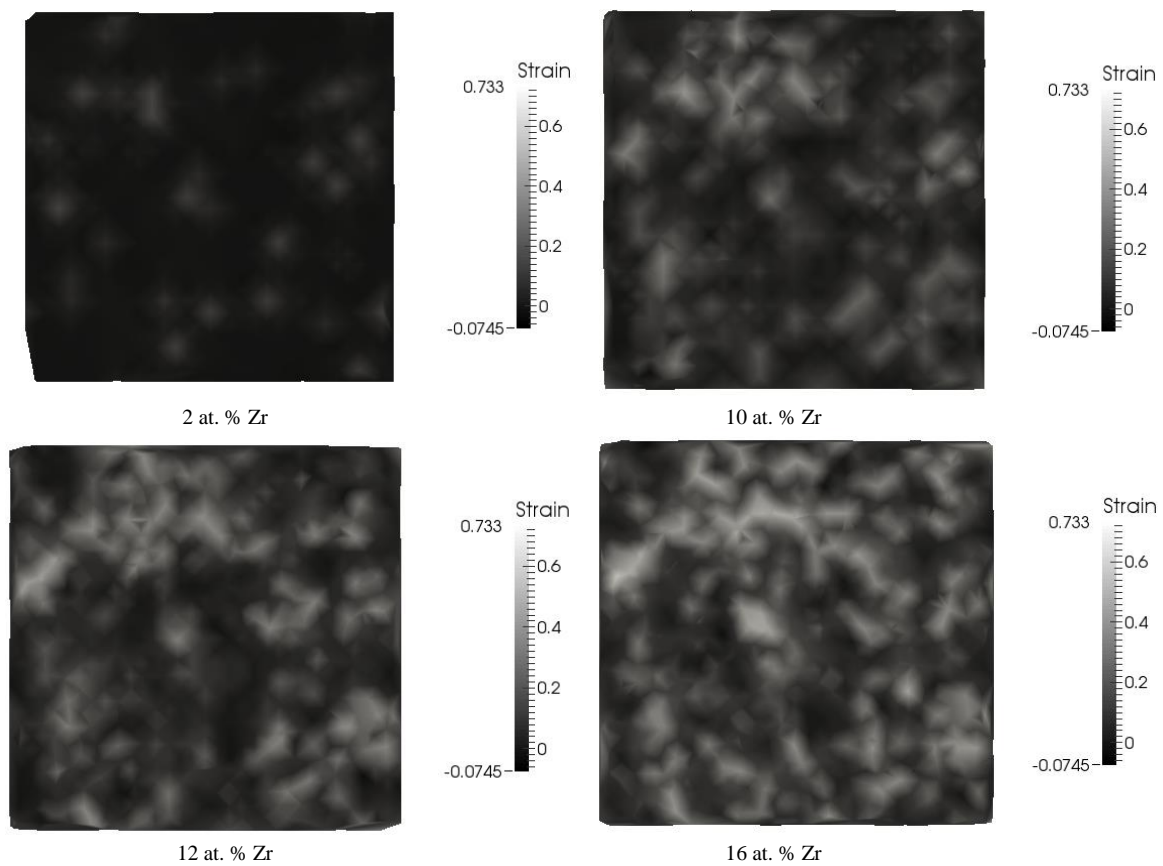


**Figure 34.** (100) crystalline plane view of FCC-Cu as a function of different Zr solute concentrations (white atoms). [135]

Aiming in obtaining insight of the structural details we performed detailed cluster analysis that revealed that the S system contains less clusters, Table 11, basically ICO clusters, than the Q system (rows Q1 and S1) and that these differences become smaller after annealing (rows Q2 and S2). More details about the clusters present in the systems and their

evolution upon annealing are given in Table 12. It is clear that the “ordering” is due to the formation of more clusters, mainly ICO, which in turn is driven by the chemical affinity of the atomic pairs. It turns out, therefore, that the amorphization is basically depending on the topological instability of the crystalline phases and the chemical ordering acts against amorphization but, at the same time, helps in stabilizing the amorphous state.

**Table 11** – [135]  
Main clusters found in the samples

Systems		Clusters			
		All	ICO	Cub	RhD
Q.1	Quenched	53.8	31.4	9.2	11.7
Q.2	Annealed	52.2 ±1.2	29.7 ±0.7	9.2 ±0.1	11.7 ±0.4
S.1	Alloyed	47.6	27.6	8.6	10.3
S.2	Annealed	52.5 ±0.3	28.9 ±0.3	9.9 ±0.2	12.3 ±0.2

**Table 12** – [135]  
Detailed description of clusters found in the samples

Systems			Clusters			
			All	ICO	Cub	RhD
Perfect Clusters	Q.1	Quenched	2.1	2.1	0.0	0.0
	Q.2	Annealed	1.9 ±0.3	1.9 ±0.3	0.0	0.0
	S.1	Alloyed	2.0	2.0	0.0	0.0
	S.2	Annealed	1.7 ±0.1	1.6 ±0.10	0.010 ±0.005	0.0
Well-Shaped Clusters	Q.1	Quenched	22.0	18.0	2.5	1.4
	Q.2	Annealed	19.9 ±0.1	16.2 ±0.1	2.32 ±0.04	1.28 ±0.03
	S.1	Alloyed	19.2	15.4	2.4	1.3
	S.2	Annealed	19.4 ±0.2	15.5 ±0.2	2.51 ±0.11	1.37 ±0.06
Distorted-Truncated Clusters	Q.1	Quenched	29.7	11.4	6.7	10.3
	Q.2	Annealed	30.4 ±0.1	11.42 ±0.08	6.97 ±0.07	10.5 ±0.1
	S.1	Alloyed	26.4	10.2	6.2	9.1
	S.2	Annealed	31.4 ±0.3	11.76 ±0.17	7.40 ±0.13	10.9 ±0.2

The chemical affinity between Zr and Cu however, leads to a complicated path towards crystallization. If we had a positive heat of mixing between Cu and Zr the chemical ordering of Cu-Cu and Zr-Zr pairs would rapidly evolve to the simple and segregated lattices of Zr and Cu metals. This finding is in good agreement with the basic empirical rules of glass formation, i.e. atomic size mismatch and negative heat of mixing between the main elements of the alloy [22,136,137]. It is also interesting to notice that the results of the present work

are in good agreement with experimental results for rapidly quenched samples by means of a large difference of cooling rates. By applying a technique of ultra-rapid quenching on the  $Zr_{55}Cu_{30}Ni_5Al_{10}$  alloy, with a cooling rate of 1010 K/s, Liu and co-workers [138] observed that the glass thus produced shows a less ordered structure, especially around Zr atoms, i.e. more ordered Zr-clusters were found in the glassy samples produced by lower cooling rates. Furthermore the ultra-rapidly quenched glass evolves to a more ordered structure, more Zr-centred clusters, more Zr-Cu pairs and less Zr-Zr pairs, after relaxation.

#### ***4.5 ANALYSIS ON THE MICRO-STRUCTURE OF $Cu_x-Zr_{(100-x)}$ , $x=65,35$***

Up to now we have seen that Cu-Zr metallic glasses are consisted of a significant percentage of tiny ICO clusters that increase in number upon solidification and/or Cu enrichment and that their composition is correlated with the system's stoichiometry. Moreover, their bonding nature is a key factor for their stability making them very important to form the resultant microstructure of the system. Even though, looking back in Fig. 17 we can clearly see that even if we consider the clusters as non-interacting with each other, even at the Cu-rich cases more than the half atoms of the system are not included to the perfect icosahedral clusters. Moreover, taking into account that the clusters are indeed interconnected, the percentage of the participating atoms of the systems into these clusters decreases to about 25%.

Very interestingly, similar structural characteristics are also present in the case of liquidus and undercooled simple metals like Al or Na, the micro-structure of which is found to be composed of tiny ICO-like clusters that are interconnected forming larger objects with total number of atoms that obey certain sequences of magic numbers [139,140]. The existence of ICO-like clusters in these liquids has also been verified experimentally, while

their stability has been proved theoretically by means of density functional theory computations that additionally yielded the possibility of the existence of so-called poly-icosahedral clusters [141,142]. However, the size of these clusters is limited to just a few atoms mostly because they are subjected to important stresses that become significant at larger sizes and eventually prohibit their increase [141,143]. Additionally, it is accepted that in the case of binary systems in which the two elements have significantly different atomic sizes, the resulting ICO-like clusters, although distorted, become more stable even from their single element perfect-shaped counterparts because of the release of the internal stresses [141]. Indeed, in many studies the existence of ICO-like clusters in undercooled liquids and metallic glasses (MGs) has been established and considered as an explanation for their basic properties [140,144,145–147]. Recently, the presence of a self-similar assembly of clusters was concluded, with a fractal nature in the medium range order of MGs [147,148]. However, the way these clusters are interconnected had still remained unclear.

Aiming in revealing the driving force of these interconnections between the various types of clusters and in order to understand their role in the formation of the MGs, we considered more types of ICO-like clusters. We found, in agreement with previous studies [120,126,127,149], that the systems are basically composed of various ICO-like clusters that may be distorted and/or truncated. In details, similarly to the TBSMA simulated system, we confirmed for the EAM simulated  $\text{Cu}_{65}\text{Zr}_{35}$  case that about 25% of the system atoms are Cu-centres of 13-atom ICO clusters with composition of  $\text{Cu}_8\text{Zr}_5$  and furthermore, we discovered that about 40% of the system atoms are Zr-centres of 15-atom Rhombic Dodecahedra (RD)  $\text{Cu}_9\text{Zr}_6$  clusters. Moreover, we found out that the conjugate stoichiometry systems yielded practically the reversed compositions, i.e.  $\text{Cu}_5\text{Zr}_8$  and  $\text{Cu}_6\text{Zr}_9$ . The intriguing issue is related to the multitude of ways in which their interconnections could be envisaged. This is a very complex situation, considering all the possible combinations of ICO with RD clusters which

are concurrently present in the systems. A number of studies have explored combinations of the possible interconnections of clusters and suggested specific sequences or magic numbers for the resulting “SuperClusters” (SC), basically depending on the type of cluster considered [141,144,145–147,150,151]. However, in reality the MGs are composed by combinations mostly of truncated and distorted interconnected clusters of various types, thus rendering this type of analysis inefficient.

In order to include all the possible combinations between the clusters we adopted another simple but more efficient approach that is not restricted from the type or the quality of a cluster. Given that MGs are homogeneous systems, one would expect that if there was a basic building unit its composition should correspond to the system’s stoichiometry. Therefore, starting from the observation that in almost all cases the compositions of ICO and RD clusters do not match the system’s stoichiometry, interconnections between the clusters are necessary for the formation of SCs whose composition will correspond to that of the system, basically by sharing common atoms. Accordingly,  $n$  interpenetrating  $\text{Cu}_y\text{Zr}_{(m-y)}$  clusters in a  $\text{Cu}_x\text{Zr}_{(100-x)}$  MG, where  $y$  is the averaged composition of Cu atoms and  $m$  is the average number of the atoms in these clusters, the total number of atoms in the SC will be [127]:

$$N_{SC} = [n \cdot y - C_{Cu}] + [n \cdot (m - y) - C_{Zr}] \quad (25)$$

where,  $C_{Cu}$  and  $C_{Zr}$  stand for the numbers of common Cu and Zr atoms amongst the clusters in the SC that have to be positive integers. These can be determined from the following Diophantine equation [127]:

$$C_{Cu} = n \cdot y - \frac{x}{100 - x} [n \cdot (m - y) - C_{Zr}] \quad (26)$$

For example, in the  $\text{Cu}_{65}\text{Zr}_{35}$  case,  $x = 65$  and, considering the very simple case of two ICO clusters,  $n = 2$ ,  $m = 13$  and  $y = 8$ . The  $C_{Zr}$  can have the values of 2, 3, 4 or 5, yielding SCs

consisted of 23, 20, 17 and 14 atoms, respectively. Note that when we use the nearest integer part of Eq. (26) the  $C_{Zr} = 0,1$  are irrelevant (negative  $C_{Cu}$ ), while the sequence is limited to  $C_{Zr} = 5$  (14-atom SC), the next one corresponding to two overlapping ICO clusters. Of course, this scheme holds for any type of clusters (e.g. 15-atom ICO-like) and their combinations as well as in multi-element systems. In these cases, if  $i$  stands for the element type,  $x_i$  is its composition into the MG and  $y_i$  is its averaged composition into the  $n$  clusters forming the SC, then the above equations become:

$$N_{SC} = \sum_i (n \cdot y_i - C_i) \quad (25.a)$$

and

$$C_i = n \cdot y_i - \frac{x_i}{\sum_{j \neq i} x_j} \sum_{j \neq i} (n \cdot y_j - C_j) \quad (26.a)$$

where once more, the only necessary restrictions are  $C_i$ ,  $n$  and  $N_{SC}$  to be positive integer numbers.

The above considerations have the following very important consequences:

- (i) Given that the clusters' compositions are in fact imposed by the system's stoichiometry, the chemistry dictated by the electronic structure of the constituent elements is restricted to the formation of the tiny clusters that form the SCs; therefore, one would expect the same sequence of SCs in the system with the conjugate stoichiometry, i.e. in the  $Cu_{35}Zr_{65}$  case. Indeed, we verified the validity of Eq. (25) by seeking in the equilibrium configuration for interpenetrating ICO-like clusters that resulted in SCs satisfying the system's composition. The populations of the SCs found in both systems are practically identical, obeying the predicted sequence from Eq. (25) of magic numbers (Fig. 35). It is interesting to note that the 20-atom SCs are formed mainly from the interconnection of two 13-atom ICO clusters, the 23-atom SCs are basically from two interpenetrating

15-atom ICO-like clusters, while the 31-atom SCs are the results of either the interconnections of three 15-atom ICO clusters or of combinations of three or four 13- and 15-atom clusters, implying the preference of the clusters in sharing common atoms and amplifying the efficient packing model. We must note here that the systems are basically composed by rather small clusters and SCs, a result that is most probably related to the very high cooling rate imposed by the MD limitations.

(ii) Accepting the smallest resulting SCs as the basic structural units of the MGs, a consideration that is compatible with the efficient packing model [146,150], the various interpretations of cluster packing [147] and the fractal nature of the medium range order in MGs [148], it has also important implications regarding the interpretation of pair interactions and thereby the microstructure of the MGs. For instance, the shorter distance that is usually attributed to Cu–Cu pair interactions in the simplest case of a perfect shaped ICO cluster is no longer unique, as it can be originated either from Cu core–shell or shell–shell interactions that are not equivalent [141] and therefore it is split into two distinct contributions. Similar effects hold for the larger neighbour distances and the situation becomes even richer in atomic pairs when taking into account the SCs that introduce additional interactions. Moreover, the fact that the clusters are binary, with one of their elements being significantly larger (Zr) than the other (Cu), results in important distortions of the clusters, thus altering the corresponding interatomic distances even more. Consequently, several pair contributions are to be expected at different distances, depending on the type of the clusters that form the SCs, justifying not only the existence of first and second neighbourhoods but also their inherent broadening in metallic glasses.

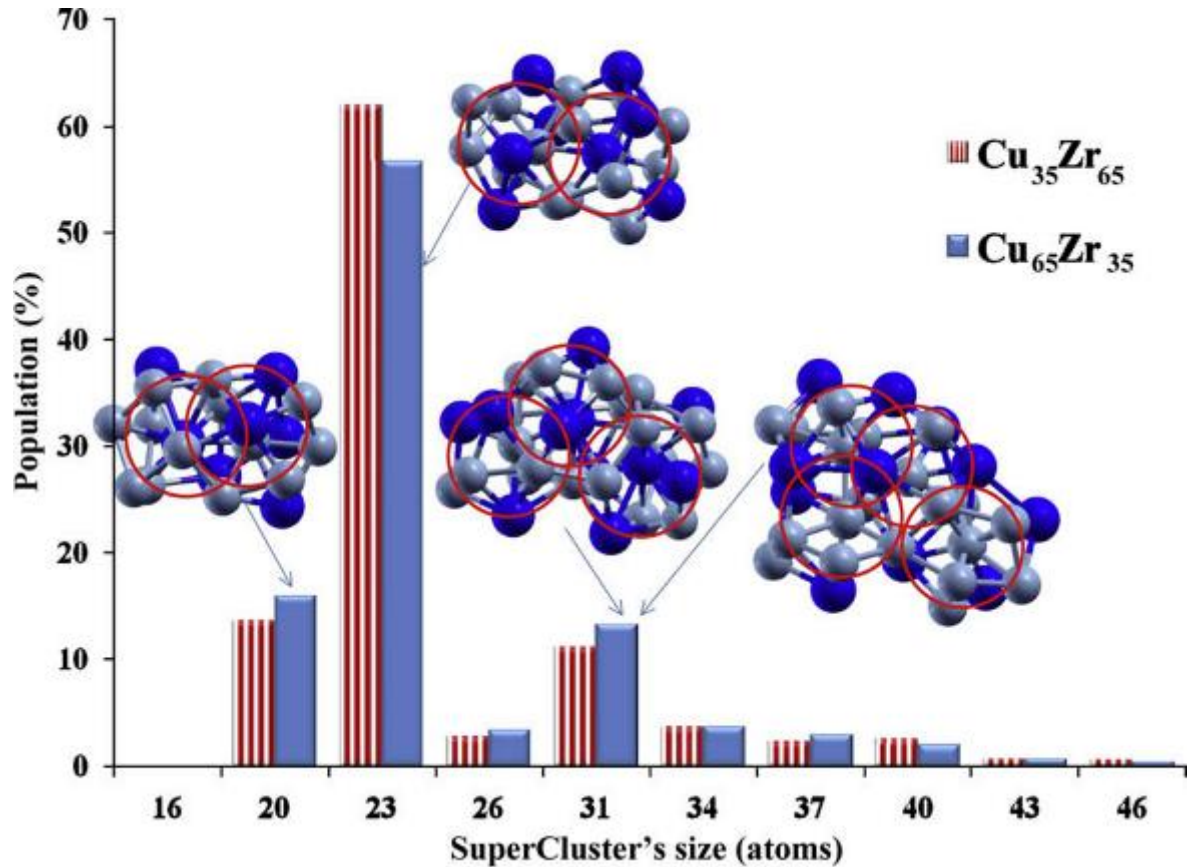


**Figure 35.** Populations of SuperClusters for two different compositions; also shown schematically are the most abundant SCs [127]

In Fig. 36 we give some calculated representative average partial RDFs of the three most abundant SCs, namely the 20 (Zr–Zr pairs, green line), 23 (Cu–Cu pairs, blue line) and 31-atom (Cu–Zr pairs, red line), along with an experimental one (black line), which were obtained from the high-energy synchrotron X-ray diffraction data of rapidly quenched melt spun  $\text{Cu}_{65}\text{Zr}_{35}$  ribbons (for details, see Ref. 23). The corresponding contributions of the 26-atom SCs are omitted for clarity and because of their insignificant participation.

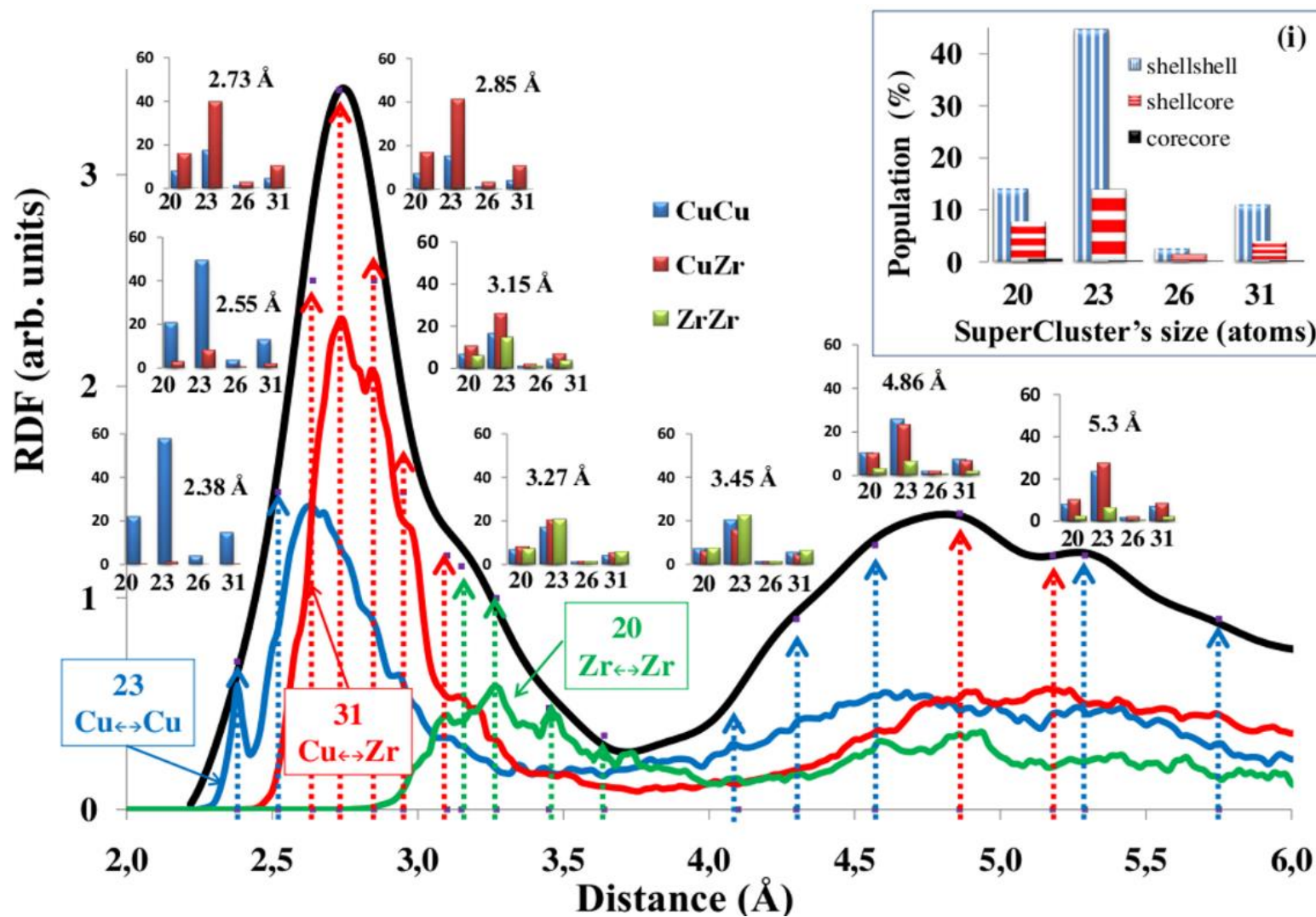


**Figure 36.** Selective partial RDFs for the 20-, 23- and 31-atom SuperClusters (corresponding to Zr-Zr, Cu-Cu and Cu-Zr pairs, respectively), along with an experimental one. In the consecutive insets the histograms concerning the type of the pairs as well as the populations of the SCs are given. Inset (i) depicts the participations in bonds of the various pairs according to their geometrical arrangement, i.e. core-core (black bar), core-shell (horizontally shadowed bar) and shell-shell (vertically shadowed bar). Coloured dashed arrows showing specific experimental peaks denote the origin of the responsible SC's pairs. [127]

Starting from the shortest possible bonds, the Cu–Cu pair interactions of the 23-atom SCs yield a clear peak at 0.238 nm, which is well below the lowest possible Goldschmidt bond length of the Cu–Cu pair, 0.256 nm, which is also present in this RDF at 0.255 nm. The highest contribution of these pairs appears at 0.264 nm, while it is important to note the significant participation of these interactions in the region around 0.315 nm, which is traditionally treated as exclusively due to Zr–Zr pair interactions. Substantial participation at this region is also due to the Cu–Zr cross interactions, which are basically responsible for the height and broadening of the first peak, located at 0.273 nm. The contributions of the Zr–Zr pairs are clearly seen around 0.315 nm in the corresponding RDF of the 20-atom SCs. The statistical participations of the various clusters, as well as the interaction types (e.g. the blue column stands for Cu–Cu pairs), at each one of the peaks are depicted in the insets of Fig. 36, while inset (i) provides the important information that refers to the geometry of the bonds (i.e. core–core, core–shell or shell–shell interactions; note, for instance, that the peak at 0.238 nm is due the shell–shell interactions, contrary to what one would expect taking into account that the core–shell pairs of an ICO-like cluster have the shortest bond length). Interestingly, these tiny SCs are able to reproduce the main structural characteristics of the second neighbour distances. We should note here that, due to the finite size of the SCs, their contributions in this region are underestimated, so the appropriate corrections should be applied [152,153]. These outcomes can explain several experimental observations, e.g. the very short interatomic interactions that were interpreted as an indication of the presence of ICO-like microstructure [144,145,147].

#### ***4.6 EXTENDED ATOMIC CLUSTER ARRANGEMENTS OF Cu-Zr***

The concept of SCs is very important for understanding the nature of the short and

medium range order in MGs. The formation of SCs is the connection point between the formation of the various tiny ICO-like clusters that enhance the efficient packing in MGs and the comprehensive structure of the MGs. Accepting SCs as the basic unit that carries out all the basic structural characteristics of the MG, we had to obtain detailed information about all the existing candidate types of clusters, which combine into SCs and also, to take into account that most of them may be distorted and/or truncated. At this point CNA is no longer a sufficient method to retrieve the clusters. Additionally, the trend of the MG system in combining clusters and forming SCs should be independent on slight differences in the short range of the microstructure that depends on the growth or simulation technique. Consequently, we used the symmetry-match procedure to analyse and compare different configurations resulting from RMC and EAM MD simulations. We used this way of comparison because the RMC configurations are based strictly on the structural characteristics of the experimental MGs and do not depend on the potential model or the cooling rate used, e.g. in MD simulations.

The exhaustive analysis of both RMC and MD structural models yielded that the systems were composed basically of 13- and 15-atom clusters of ICO and RD symmetry, respectively. In addition, we found that their populations and compositions depend on the systems' stoichiometry, in agreement with previous studies [119,120,126]. Once more, we note here that the Voronoi analysis [154] is quite strict in accepting a candidate cluster, while this new methodology allowed us to find more possible clusters (including the truncated) existing in the systems. It came out that around 80% of the systems' atoms could be considered as centres of clusters, a result that supports the idea that MGs are composed by short-range ordered structures [126-129,155-158]. The percentages of Cu- and Zr-centred ICO-like clusters, with respect to the total number of clusters found in the systems are summarized in Table 13. As it can be seen, while in the Cu-rich case the clusters found in

both structural models are practically identical, in the Zr-rich system there are some differences. In particular, the RMC Zr-centred 13-atoms ICO clusters are systematically higher than those created from the MD simulations, independently from the systems' stoichiometry. Besides the potential model used, we attribute this discrepancy to the very high cooling rate, which in conjunction with the small Zr diffusivity, reveals that these atoms defer clustering, thus resulting in a system with a lower content of Zr-centred clusters.

**Table 13** – [159] The percentage of clusters composing each model system

Composition		Cu <sub>35</sub> Zr <sub>65</sub>		Cu <sub>50</sub> Zr <sub>50</sub>		Cu <sub>65</sub> Zr <sub>35</sub>	
Type of central atom		Cu	Zr	Cu	Zr	Cu	Zr
ICO clusters (13 atoms)	RMC	29.6%	29.4%	53.6%	15.1%	63.8%	7.0%
	MD	37.5%	14.9%	59.3%	6.2%	68.3%	3.0%
RD clusters (15 atoms)	RMC	0.7%	40.3%	2.8%	28.5%	10.9%	18.3%
	MD	0.4%	47.2%	2.7%	31.9%	10.0%	18.7%

Despite the slight differences in the populations of the various clusters, depending on the basic differences between the two simulation techniques, it is more important to understand whether the systems exhibit the same trend in forming SCs. Fig. 37 depicts the histograms of the SCs found from the analysis of the MD (red lines) and RMC (blue lines) equilibrium configurations for the compositions studied ((a) Cu<sub>35</sub>Zr<sub>65</sub>, (b) Cu<sub>50</sub>Zr<sub>50</sub> and (c) Cu<sub>65</sub>Zr<sub>35</sub>). We note that in the present analysis we seek only for the basic structural units, so we chose to keep primarily the smallest possible SCs; this explains the differences (only in abundances, the magic number sequences are the same) we found here compared to those given in the previous chapter. As expected, the RMC and MD configurations yield exactly the same sequences of magic numbers of SCs. It is worth noting that the only visible differences are restricted in the percentages of their relative occurrence, in which we have some small deviations. Although these SCs may have small structural differences

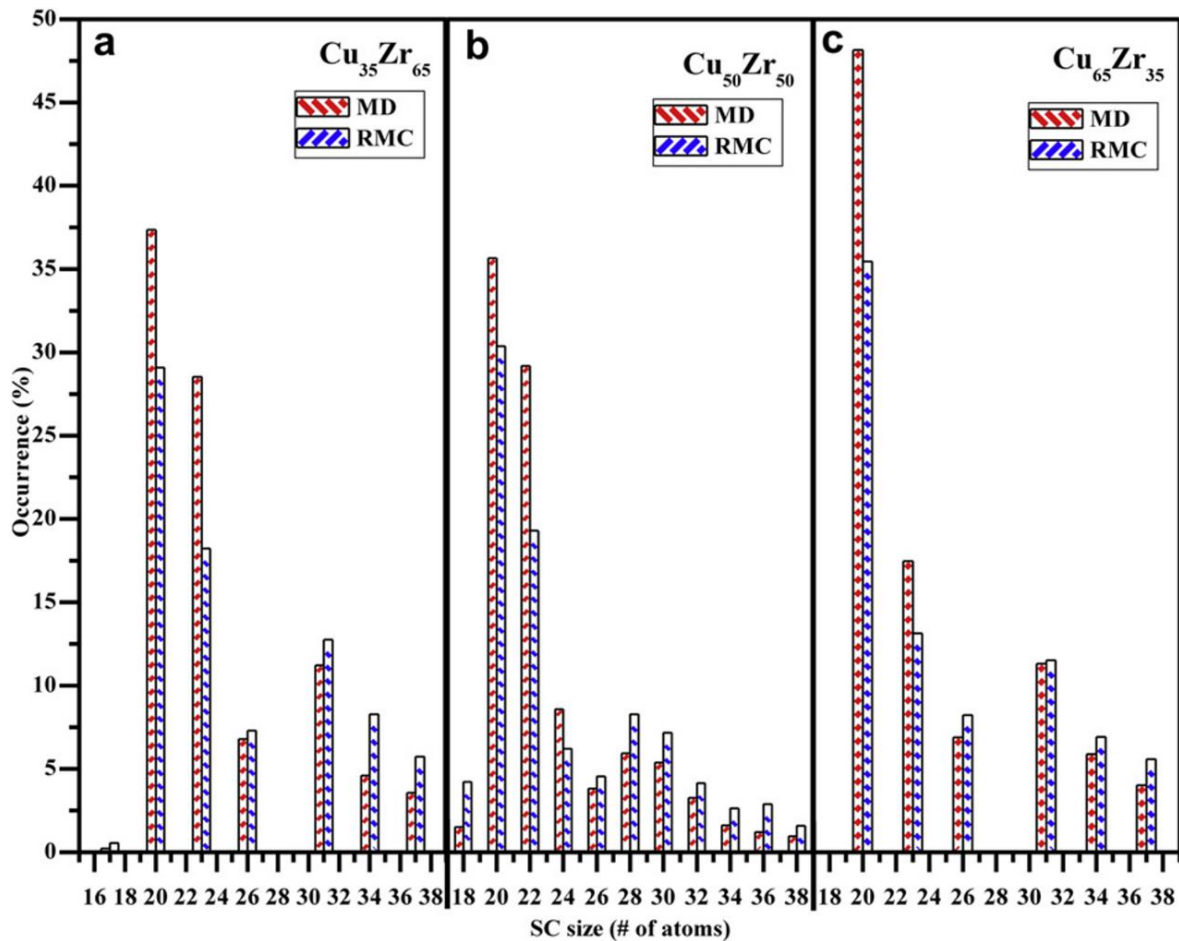


**Figure 37.** Population of SCs (%) for the three stoichiometries studied [159]  
 (a) Cu<sub>35</sub>Zr<sub>65</sub>, (b) Cu<sub>50</sub>Zr<sub>50</sub>, (c) Cu<sub>65</sub>Zr<sub>35</sub>.

occurring by the differences in the population of the various clusters, it is very interesting that their averaged RDFs are in very good agreement. Fig. 38 depicts the comparison of the averaged RDFs obtained for the SCs found from the analysis of the RMC and MD configurations for the three stoichiometries analysed. Taking into account that in the RMC simulations no potential model was used, this result implies that these SCs could have a topological origin. Consequently, the chemistry, which depends on the fine details of the MD interatomic potential model, seems to be restricted to the determination of the symmetry and the composition of the small clusters that constitute the SCs.

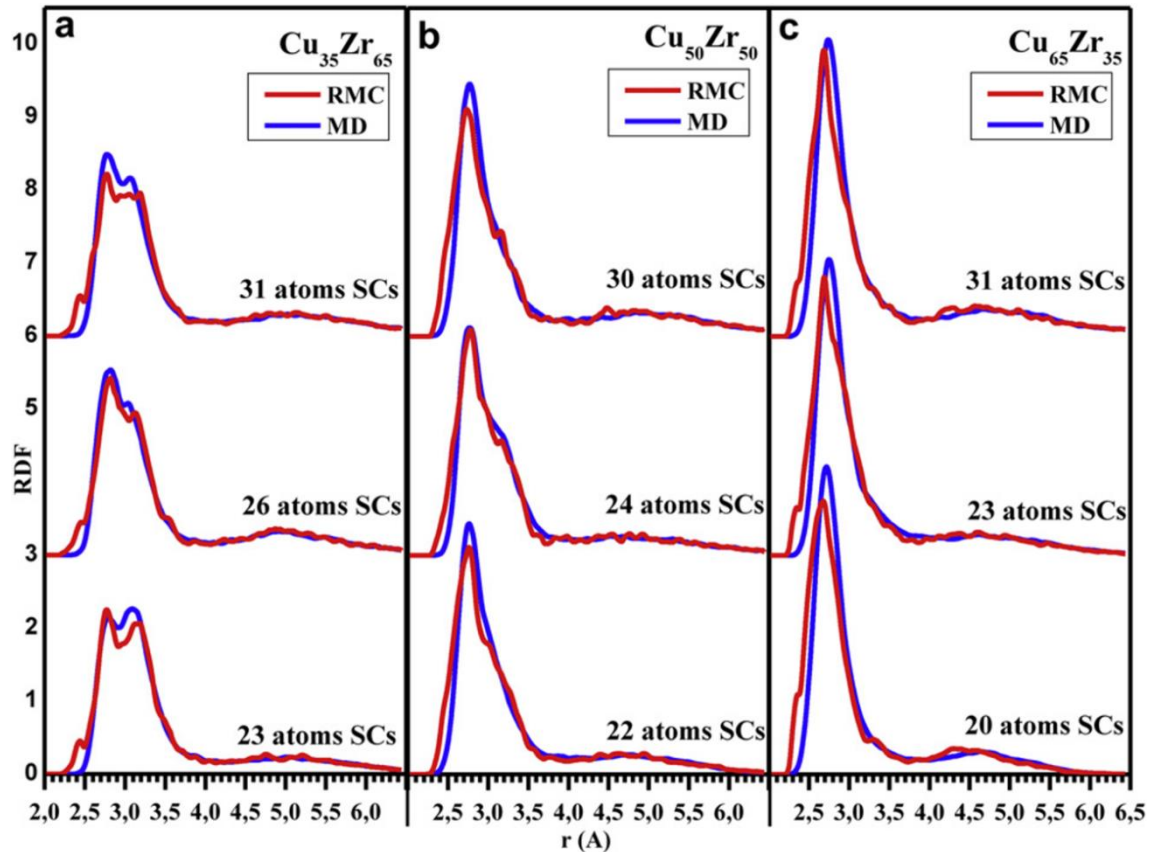


**Figure 38.** Population of SCs (%) for the three stoichiometries studied. [159]  
 (a) Cu<sub>35</sub>Zr<sub>65</sub>, (b) Cu<sub>50</sub>Zr<sub>50</sub>, (c) Cu<sub>65</sub>Zr<sub>35</sub>

Moreover the calculations reveal that the average RDFs of these SCs results in total RDFs that are in very good agreement with the experimental pair correlation functions ( $G(r)$ ) (Fig. 39). In addition, the coordination numbers deduced from these RDFs, although slightly underestimated, are in fair agreement with the available experimental data. We found 12, 11.51 and 11.05, going from the Cu-rich to Zr-rich systems, to be compared with 13.2, 12.9 and 12.4, respectively [160]. Therefore, these tiny SCs capture the characteristics of the micro-structure of these MGs and they are also able to reproduce the main structural features of the second nearest neighbour distances. We have to note here that the RDFs are normalized so that their values should converge to unity, as the radius  $r$  goes to infinity. However, due to the finite size of the SCs, their contributions in the region

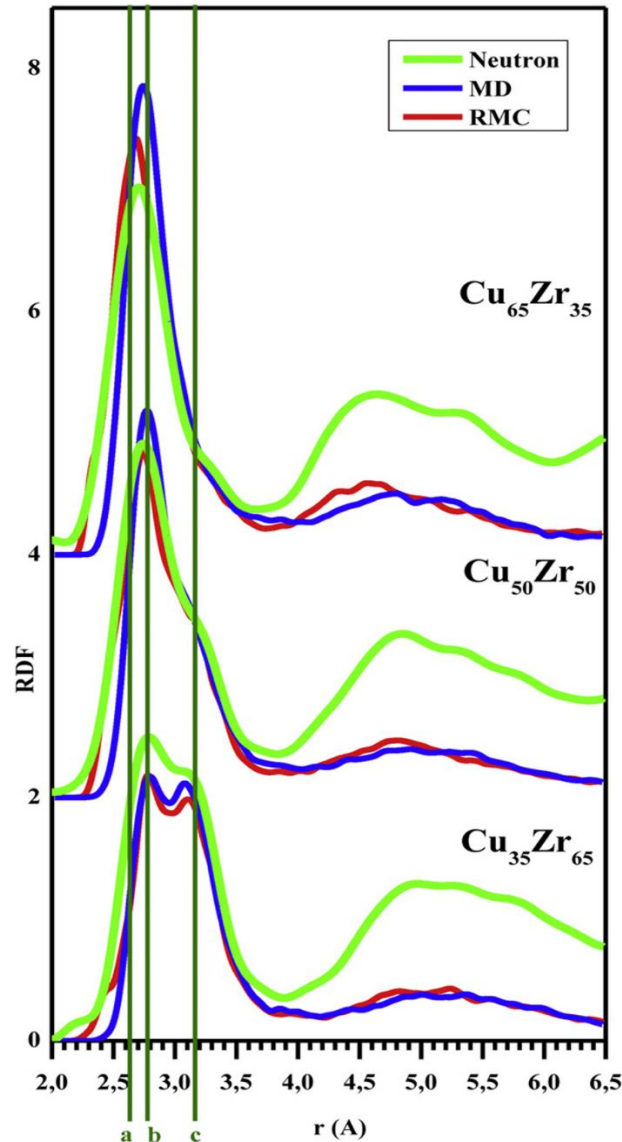


**Figure 39.** Comparison of the experimental RDFs for the three stoichiometries versus the average RDFs of the SCs found at RMC (red line) and MD (blue line) systems. [159]

above  $4\text{\AA}$  are underestimated and they have to be treated considering the appropriate corrections [152,153] (not included in the present analysis). We have also to notice that the MD RDFs fail to satisfactorily reproduce the broadening around  $0.24\text{ nm}$ , which is more important for the Cu-rich compositions; we attribute this deviation to the mass density differences between the MD model and the experimental MGs, the fine details of the Cu-Cu MD interactions and the high MD cooling rate. Moreover, it is important to mention that the MD RDF, calculated in the usual way, i.e. by counting all atom pairs, results in larger

deviations from the experimental one. It appears, therefore, that calculating the MD RDFs by means of SCs, acts as a filter of the artefacts that are due to deficiencies of the MD model and its computational limitations. In addition, it is important to point out that these results were obtained just by statistically averaging the RDFs of the SCs in absence of any kind of fitting. This strongly implies that the structural details of the MGs are closely related to the clusters that combine into SCs and compose these systems. This interpretation is in line with experimental findings referring to Cu-Zr systems with small amount of Al additions [161].

Further analysis of these SCs yielded the fine details of the atomic bonding characteristics. Fig. 40 shows the partial RDFs for the three stoichiometries studied, as obtained from the analysis of the RMC and MD configurations. From the inspection of these RDFs we can conclude, besides the general agreement obtained between the two independent simulation methods, a very important finding: the positions of the main peaks in the three partials do not change with composition, i.e. for all the investigated different stoichiometries the apparent Cu-Cu inter-atomic distance is located at 2.6 Å, the cross interactions at 2.77 Å and the Zr-Zr inter-atomic distance at 3.17 Å (a, b and c lines, respectively, at Figs. 39 and 40), in line with the available experimental results [149,162]. This means that the shift in the inter-atomic distances with the composition of the MGs, which is usually obtained and reported from the analysis of the experimental data, is in fact due only to the alterations of the relative heights of the main peaks of the partials and not to changes of the atomic bond lengths. It is worth noting, however, that even these atomic pair distances indicate just the average bond lengths of the atom pairs, the SCs having a lot of distinct contributions in several locations within these broad peaks that are originated from the multiplicity of the atomic arrangements within a cluster and a SC.

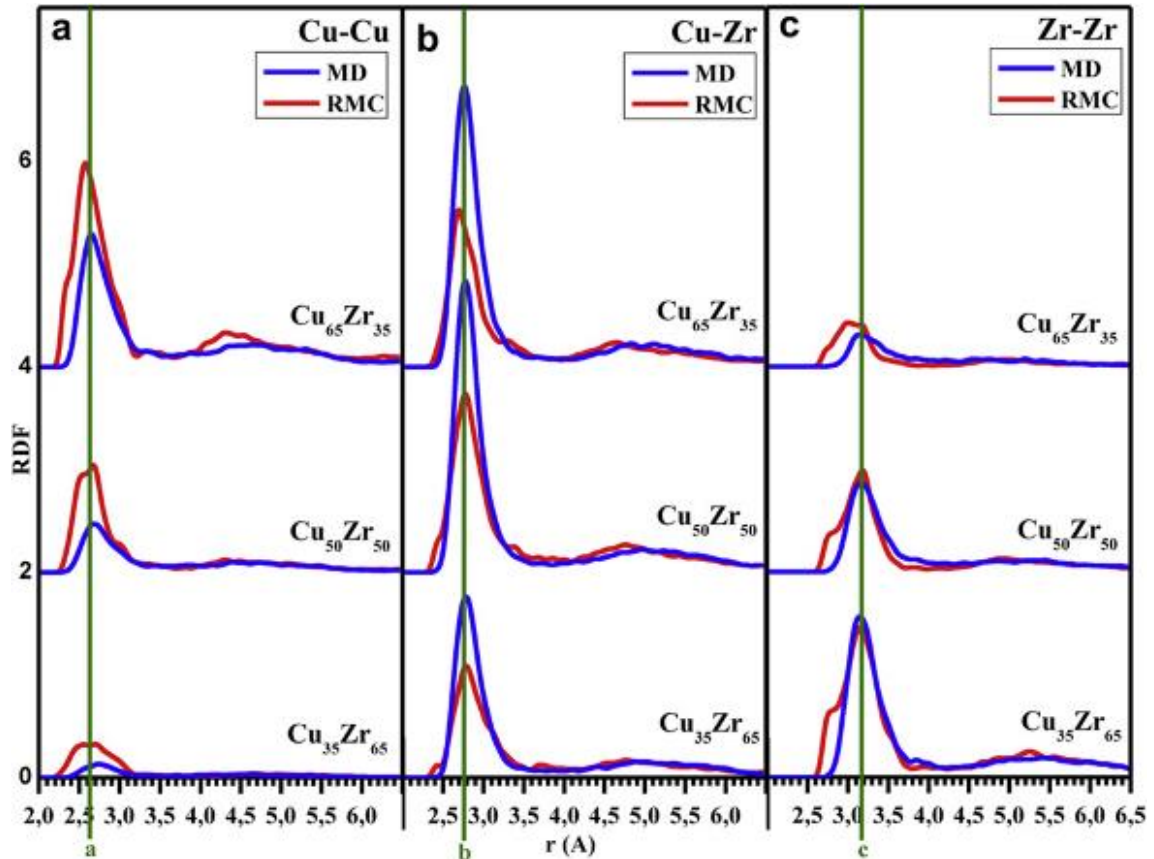


**Figure 40.** Partial RDFs: (a) Cu-Cu bonds, (b) Cu-Zr bonds and (c) Zr-Zr bonds; red line stands for SCs obtained by RMC and blue line for those by MD simulation, for all stoichiometries studied. [159]

#### 4.7 THE MD MICRO-STRUCTURE ANALYSIS OF Cu-Zr USING EXAFS

Since now we have seen that the tendency of forming various clusters is an inherent characteristic of the MGs. Moreover, we have seen that the SCs incorporate the variety of the short range order carrying out all the basic structural characteristics of the MGs, up to the medium range order. Hence, aiming in understanding in details the origin of the multiple structure characteristics in these glassy systems, we proceeded into more analytic techniques, i.e. EXAFS. Due to the disordered nature of MGs the experimentally acquired EXAFS spectrum of a glassy alloy is a statistical average of single EXAFS spectra originating from individual atomic clusters centred around the absorbing atoms present in the irradiated volume. To simulate the actual absorption experiment we evaluated a number of EXAFS

functions  $\chi(k)$  for randomly taken atomic clusters extracted from the MD configuration. During the calculation of a single EXAFS function the central atom of a cluster was treated as an absorber and the outer atoms as scattering atoms contributing to the oscillating EXAFS signal. In order to account for the atomic disorder the global EXAFS signal of the MD configuration was obtained by averaging multiple  $\chi(k)$  functions. This kind of approach is essentially ab initio and does not involve any adjustable parameters, which makes the results unambiguous and unreliable. A representative example of the variety of local atomic arrangements is demonstrated in Fig. 41 for the case of the  $\text{Cu}_{65}\text{Zr}_{35}$  system.

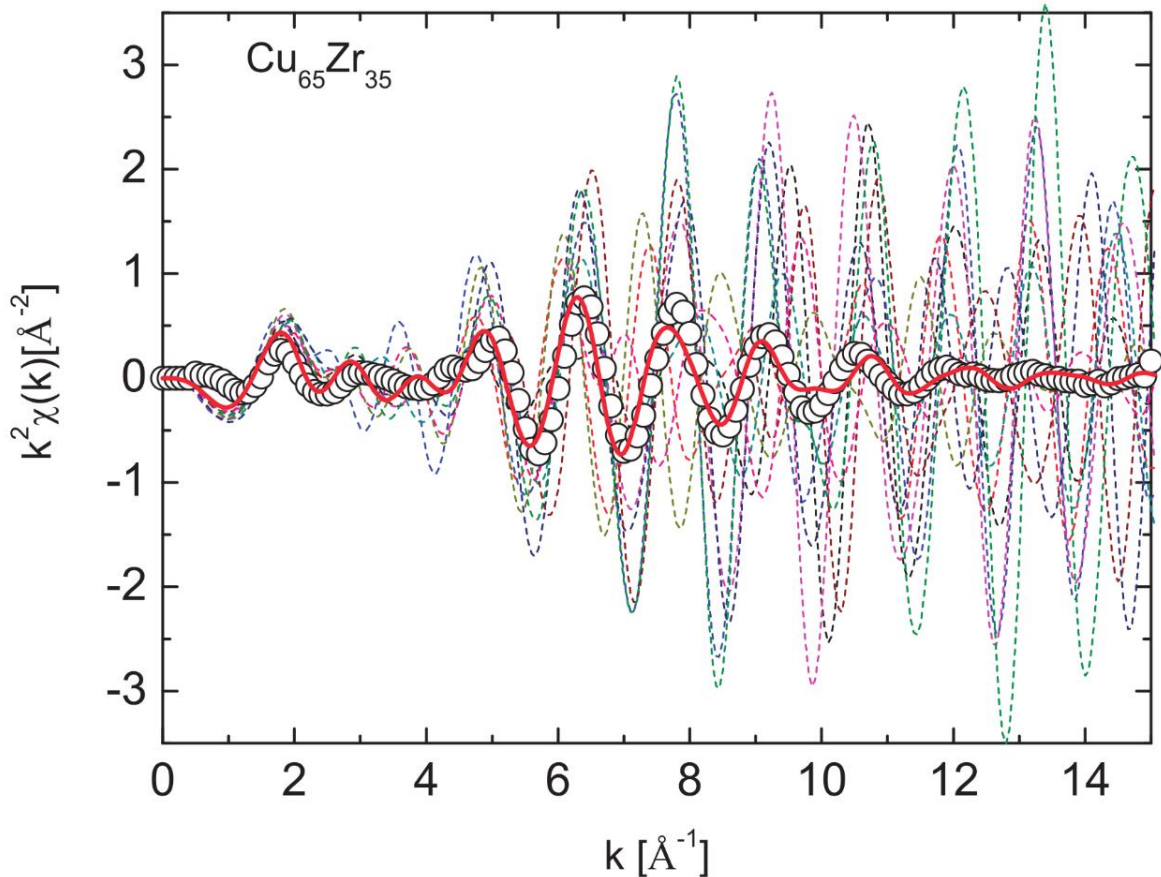


**Figure 41.**  $k^2$ -weighted  $\chi(k)$  functions for 10 random Cu atoms from the MD configuration (dashed lines), an average of 600  $\chi(k)$  functions (solid line), and the experimental Cu  $K$ -edge EXAFS spectrum of  $\text{Cu}_{65}\text{Zr}_{35}$  alloy (symbols). [163]

The plot shows  $k^2$ -weighted  $\chi(k)$  functions obtained from 10 randomly taken Cu atoms

extracted from the equilibrium MD configuration, an average of 600  $\chi(k)$  functions, and the experimental Cu *K*-edge EXAFS spectrum. It is clear that none of the single  $\chi(k)$  functions is similar to the experimental curve; however the average  $\chi(k)$  almost perfectly reproduces the experiment. We have found that at least several hundreds of  $\chi(k)$  functions have to be taken into account in order to achieve satisfactory results. Fig. 42 shows the distribution of values of  $\chi(k)$  for different values of  $k$  evaluated for 600 random Cu atoms in  $\text{Cu}_{65}\text{Zr}_{35}$ . In all cases the values of  $\chi(k)$  form a normal distribution indicating the Gaussian character of the local atomic disorder.

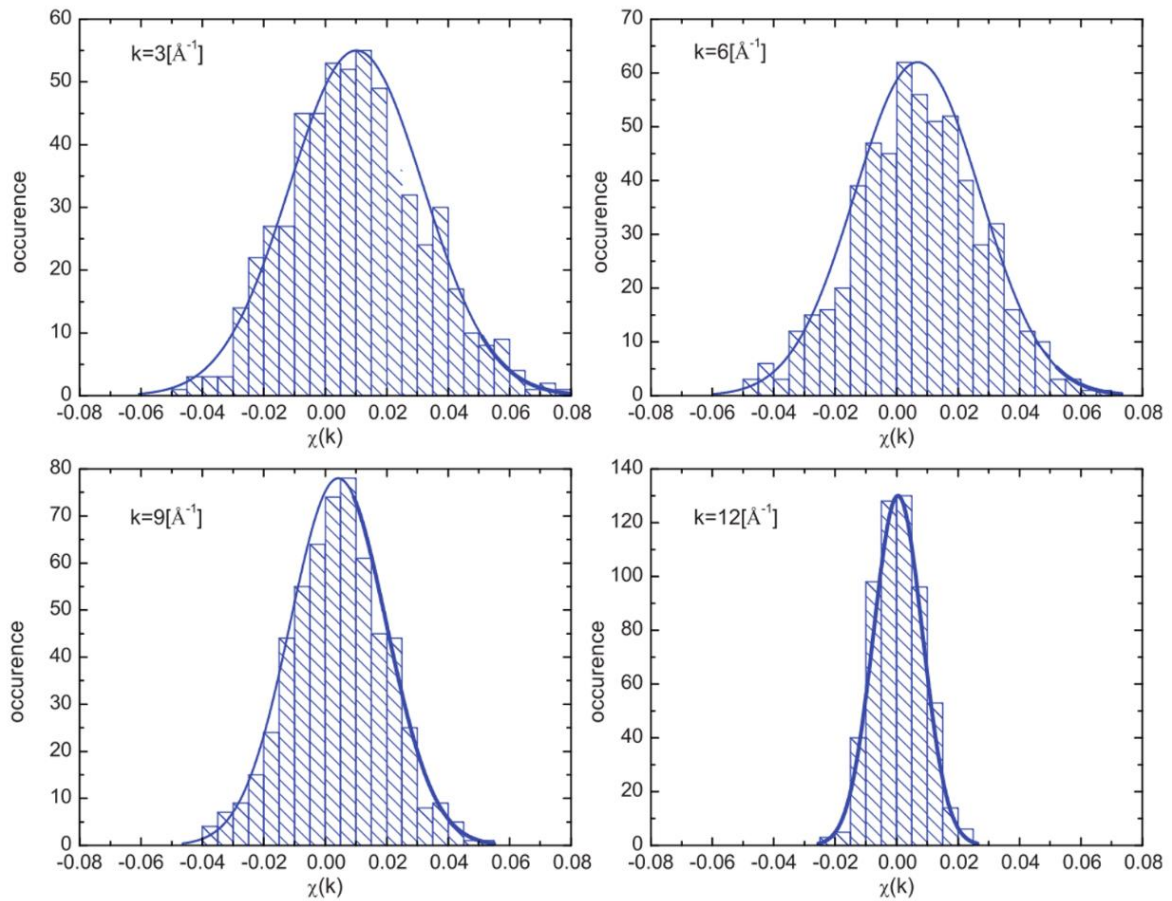


**Figure 42.** Histogram showing the distribution of values of  $\chi(k)$  for different values of  $k$  evaluated for 1000 random Cu atoms in  $\text{Cu}_{65}\text{Zr}_{35}$ . [163]

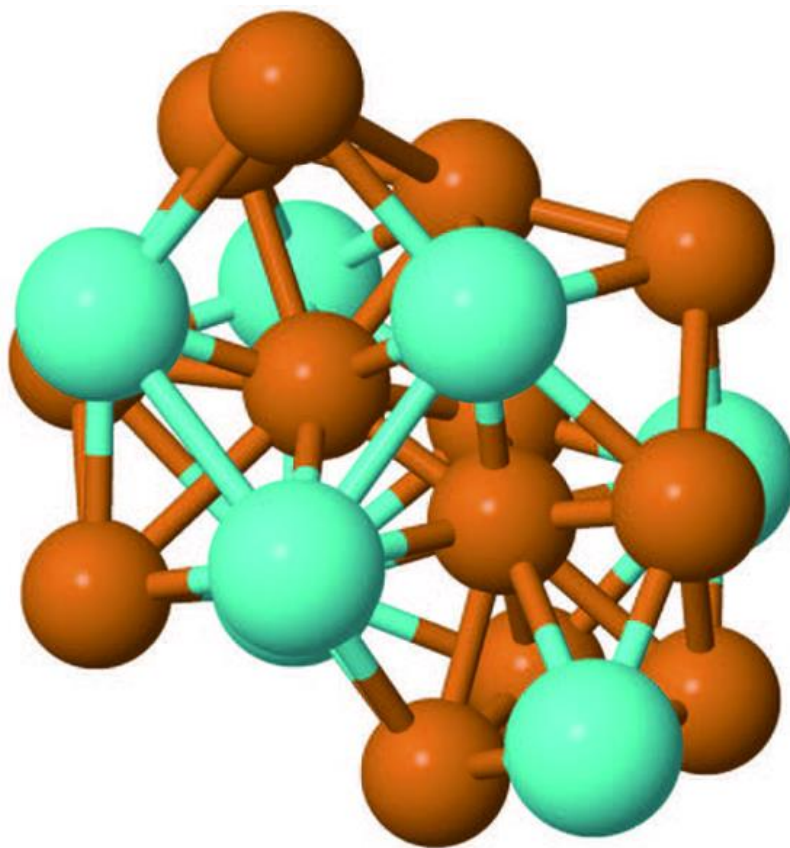
The above observations demonstrate the diversity of SRO resulting from distortion

and/or truncation of atomic clusters as well as the stochastic character of the EXAFS analysis applied to MGs. On the other hand, good agreement between the calculated and the experimental EXAFS in the absence of fitting of any kind means that the equilibrium MD configuration is representative of the actual atomic structure of the amorphous alloy.

We recall that in the case of the  $\text{Cu}_{65}\text{Zr}_{35}$  alloy 75% of the central atoms of the clusters are Cu atoms, while in the case of  $\text{Cu}_{35}\text{Zr}_{65}$ , Cu-centred ICOs comprise 20% of the total number of central atoms. EXAFS analysis is an effective tool for the analysis of the atomic arrangement within the SuperCluster composed of interpenetrating ICO clusters. The oscillatory character of EXAFS spectra results from the interference between contributions to the photoelectron wavefunction from various paths the excited photoelectron takes as it scatters off the nearest atoms. Thus, the  $\chi(k)$  function of a single SC is the sum of the  $\chi(k)$  functions from the central atoms of the clusters creating the SC. For example, for a 20-atom SC composed of two interpenetrating 13-atom icosahedral clusters, the two core (central) atoms having well-defined first coordination shells are treated as absorbing atoms contributing to the  $\chi(k)$  function from the SC. Of course the atoms that are core atoms of one cluster can act as shell atoms of the nearby overlapping cluster and from this point of view the core/shell assignment is not unique.

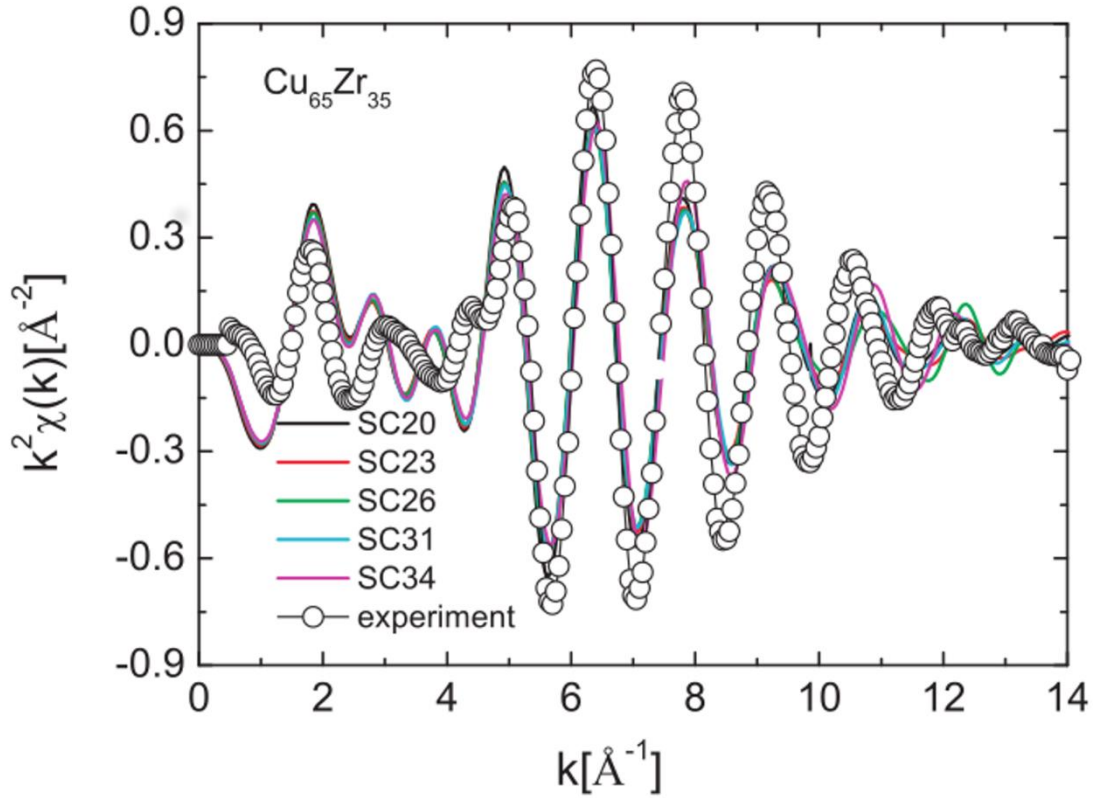
**Table 14** - [163]  
The percentage of clusters composing each model system

<b>Alloy</b>	<b>SC20</b>	<b>SC23</b>	<b>SC26</b>	<b>SC31</b>	<b>SC34</b>
$\text{Cu}_{65}\text{Zr}_{35}$	53%	14%	13%	15%	3%
$\text{Cu}_{35}\text{Zr}_{65}$	26%	27%	10%	14%	9%



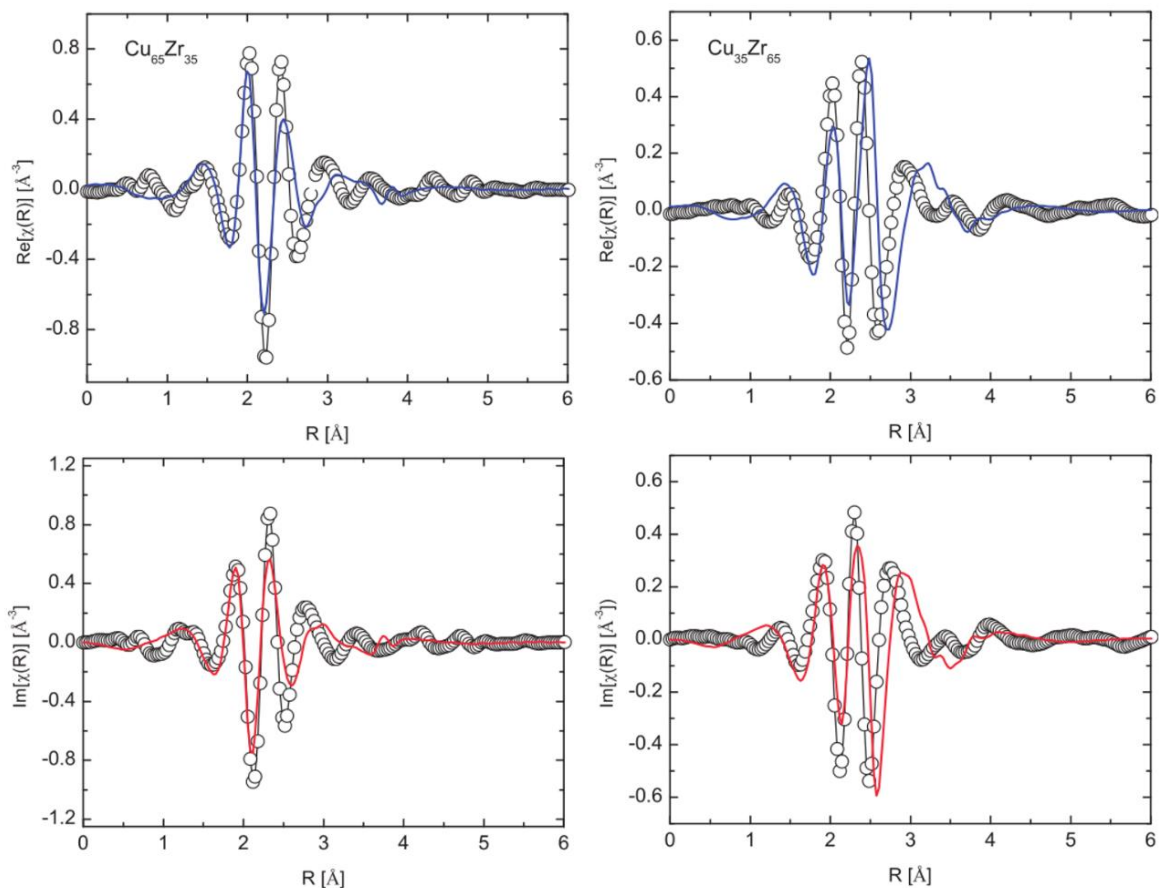
**Figure 43.** 20-atom SC composed of two interpenetrating Cu-centred 13-atom icosahedral-like clusters [163] (brown spheres represent copper and blue zirconium atoms)

Fig. 43 illustrates this situation for the case of the 20-atom SC composed of two 13-atom ICO clusters. In order to examine the characteristic structural features of the population of SCs we used the above approach to calculate the EXAFS of the five dominant types of SCs listed in Table 14. The  $\chi(k)$  functions for SCs corresponding to different magic numbers were obtained by averaging of the  $\chi(k)$  functions obtained for a given SC size. The results for  $\text{Cu}_{65}\text{Zr}_{35}$  depicted in Fig. 44 show that the calculated  $\chi(k)$  functions are very similar.



**Figure 44.**  $\chi(k)$  functions for SCs corresponding to different magic numbers (lines) and experimental EXAFS for  $\text{Cu}_{65}\text{Zr}_{35}$ . [163]

This observation indicates that the SCs of various sizes do not exhibit any distinct structural features. The above conclusion is consistent with the results of radial distribution function (RDF) analysis of the MD and reverse Monte-Carlo configurations of  $\text{Cu}_{65}\text{Zr}_{35}$  and  $\text{Cu}_{35}\text{Zr}_{65}$  alloys [159]. In order to reconstruct the EXAFS spectra of these systems we have used the SC distribution data from Table 14 to evaluate a weighted average of the  $\chi(k)$  functions. Fig. 45 presents the real and imaginary parts of the Fourier-transformed averaged spectra and the experimental EXAFS. While calculation of the weighted average has only minor effect due to the structural similarity between the SCs, the procedure allows us to improve the statistics by including more spectra in the average. The good agreement in case of both real and imaginary parts of the EXAFS function indicates that the SRO of the SCs reflects the actual local atomic arrangement of the glassy alloys.



**Figure 45.** Real (top) and imaginary (bottom) parts of the Fourier-transformed EXAFS of  $\text{Cu}_{65}\text{Zr}_{35}$  and  $\text{Cu}_{35}\text{Zr}_{65}$ . Solid lines represent the results of calculations and the symbols are experimental data points. [163]

The EXAFS method applied to amorphous solids probes only the nearest neighbour shell of the absorbing atoms. Information about the atomic structure over distances beyond the first coordination shell is embedded in the near-edge part of the absorption spectrum. To evaluate the theoretical form of the X-ray Absorption Near-Edge Structure (XANES) curve of the MD configuration we have calculated the Cu- $K$ -edge XANES for a number of random copper atoms considering multiple scattering within a sphere of 6 Å radius containing about 60 atoms. We found that increasing the radius beyond 6 Å does not affect the resulting XANES curves. Like in the case of EXAFS, the global XANES was obtained by averaging over individual spectra. As XANES involves more scattering atoms than EXAFS, convergence of the averaged spectra was faster and, according to our results, the global

spectrum remained unchanged after averaging over about 50 local XANES functions. The resulting near-edge absorption spectra for both these systems are shown in Fig. 46. In both cases most of the characteristic features of the experimental XANES are reasonably reproduced by the theoretical curves. This suggests that the atomic order of the MD configuration is consistent with that of the real alloy, not only in the sense of the chemical SRO within the first coordination shell, but also over distances of the order of 1 nm, characteristic of medium-range order and interconnection of atomic clusters.

Considering the above results we conclude that EXAFS from random Cu atoms is very close to that from atoms that are centres of ICO-like clusters creating the SCs. Indeed the analysis of the MD configuration shows that most of the atoms of the amorphous structure can be treated as central atoms of more or less strained clusters. While the statistical analysis of the local atomic arrangement yields satisfactory results, it is instructive to consider the possible form of a “representative cluster” exhibiting all the typical features of the SRO of the glassy system, such as coordination number, interatomic distances, and local symmetry.

The existence of various types of distorted and/or truncated polyhedra present in the MD configuration suggests that finding such a representative cluster might be difficult. One way for looking for such a cluster is a trial and error method based on comparing the  $\chi(k)$  of the candidate polyhedral clusters with the experimental EXAFS function. For both systems considered here the best agreement was found for the Cu-centred 13-atom icosahedral-like cluster. The cluster was constructed starting from a perfect icosahedron by surrounding the Cu atom with Cu and Zr atoms assuming ideal mixing behaviour [162,164]. The resulting cluster stoichiometries were  $\text{Cu}_8\text{Zr}_5$  for the  $\text{Cu}_{65}\text{Zr}_{35}$  alloy and  $\text{Cu}_5\text{Zr}_8$  for the conjugate composition. The Cu-Cu and Cu-Zr core-shell distances were optimized to

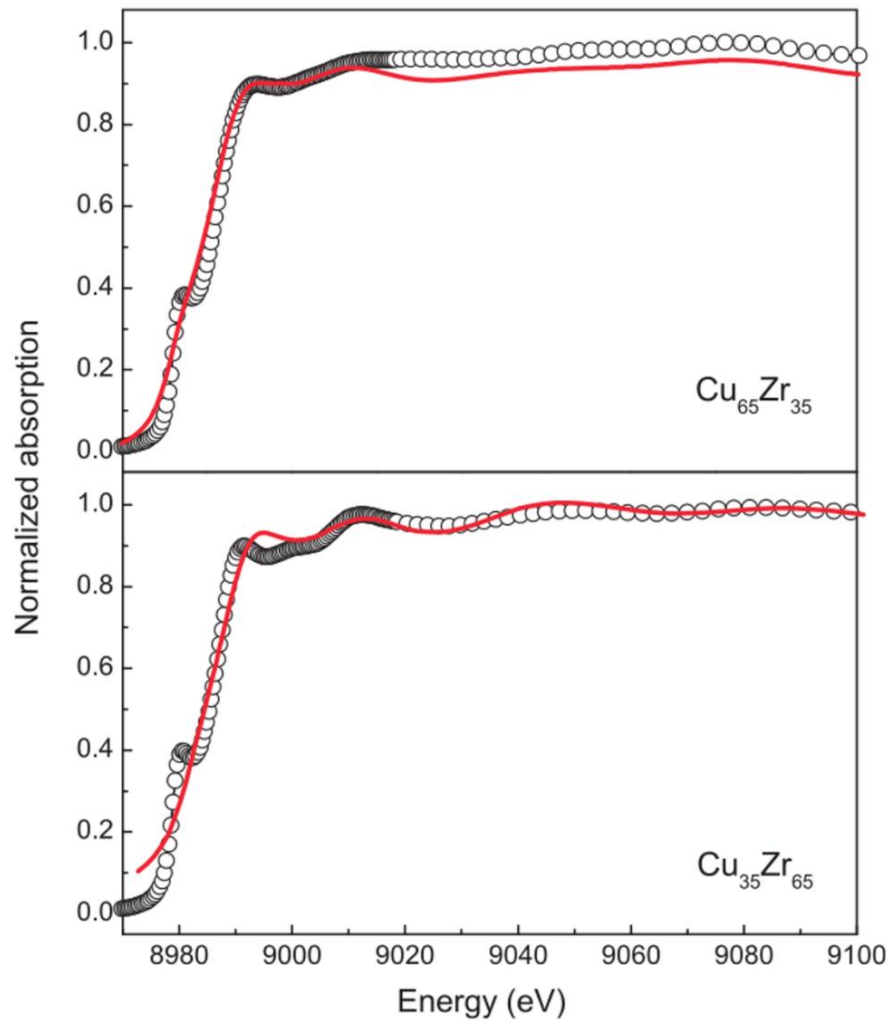


**Figure 46.** Comparison of experimental (symbols) and calculated (lines) XANES spectra of  $\text{Cu}_{65}\text{Zr}_{35}$  and  $\text{Cu}_{35}\text{Zr}_{65}$  alloys. [163]

achieve the best agreement with experiment. The best-fit values were  $2.48\text{\AA}$  for Cu-Cu and  $2.70\text{\AA}$  for Cu-Zr. The above distances are in reasonable agreement with the apparent interatomic spacing evaluated from the MD configuration ( $2.55\text{\AA}$  for Cu-Cu and  $2.73\text{\AA}$  for Cu-Zr) and, compared to the sum of the Goldschmidt radii of Cu and Zr ( $128\text{pm}$  and  $160\text{pm}$  respectively), show shrinkage of the bond distances by several percent, in agreement with our previous observations [164]. Fig. 47 depicts a comparison of the experiment and the theoretical EXAFS function calculated for the icosahedral-like cluster model.

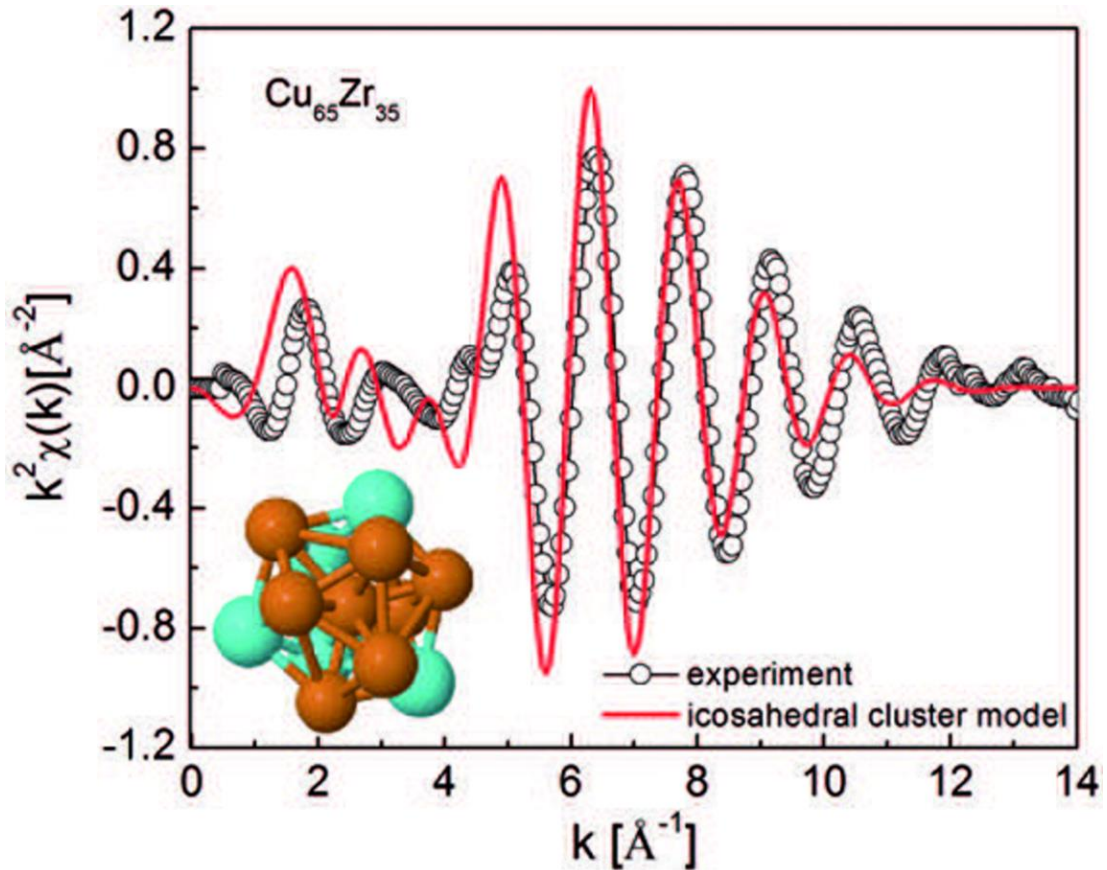


**Figure 47.** Experimental EXAFS (symbols) and theoretical  $\chi(k)$  function (line) calculated for the icosahedral-like cluster model shown in the inset. [163]

The above result shows that a “representative cluster” satisfies the condition of maximal local packing efficiency characteristic of metallic glasses. The local icosahedral arrangement involving five-fold symmetry is well known to be the most favourable structure in pure systems with pair interactions [164]. It can be argued that in the case of rapidly quenched amorphous Cu-Zr alloys the competition between maximization of the bond number and accumulation of strain leads to the development of local icosahedral symmetry. As in the case of an icosahedron, the core–shell bonds are 5% shorter than the shell–shell bonds and Cu and Zr atoms have different sizes, the spatially extended structure requires distortion and/or truncation of the icosahedra. An additional contribution to the atomic disorder comes from the high quenching rate required for achieving a configurationally frozen metastable structure containing a dispersed randomly free volume [166]. The resulting microstructure

consists of a population of icosahedral-like interpenetrating clusters. The five-fold symmetry of the SRO is incompatible with long-range order and thus acts as a kinetic barrier for nucleation and growth of competing crystalline phases providing thermal stability of the system. Our present results show that the atomic disorder of Cu-Zr MGs has a Gaussian character. This suggests that the icosahedral clusters are strained randomly to adapt to the homogeneous amorphous structure.

#### ***4.8 CLUSTERING, MICROALLOYING AND MECHANICAL PROPERTIES IN Cu-Zr BY MD AND AB-INITIO CALCULATIONS***

We have seen that the secret for the basic structural characteristics of the MGs is hidden to the coexistence of the various SCs that are present in the studied systems and that their stability depends on the presence of the ICO clusters. Though, we have not discover yet how these SCs are related with the inner structural changes that take place under tension. We proceed in detailed analysis on MD trajectories which yielded that under tensile deformation the ICO-like clusters are destructed and recreated [126], while the formation of SCs is also manifested during this dynamical process. A representative example of such a processes is depicted in Fig. 48 in a sequence of snapshots.

As it can be seen, the initial amorphous matrix (Fig. 48a), is locally transformed, an ICO cluster is formed at strain of 0.6‰ (Fig. 48b), followed by the creation of an interpenetrating second one, the processes thus resulting in the formation of a SC at strain of 0.8‰ (Fig. 48c). Interestingly, the Cu–Cu SC’s core atoms are aligned along the deformation direction

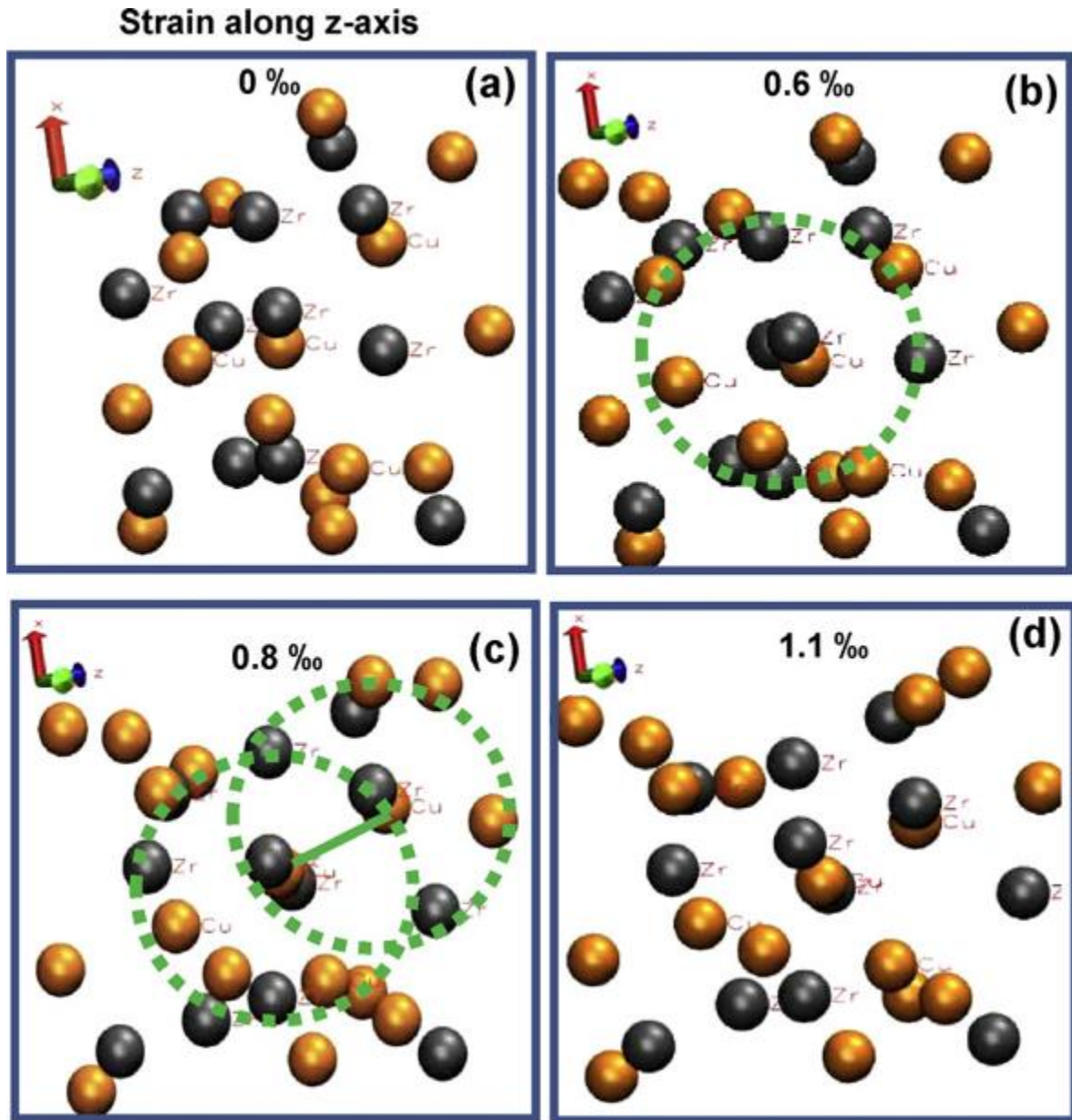


**Figure 48.** Sequence of snapshots extracted from MD trajectory of Cu<sub>46</sub>Zr<sub>54</sub> upon tensile deformation. [167]  
 (a) the initial amorphous matrix, (b) the creation of an ICO cluster,  
 (c) the SC formation from two interpenetrating ICO clusters and (d) the destruction of the SC.

persisting until the eventual SC destruction occurring at strain 1.1‰ (Fig. 48d). We note here that due to the size of the simulating system (which is comparable to the thickness of a shear band), the material dilates homogeneously, effect that is not shown in the present study that focuses on the role of clusters and SCs in the mechanical response.

In addition, we found that the application of tensile deformation affects the existing SCs

that are forced to reorganize their shapes and orientations, thus contributing in the accommodation of the mechanical solicitation. A schematic representation of this process is depicted in Fig. 49 in a sequence of snapshots. The SC's Cu–Zr core atoms that are initially randomly oriented (Fig. 49a), align along the deformation direction at strain of 0.3% (Fig. 49b), and principally by means of the Cu core atom's movements. Meanwhile, the SC is reshaped via the rearrangements of its shell atoms shown by arrows in Figs. 49b–d. It turns out therefore that in the processes shown in Figs. 48 and 49 the core–core interactions are decisive for the SCs rigidity and are fundamentally distinct from the shell–shell interactions that are weak, thus enabling the SC's reshaping. Therefore, the bonding features of these SCs, in particular when considering the various combinations of their core elements (Cu–Cu, Cu–Zr or Zr–Zr) are very important for the mechanical responses of the resulting MGs. In this direction we may also consider the microalloying effect, e.g. substitution of a core atom by Al, thus altering the mechanical properties of the resulting system. Proper treatment of these issues requires electronic structure calculations.

The electronic structure calculations on the SCs we considered provided insight in their bonding characteristics yielding some unanticipated results. In Fig. 50 we present the calculated partial electronic density of states (PEDOS) of the simple case of a 23 atom SC,  $\text{Cu}_{13}\text{Zr}_{10}$ , which is commonly found in the cases of Cu-rich MGs, considering the combinations of Cu–Cu, Cu–Zr and Zr–Zr core–core atoms (Figs. 50a–c), respectively.

The overall remarks that come out from the inspection of the SCs' EDOSes could be resumed in:

- a. At the Fermi level ( $E_F$ ), the Zr *d*-electrons are basically responsible for the filling of these energy states
- b. The wide energy band from  $-4.5$  eV to  $-2$  eV is mainly due to Cu *d*-electrons
- c. For the two lowest energy states (labelled (a) and (b)) both Cu and Zr atoms

contribute

- d. At the lowest energy states the SC's wavefunction (WF) is mainly due to core–core and core–shell atoms' hybridizations, while close to  $E_F$  is dominated by the shell–shell hybridizations (insets of Figs. 50).

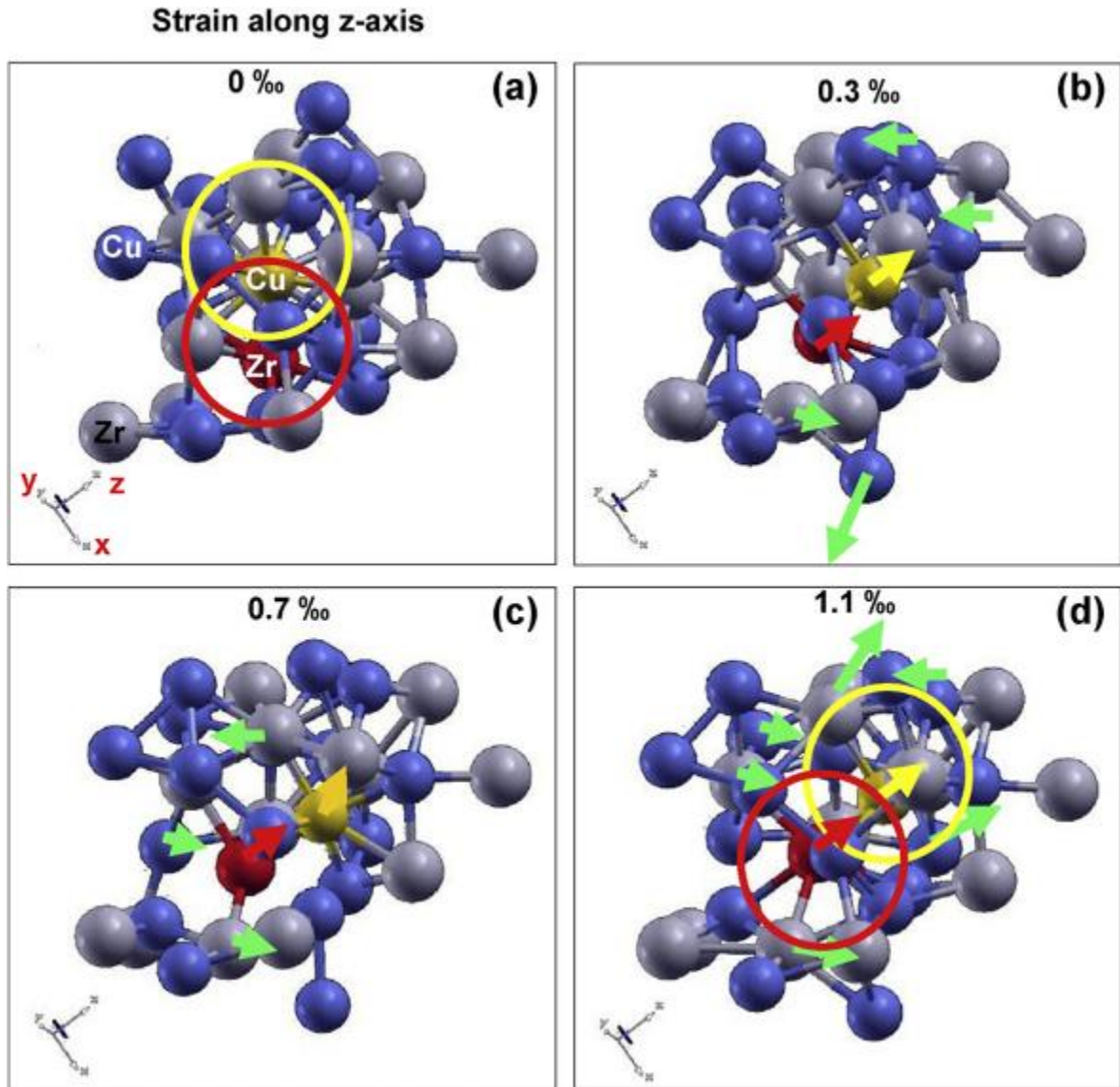


**Figure 49.** Sequence of snapshots of MD simulations on  $\text{Cu}_{65}\text{Zr}_{45}$  upon tensile deformation showing (a) a SC consisted of two interpenetrating ICO clusters, (b) the SC reshaping (c) the core–core alignment and (d) Recreation of the SC along the deformation direction. [167]

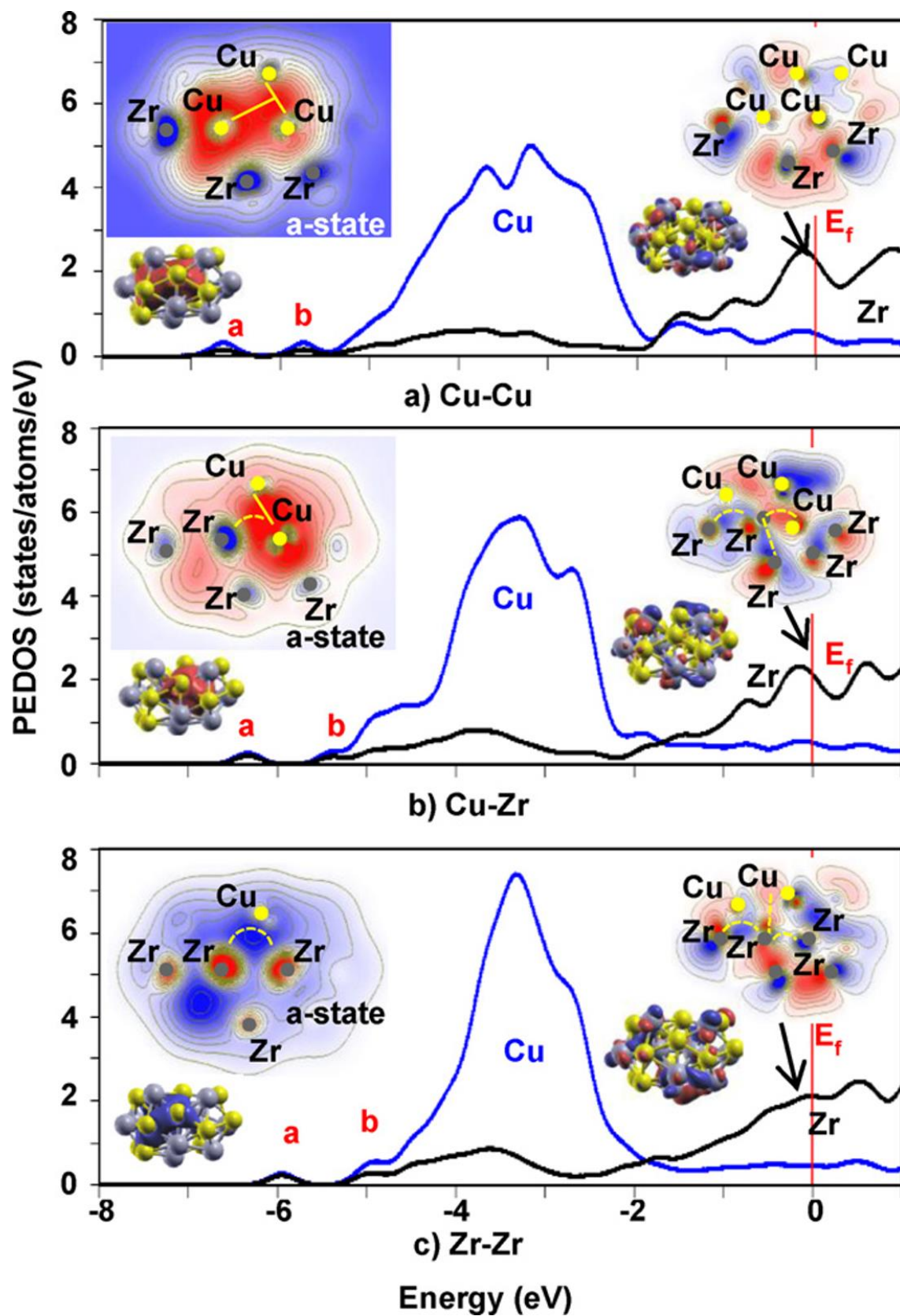


**Figure 50.** Partial electronic densities of states for SCs: (a)  $\text{Cu}_{13}\text{Zr}_{10}$  with Cu–Cu core atoms, (b)  $\text{Cu}_{13}\text{Zr}_{10}$  with Zr–Cu core atoms and (c)  $\text{Cu}_{12}\text{Zr}_{11}$  with Zr–Zr core atoms.

In each case, the insets depict the *a*-state and the highest occupied state wavefunctions.

The vertical red line denotes the Fermi level that has been set to zero.

Black and Blue lines refer to Zr and Cu contributions, respectively. [167]

More specifically In the case of a SC with Cu–Cu core atoms the lowest energy state (a-state) is marked by a directional bond between the  $d_{eg}$ -electrons of the core atoms (shown by yellow solid line), while in the SC cases with Cu–Zr or Zr–Zr core atoms no direct core–core bond was found. Nevertheless at the a-state the Cu shell atoms may form direct bonds with the Cu core atoms (Figs. 50a and b), or with the Zr core atoms ( $d_{eg}$ -electrons) (Fig. 50c), in line with previous studies [168,169]. At the Fermi level, hybridization occurs mainly between the  $d$ -electrons of the Zr shell atoms, while in the cases of Zr core atom direct bonds may be also formed (Fig. 50c). We have to note that the directional bonding is substantially different from the usual metallic one and it is closely related to the local structure and the amorphous nature of the MGs [169].

The b-state has been found for the case of single ICO clusters to selectively exhibit a free of bonds (FoB) plane depending on the valence electrons of the substitutional core atom [125]. Although for the case of Cu core  $\text{Cu}_8\text{Zr}_5$  the b-state has mainly  $d$ -electron character and therefore does not exhibit any FoB plane [125], the case of Cu–Cu centred SC yields a clear FoB plane around the energy of  $-5$  eV (Fig. 51a). Careful analysis of the Mulliken charge populations and of the wavefunction revealed that at this energy the Cu central atoms participate with their  $4s^1$  electrons, while in the other combinations of the central atoms, i.e. Cu–Zr or Zr–Zr, the  $d$ – $d$ -electron hybridizations of the Cu or Zr atoms prohibit the existence of a possible FoB plane (Figs. 51b and c, respectively).

This finding suggests that probably the existence of a FoB plane is related with  $s$  or  $p$  type contributions and consequently the effect would be accentuated upon microalloying, e.g. with Al. Aiming in exploring this possibility, we replaced the SC's core atoms with Al covering the following cases:  $\text{Cu}_{12}\text{Zr}_{10}\text{Al}_1$  having Cu–Al or Zr–Al core atoms and  $\text{Cu}_{12}\text{Zr}_9\text{Al}_2$  with Al–Al core atoms. Albeit the introduction of new lower energy states due

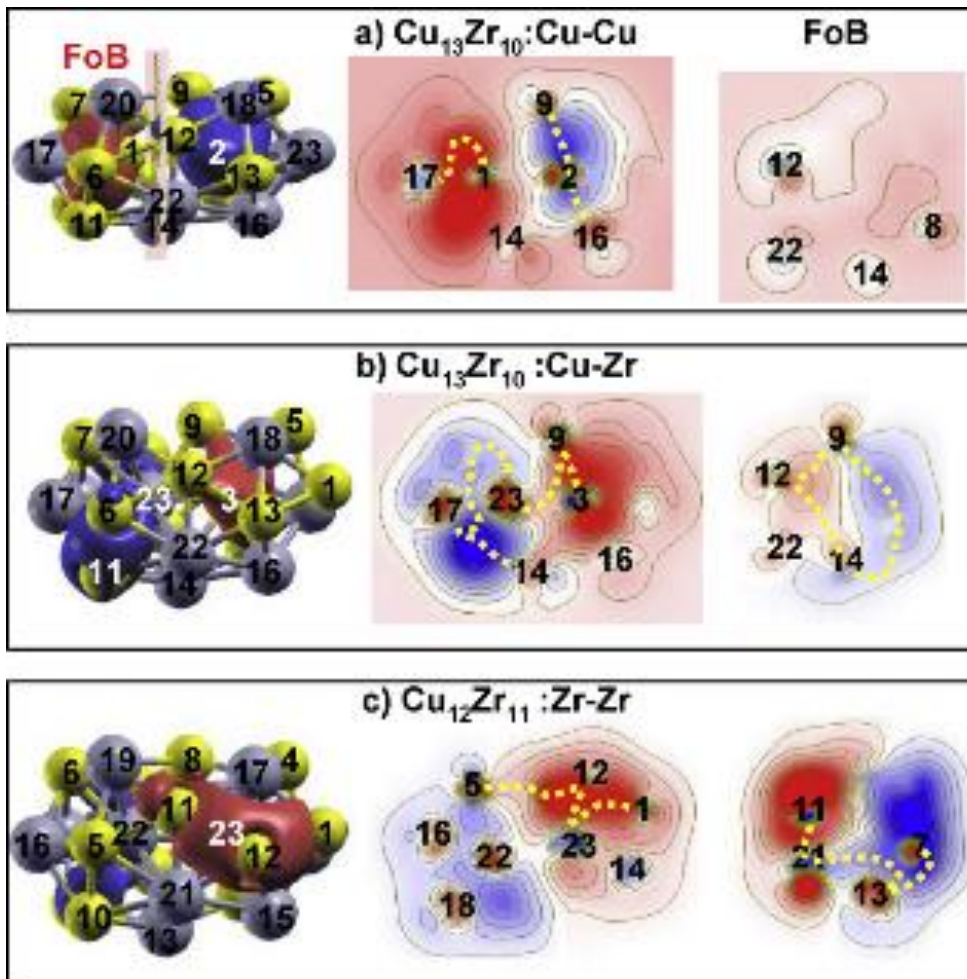


**Figure 51.** Wavefunction and contour plots around the b-state demonstrating the presence or absence of a FoB plane:  $\text{Cu}_{13}\text{Zr}_{10}$  with (a) Cu–Cu and (b) Cu–Zr core atoms, c)  $\text{Cu}_{12}\text{Zr}_{11}$  with Zr–Zr core atoms. Big (grey) and small (yellow) spheres stand for Zr and Cu atoms, respectively [167]

to the presence of Al, the basic wavefunction's characteristics persist. However, the b-state exhibits now basically *p*-electron character [168]. Interestingly, with the exception of the combination of Cu–Al centred ICO clusters, whose core atoms are bonded via *d*–*p* hybridizations (Fig. 52d), in the Zr–Al and the Al–Al core–core combinations of the  $\text{Cu}_{12}\text{Zr}_{10}\text{Al}_1$  and the  $\text{Cu}_{12}\text{Zr}_9\text{Al}_2$  SCs, respectively, the prediction for the existence of a FoB plane in presence of *s* or *p* type contributions is fulfilled (Figs. 52e and f), thus justifying the MA effect.

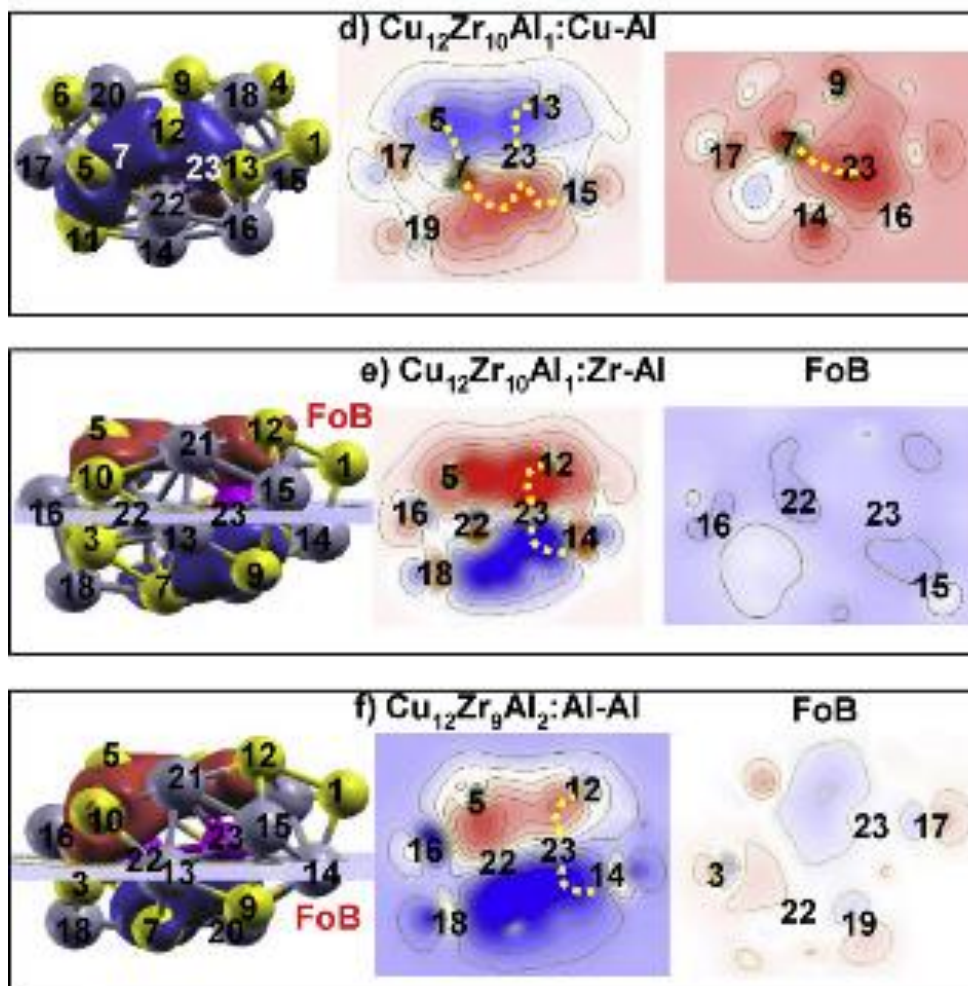


**Figure 52.** Wavefunction and contour plots around the b-state demonstrating the presence or absence of a FoB plane:  $\text{Cu}_{12}\text{Zr}_{10}\text{Al}_1$  with (d) Cu–Al and (e) Zr–Al core atoms. (f)  $\text{Cu}_{12}\text{Zr}_9\text{Al}_2$  with Al–Al core atoms. Big (grey) and small (yellow) spheres stand for Zr and Cu atoms, respectively [167]

## 5 CONCLUSIONS AND PERSPECTIVES

### 5.1 CONCLUSIONS

Several results concerning the microstructure of the MGs have been presented. We revealed the fine structural details regarding the formation of the well-known ICO clusters as well as other ICO-like types of clusters and we have seen the behaviour of these short range ordered aggregates upon system's deformation. Most importantly, we enlightened the nature of the confusion principle, an inherent characteristic of the good glass formers, by studying the origin of the formation of the various types of clusters and their evolution during the transformation of the system from liquid to solid. We analysed and revealed how these clusters combine and form larger structures, representative of the medium range order, the SCs. Moreover, we have seen the important role of the SCs on absorbing the imposed mechanical solicitation of these systems.

In details, we gave results on the microstructural characteristics of the  $\text{Cu}_x\text{Zr}_{100-x}$  ( $20 \leq x \leq 80$ ) metallic glasses. With the exception of the Zr-rich system, we found that the Cu-centred small ICO clusters are the basic structured unit of the systems, while their number and their Cu content increases with Cu content. In addition, we found that upon cooling the solidification process proceeds via the formation of such ICO clusters. The type and the compositions of the free-standing ICO clusters found by the simulations were compared and found in general agreement with ab-initio calculations within the Density Functional Theory. Moreover, we present MD simulations and DFT computations results referring to the microstructural alterations (deduced from the ICO clusters) and EDOS modifications during solidification and tensile deformation of  $\text{Cu}_{65}\text{Zr}_{35}$  and  $\text{Cu}_{50}\text{Zr}_{50}$  MGs, respectively. It came out that upon solidification and down to the glass formation temperature, the ICO number increases, while the average distances between their

constituent atoms decreases, pursuing incisively the evolution of the mean first neighbour distances, as extracted from the corresponding RDFs. In addition, we found that these changes are basically due to  $\text{Cu}_{\text{core/shell}}\text{-Cu}_{\text{shell}}$  bond shortenings, while Zr-Cu/Zr distances suffer smaller alterations. EDOSes calculated by means of DFT yielded that these inhomogeneous cluster modifications are originated from *s-s/d* strong hybridization between  $\text{Cu}_{\text{core/shell}}$  (a-state) and  $\text{Cu}_{\text{shell}}$  atoms that are shifted to lower energies, the Zr-Cu/Zr interactions exhibiting smaller changes. Furthermore, we found that upon deformation the number, the mean radius and the main EDOS characteristics of the ICO clusters remain unchanged in the elastic region, while in the plastic region their number decreases, their mean atomic distances increase similarly to the RDFs' characteristic peaks evolution and the a-state shifts towards higher energies, resulting in less stable system. It turns out therefore, that the ICO evolution under solidification or mechanical solicitation is sufficient to capture the essentials of the microstructural alterations, which are also imprinted in the corresponding EDOSes.

Subsequently we investigated the mechanisms responsible for the formation of amorphous and/or nanocrystalline bimetallic (Zr–Cu) thin films. From the MD simulations it was inferred that co-deposition of Cu and Zr atoms results in a totally amorphous overlayer that is characterized by the presence of ICO clusters that impede nucleation, while when the two elements were deposited sequentially, the resulting film manifested clear characteristics of  $\alpha\text{-Zr}$  and  $t\text{-Zr}_2\text{Cu}$  nanograins. In sequential growth and for individual layers thicker than the diffusion length, layering is observed. The MD predictions were fully verified experimentally in films grown by means of PLD and DCMS deposition techniques. The present results could be used as an alternative route for growing bimetallic either nanocomposite or glassy films with tailored properties.

Following the previous conclusion, we simulated two  $\text{Cu}_{65}\text{Zr}_{35}$  glassy systems produced

by substitutional destabilization of Cu or Zr metals and by rapid quenching. From the detailed microstructural analysis it came out that the glass produced by the pure topological instability of the crystalline phases is less “ordered”, i.e., consists of less clusters, especially ICO, in comparison with the rapidly quenched sample. Annealing of the rapidly quenched sample resulted in no significant structural differences, while the glass produced by pure topological instability of the crystalline metals evolved to a more “ordered” structure, with more clusters, especially icosahedral-like, towards the structure of the rapidly quenched sample. It turns out therefore, that no structural differences are to be expected in MGs produced by mechanical alloying and by rapid quenching; thus any differences found in MGs produced by these different processes are attributed to insufficient alloying treatment during the mechanical alloying procedure. In addition, it is concluded that the topological instability of the crystalline phases is the main mechanism of amorphization, for both, rapidly quenching and mechanical alloying processes. However, the large negative heat of mixing between different atomic elements is fundamental to render the amorphous structure more “stable”, i.e., the atomic affinity, and the atomic size mismatch, as well as the relative amount among the different elements, leads to the formation of complex and interpenetrating clusters which, in turn, slows down the crystallization process.

Having in mind the existence of clusters’ networks, we have presented results showing that the microstructure of the model MG we studied consists of SuperClusters that can be formed from the interconnections of ICO-like clusters according to a simple rule that takes into account the system’s stoichiometry. It turns out that these SCs obey a sequence of magic numbers and that they can reproduce all the basic structural characteristics of the system. We presented results showing that both MD and RMC simulations agree on the existence and the populations of SCs in Cu-Zr MGs. It turned out that each type of these SCs exhibits similar RDF’s features, while their statistical averages reproduce satisfactorily the

experimental RDFs. These findings indicate that these SCs can be regarded as basic structural units and that clustering in these MGs may have topological origin. In addition, the effect of possible chemical short-range ordering looks to be restricted by the composition of the small clusters that combine together to form the SCs. Under this perspective the fine details of the MD inter-atomic potential do not appear as a decisive factor for the formation of SCs. Moreover, the partial RDFs revealed that the stoichiometry of the system does not influence the positions of the principal first nearest neighbour RDFs peaks, suggesting that the changes in the experimental RDFs with composition are due only to the alterations in the relative heights of the pair correlation functions.

Aiming in revealing the correlation of the fine details of the microstructure with the SCs, we demonstrated a method of direct comparison of the results of MD simulations with the experimental X-ray absorption data. The method is based on ab initio calculations of EXAFS and XANES spectra from the atomic coordinates obtained from the MD. Our approach allows for the verification of the applicability of the pair interaction potentials used in MD simulations by comparing the experimental and theoretical EXAFS and XANES spectra. In the case of  $\text{Cu}_{65}\text{Zr}_{35}$  and  $\text{Cu}_{35}\text{Zr}_{65}$  MGs, our method proves that the atomic arrangement of the MD configuration is consistent with that of a real glassy alloy over distances ranging from the nearest neighbour spacing up about 1 nm. The analysis of the population of the SCs showed that different types of SCs do not exhibit any distinct structural features and their average  $\chi(k)$  reproduces the experimental EXAFS. We have found that the dominant SRO motif in both alloys can be approximated by an ICO-like Cu-centred cluster obeying the condition of maximal local packing efficiency. However it must be noted that due to the stochastic character of the EXAFS function of the amorphous system a single-cluster model cannot account for the variety of local atomic arrangements present in the population of the SCs. Our findings indicate that in the case of Cu-Zr MGs the

chemical SRO tends to maximize the local packing density while adapting the stoichiometry of the cluster to the global system composition with interatomic distances within the cluster being composition independent. This observation is consistent with our previous results on EXAFS fitting and RDF analysis showing that, despite the negative heat of mixing of -23 kJ/mol, Cu-Zr systems exhibit no specific bonding preferences as predicted from an ideal solution. The Gaussian distribution of the EXAFS function from individual absorbing sites suggests that Cu-centred ICOs are strained randomly to form an interconnected cluster structure. We concluded that the interconnections between the clusters and consequently the formation of the SCs is thus of topological rather than chemical origin.

Moreover, we investigated the behaviour of these structures upon tensile deformation. It came out that the SCs follow a dynamic process of destruction and recreation during which the SCs' core-core atoms are aligned along the deformation direction and the shell atoms reorganize their positions and reshape the SCs. Density functional theory calculations revealed that the Zr *d*-electrons dominate the states close to the Fermi level, they are responsible mainly for the shell-shell interactions, while the Cu contributions are essentially localized well below  $E_F$ . The low energy states are due to core-core and core-shell interactions, while interestingly we found that in the case of SC with Cu-Cu core atoms the participation of Cu  $4s^1$  electrons at these states results in a free of bonds plane, which could be considered as the analogue of the slip planes of crystalline materials. The effect of electronic depletion at certain energies due to the presence of *s* or *p* electrons in a *d* environment was further explored considering the case of Al microalloying. We found that substitution of a SCs core atom with Al results in the manifestation of a FoB plane, with the exception of the Cu-Al core-core atoms due to their *d-p* hybridizations. It turns out therefore that the electronic structure of the SCs, which compose the MGs, is closely related to their mechanical properties and the microalloying effect. We think that this approach could

ultimately lead to the possible design of metallic glasses with predefined properties.

## ***5.2 PERSPECTIVES***

Understanding the tendency of the Cu-Zr systems to form a multitude of nanostructures, i.e. clusters, revealed us the mechanisms behind the confusion principle, a major characteristic of the good glass-formers. More extended investigation about the thermodynamic correlation between the various clusters as well as the connection of a specific stoichiometry with its preferable structural symmetry would allow us to make a pattern that connects the system's elemental composition with its resulting microstructure thus, granting us the privilege to design MGs with the desired properties.

Discovering the mechanism through which the ICO clusters, and furthermore the SCs, absorb the deformation imposed to the system is the first step for the complete analysis of the mechanical properties of the MGs. Further investigation should be focused on finding the correlation of the other symmetries found with the deformation, as well as to understand how the external pressure affects the various nanostructures. Answering these questions would give us the advantage of choosing a system with the appropriate microstructure for a specific application.

## REFERENCES

- 1) W. Klement, R.H. Willens, P. Duwez, *Nature* 187 (1960) 869.
- 2) A.L. Greer, *Science* 267 (1995) 1947.
- 3) W.L. Johnson, *Prog. Mater. Sci.* 30 (1986) 81.
- 4) H.A. Daveis, in: F.E. Luborsky (Ed.), *Amorphous Metallic Alloys*, Butterworths, London, 1983 p.8.
- 5) S. Kavesh, in: J.J. Gillman, H.L. Leamy (Eds.), *Metallic Glasses*, ASM International, Metals Park, OH, 1978 Chapter 2.
- 6) D. Turnbull, *Trans. AIME* 221 (1961) 422.
- 7) H.S. Chen, D. Turnbull, *J. Chem. Phys.* 48 (1968) 2560.
- 8) H.S. Chen, D. Turnbull, *Acta Metall.* 17 (1969) 1021.
- 9) D. Turnbull, J.C. Fisher, *J. Chem. Phys.* 17 (1949) 71.
- 10) D. Turnbull, *Contemp. Phys.* 10 (1969) 437.
- 11) W.L. Johnson, *MRS Bull.* 24 (10) (1999) 42.
- 12) H.S. Chen, *Acta Metall.* 22 (1974) 1505.
- 13) A.L. Drehman, A.L. Greer, D. Turnbull, *Appl. Phys. Lett.* 41 (1982) 716.
- 14) W.H. Kui, A.L. Greer, D. Turnbull, *Appl. Phys. Lett.* 45 (1984) 615.
- 15) A. Inoue, T. Zhang, T. Masumoto, *Mater. Trans. JIM* 30 (1989) 965.
- 16) A. Inoue, *Acta Mater.* 48 (2000) 279.
- 17) A. Inoue, T. Nakamura, N. Nishiyama, T. Masumoto, *Mater. Trans. JIM* 33 (1992) 937.
- 18) A. Inoue, *Mater. Trans. JIM* 36 (1995) 866.
- 19) A. Inoue, T. Zhang, N. Nishiyama, K. Ohba, T. Masumoto, *Mater. Trans. JIM* 34 (1993) 1234.

- 20) A. Inoue, N. Nishiyama, *Mater. Sci. Eng. A* 226–228 (1997) 401.
- 21) A. Peker, W.L. Johnson, *Appl. Phys. Lett.* 63 (1993) 2342.
- 22) W.H. Wang, C. Dong, C.H. Shek, *Mater. Sci. and Eng. R* 44 (2004) 45.
- 23) F.Q. Guo, S.J. Poon, G.J. Shiflet. *Appl. Phys. Lett.* 84 (2004) 37.
- 24) J. Pu, J.F. Wang, J.Z. Xiao. *Nonferr Metal Soc.* 13 (2003) 1056.
- 25) M.B. Tang, D.Q. Zhao, M.X. Pan W.H. Wang, *Chinese Phys. Lett.* 21 (2004) 901.
- 26) A. Inoue, W. Zhang, *Mater. Trans.* 45 (2004) 584.
- 27) D. Xu. B. Lohwongwatana, G. Duan, W.L. Johnson, C. Garland, *Acta Mater.* 52 (2004) 2621.
- 28) A.L. Greer, *Nature* 366 (1993) 303.
- 29) A. K. Doolittle, *J. Appl. Phys.* 22 (1951) 1471.
- 30) M. H. Cohen, D. Turnbull, *J. Chem. Phys.* 31 (1959) 1164.
- 31) L.E. Tanner, R. Ray, *Acta Metall.* 27 (1979) 1727.
- 32) X.H. Lin, W.L. Johnson, *J. Appl. Phys.* 78 (1995) 6514.
- 33) Z.P. Lu, C.T. Liu, *Acta Mater.* 50 (2002) 3501–3512.
- 34) A. Peker, Ph.D. Dissertation, California Institute of Technology, 1994.
- 35) R. Busch, *JOM* 52(7) (2000) 39.
- 36) M. Heilmaier, J. Eckert, *JOM* 52(7) (2000) 43.
- 37) C.A. Angell, *Science* 267 (1995) 1924.
- 38) R. Busch, W. Liu, W.L. Johnson, *J. Appl. Phys.* 83 (1998) 4134.
- 39) H. Tanaka, *Phys. Rev. Lett.* 90 (2003) 055701.
- 40) A. Meyer, J. Wuttke, W. Petry, *Phys. Rev. Lett.* 80 (1998) 4454.
- 41) A. Meyer, R. Busch, H. Schober, *Phys. Rev. Lett.* 83 (1999) 5027.
- 42) S.R. Nagel, J. Tauc, *Phys. Rev. Lett.* 35 (1975) 380.
- 43) S.R. Nagel, *Phys. Rev. B* 16 (1977) 1694.

- 44) S.R. Nagel, J. Vassiliou, P.M. Horn, B.C. Giessen, *Phys. Rev. B* 17 (1978) 462.
- 45) P. Haeussler, F. Baumann, J. Krieg, G. Indlekofer, P. Oelhafen, H.-J. Guentherodt, *Phys. Rev. Lett.* 41 (1983) 714.
- 46) P. Haeussler, *Phys. Rep.* 222(2) (1992) 65.
- 47) U. Mizutani, *Prog. Mater. Sci.* 28 (1983) 97.
- 48) U. Mizutani, K.T. Hartwig, T.B. Massalski, R.W. Hopper, *Phys. Rev. Lett.* 41 (1978) 661.
- 49) U. Mizutani, K. Yashino, *J. Phys.* F14 (1984) 1179.
- 50) A. Inoue, W. Zhang, T. Zhang, K. Kurosaka, *Acta Mater.* 49 (2001) 2645.
- 51) A. Inoue, T. Zhang, A. Takeuchi, *Appl. Phys. Lett.* 71 (1997) 464.
- 52) C.A. Schuh, T.G. Nieh, Y. Kawamura, *J. Mater. Res.* 17 (2002) 1651.
- 53) C.A. Schuh, T.G. Nieh, *Acta Mater.* 51 (2003) 87.
- 54) K.M. Flores, R.H. Dauskardt, *Acta Mater.* 49 (2001) 2527–2537.
- 55) A. Inoue, A. Takeuchi, *Mater. Trans. JIM* 43 (2002) 1892.
- 56) D. Schreiber, *Elastic Constants and their Measurement*, McGraw-Hill, New York, 1973.
- 57) D.E. Gray, *American Institute of Physics Handbook*, 3rd ed., McGraw-Hill, New York, 1973 (Chapter 3).
- 58) H.S. Chen, J.T. Krause, E. Coleman, *J. Non-Cryst. Solids* 18 (1975) 157.
- 59) L.M. Wang, W.H. Wang, R.J. Wang, Z.J. Zhan, D.Y. Dai, L.L. Sun, W.K. Wang, *Appl. Phys. Lett.* 77 (2000) 1147.
- 60) W.H. Wang, R.J. Wang, D.Q. Zhao, M.X. Pan, Y.S. Yao, *Phys. Rev. B* 62 (2000) 11292.
- 61) R. Wang, *Nature* 278 (1979) 700.

- 62) A. Inoue, T. Negishi, H.M. Kimura, T. Zhang, A.R. Yavari, *Mater. Trans. JIM* 39 (1998) 318.
- 63) J. Schroers, W.L. Johnson, R. Busch, *Appl. Phys. Lett.* 76 (2000) 2343.
- 64) J. Schroers, W.L. Johnson, *J. Appl. Phys.* 88 (2000) 44.
- 65) J. Schroers, A. Masuhr, W.L. Johnson, R. Busch, *Phys. Rev. B* 60 (1999) 11855.
- 66) J. Schroers, R. Busch, A. Masuhr, W.L. Johnson, *Appl. Phys. Lett.* 74 (1999) 2806.
- 67) T.A. Waniuk, J. Schroers, W.L. Johnson, *Appl. Phys. Lett.* 78 (2001) 1213.
- 68) J. Schroers, Y. Wu, R. Busch, W.L. Johnson, *Acta Mater.* 49 (2001) 2773.
- 69) W.H. Wang, *J. Metastable Nano-Cryst. Mater.* 15/16 (2003) 73.
- 70) W.H. Wang, D.W. He, D.Q. Zhao, Y.S. Yao, M. He, *Appl. Phys. Lett.* 75 (1999) 2770.
- 71) W.H. Wang, Y.X. Zhuang, M.X. Pan, Y.S. Yao, *J. Appl. Phys.* 88 (2000) 3914.
- 72) Z. Zhang, L. Xia, R.J. Wang, B.C. Wei, M.X. Pan, W.H. Wang, *Appl. Phys. Lett.* 81 (2002) 4371.
- 73) J.J. Kim, Y. Choi, S. Suresh, A.S. Argon, *Science* 295 (2002) 654.
- 74) J. Zhang, K.Q. Qiu, A.M. Wang, H.F. Zhang, M.X. Quan, Z.Q. Hu, *J. Mater. Res.* 17 (2002) 2935.
- 75) A. Gebert, J. Ekert, L. Schultz, *Acta Mater.* 46 (1998) 5475.
- 76) M. Yousuf, K.G. Rajan, *J. Mater. Sci. Lett.* 3 (1984) 149.
- 77) V. T. Witusiewicz, F. Sommer, *Journal of Alloys and Compounds*, 289, (1999), 152-167
- 78) Inoue, D Kawase, A.P Tsai, T Zhang, T Masumoto, *Mater. Sci. Eng., A* 178 (1994) 255.
- 79) E. Kneller, Y. Khan, U. Gorres, *Metallkd.* 77(3) (1986) 152.
- 80) G. Duan, D. Xu, Q. Zhang, G. Zhang, T. Cagin, W. L. Johnson, and W. A. Goddard *Phys. Rev. B* 71 (2005) 224208

- 81) Computational Materials Science: A Scientific Revolution about to Materialize, (White Paper, Materials Component Strategic Simulation Initiative, DOE, USA, 1999).
- 82) W. Hergert, A. Ernst, M. De, Computational Materials Science: From Basic Principles to Material Properties, Springer-Verlag, New York, 2004.
- 83) D. Raabe, Computational Materials Science, Wiley-VCH, New York, 1998.
- 84) S. Erkoç, Phys. Rep. 278 (1997) 80.
- 85) K. Ohno, K. Esfarjani, Y. Kawazoe, Computational Materials Science: From Ab Initio to Monte Carlo Methods, Springer, Berlin, 1999.
- 86) R.L. McGreevy, J. Phys.: Condens. Matter 13 (2001) R877
- 87) K. Binder, Applications of the Monte Carlo Method in Statistical Physics, Springer-Verlag, Berlin, 1987.
- 88) W.G. Hoover, Molecular Dynamics, Springer-Verlag, Berlin, 1986.
- 89) B.J. Alder, T.E. Wainwright, J. Chem. Phys. 27 (1957) 1208.
- 90) A. Rahman, Phys. Rev. 136 (1964) A405.
- 91) L. Verlet, Phys. Rev. 159 (1967) 98.
- 92) L. Verlet, Phys. Rev. 165 (1968) 201.
- 93) H.C. Andersen, J. Chem. Phys. 72 (1980) 2384.
- 94) W.G. Hoover, Phys. Rev. A 31 (1985) 1695.
- 95) D.J. Evans, W.G. Hoover, B.H. Failor, B. Moran, A.J.C. Ladd, Phys. Rev. A 28 (1983) 1016.
- 96) G. Ciccotti, W.G. Hoover, Molecular-dynamics simulation of statistical-mechanical system, in: Proceedings of the International School of Physics, ASI-NATO, Monastero, Italy, 1986.
- 97) S. Nose, Mol. Phys. 52 (1984) 255.

- 98) M. Parrinello, A. Rahman, *J. Appl. Phys.* 52 (1981) 7182.
- 99) R. Car, M. Parrinello, *Phys. Rev. A* 55 (1985) 2471.
- 100) M. Parrinello, *Comp. Sci. Eng.* 2 (2000) 22.
- 101) T.J. Raeker, A.E. DePristo, *Inter. Rev. Phys. Chem.* 10 (1991) 1–54.
- 102) V. Heine, L.J. Robertson, M.C. Payne, *Philos. Trans. R. Soc. Lond. A* 334 (1991) 393.
- 103) A.F. Voter, *MRS Bull.* 31 (1996) 17 (special ed.).
- 104) B.J. Garrison, D. Srivastava, *Annu. Rev. Phys. Chem.* 46 (1995) 373.
- 105) M.S. Daw, S.M. Foiles, M.I. Baskes, *Mater. Sci. Rep.* 10 (1993) 251.
- 106) M.S. Daw, M.I. Baskes, *Phys. Rev. B* 29 (1984) 6443.
- 107) B.J. Lee, M.I. Baskes, H. Kim, Y.K. Cho, *Phys. Rev. B* 64 (2001) 184102.
- 108) Y.F. Ouyang, B.W. Zhang, S.Z. Liao, Z.P. Jin, *Z. Phys. B* 101 (1996) 161.
- 109) M.W. Finnis, J.E. Sinclair, *Philos. Mag. A* 50 (1984) 45.
- 110) F. Cleri, V. Rosato, *Phys. Rev. B* 48 (1993) 22.
- 111) D.P. Yang, W.A. Hines, C.L. Tsai, B.C. Giessen, F.C. Lu, *J. Appl. Phys.* 69 (1991) 6225.
- 112) R. Delgado, H. Armbruster, D.G. Naugle, C.L. Tsai, W.L. Johnson, A. Williams, *Phys. Rev. B* 34 (1986) 8288.
- 113) H.W. Sheng, Y.Q. Cheng, P.L. Lee, S.D. Shastri, E. Ma, *Acta Mater.* 56 (2008) 6264.
- 114) J.C. Foley, D.R. Allen, J.H. Perepezko, *Scripta Mater.* 35 (1996) 655.
- 115) J.H. Li, Y. Dai, Y.Y. Cui, B.X. Liu, *Mater. Sci. and Eng. R* 72 (2011) 1.
- 116) J.D. Honeycutt, H.C. Andersen, *J. Phys. Chem.* 91 (1987) 4950.
- 117) A.S. Clarke, H. Jonsson, *Phys. Rev. E* 47 (1993) 3975.
- 118) C. L. Cleveland, W. D. Luedtke, Uzi Landman *Phys. Rev. B* 60 (1999) 5065.
- 119) M.Wakeda, Y. Shibutani, S. Ogata, J. Park, *Intermetallics* 15 (2007) 139.

- 120) Lagogianni AE, Almyras GA, Lekka ChE, Papageorgiou DG, Evangelakis GA. *J All. and Comp.* 483 (2009) 658.
- 121) J. Xia, J. Qiang, Y. Wang, Q. Wang, C. Dong. *Appl. Phys. Lett.* 88 (2006) 101907.
- 122) H. Tian, Ch. Zhang, L. Wang, J. Zhao, Ch. Dong, B. Wen, et al., *J. Appl. Phys.* 109 (2011) 123520.
- 123) T. Egami, Y. Waseda, *J. Non-Cryst. Solids* 64 (1984) 113.
- 124) G.B. Bokas, A.E. Lagogianni, G.A. Almyras, Ch.E. Lekka, D.G. Papageorgiou, G.A. Evangelakis, *Intermetallics* 43 (2013) 138.
- 125) G.B. Bokas, G.A. Evangelakis, Ch.E. Lekka. *Comp. Mater. Sci.* 50 (2011) 2658.
- 126) Ch.E. Lekka, A. Ibenskas, A.R. Yavari, G.A. Evangelakis, *Appl. Phys. Lett.* 91 (2007) 214103.
- 127) G.A. Almyras, Ch.E. Lekka, N. Mattern, G.A. Evangelakis, *Scr. Mater.* 62 (2010) 33.
- 128) G.A. Almyras, G.M. Matenoglou, Ph. Komninou, C. Kosmidis, P. Patsalas, G.A. Evangelakis, *J. Appl. Phys.* 107 (2010) 084313.
- 129) D.G. Papageorgiou, G.A. Evangelakis, *Surf. Sci.* 602 (2008) 1486.
- 130) J. Sakurai, S. Hata, A. Shimokohbe, *Japan. J. Appl. Phys., Part 1* 48 (2009) 025503.
- 131) E. Vasco, J.L. Sacedón, *Phys. Rev. Lett.* 98 (2007) 036104.
- 132) B.H. Huang, *J. Phys. D* 34 (2001) 3121.
- 133) L. E. Koutsokeras, G. Abadias, Ch.E. Lekka, G.M. Matenoglou, D.F. Anagnostopoulos, G.A. Evangelakis, P. Patsalas, *Appl. Phys. Lett.* 93 (2008) 011904.
- 134) JCPDS Powder Diffraction File No. 04-008-1477.
- 135) M. F. de Oliveira, G. A. Almyras and G. A. Evangelakis, Microstructural differences of amorphous  $\text{Cu}_{65}\text{Zr}_{35}$  between rapidly quenched and topologically destabilized crystalline Cu and Zr metals by Molecular Dynamics simulations, *Under Revision*.

- 136) C. Suryanarayana, *Mechanical Alloying and Milling*, Marcel Dekker Ed., New York, 2004.
- 137) A. C. Lund, C. A. Schuh, *Acta Materialia* 52 (2004) 2123.
- 138) Y.H. Liu, T. Fujita, D.P.B. Aji, M. Matsuura, M.W. Chen, *Nature Communications* 5:3238 (2014) 1.
- 139) R.S. Liu, K.J. Dong, J.Y. Li, A.B. Yu, R.P. Zou, *J. Non-Cryst. Solids* 351 (2005) 612.
- 140) R.S. Liu, H.R. Liu, K.J. Dong, Z.Y. Hou, Z.A. Tian, P. Peng, A.B. Yu, *J. Non-Cryst. Solids* 355 (2009) 541.
- 141) G. Rossi, A. Rapallo, C. Mottet, A. Fortunelli, F. Baletto, R. Ferrando, *Phys. Rev. Lett.* 93 (2004) 105503.
- 142) T. Takeuchi, S. Nakano, M. Hasegawa, K. Soda, H. Sato, U. Mizutani, K. Itoh, T. Fukunaga, *Mat. Sci. Eng. A* 449–451 (2007) 599.
- 143) J. Liu, J.Z. Zhao, Z.Q. Hu, *Mat. Sci. Eng. A* 452–453 (2007) 103.
- 144) X.D. Wang, S. Yin, Q.P. Cao, J.Z. Jiang, *Appl. Phys. Lett.* 92 (2008) 011902.
- 145) M. Matsuura, M. Sakurai, W. Zhang, A. Inoue, *Mat. Sci. Forum* 539–543 (2007) 1959.
- 146) D.B. Miracle, A.L. Greer, K.F. Kelton, *J. Non-Cryst. Solids* 354 (2008) 4049.
- 147) Y.Q. Cheng, A.J. Cao, H.W. Sheng, E. Ma, *Acta Mater.* 56 (2008) 5263.
- 148) A.A. Kundig, M. Ohnuma, D.H. Ping, T. Ohkubo, K. Hono, *Acta Mater.* 52 (2004) 2441.
- 149) N. Mattern, P. Jovari, I. Kaban, S. Gruner, A. Elsner, V. Kokotin, H. Franz, B. Beuneu, J. Eckert, *J. Alloys Comp.*, 485 (2009) 163.
- 150) D.B. Miracle, E.A. Lord, S. Ranganathan, *Mat. Trans.* 47 (2006) 1737.
- 151) X.D. Wang, Q.K. Jiang, Q.P. Cao, J. Bednarcik, H. Franz, J.Z. Jiang, *J. Appl. Phys.* 104 (2008) 093519.

- 152) K. Kodama, S. Likubo, T. Taguchi, S.I. Shamoto, *Acta Cryst. A* 62 (2006) 444.
- 153) V.I. Korsunskiy, R.B. Neder, A. Hofmann, S. Dembski, C. Graf, E. Ruhl, *J. Appl. Cryst.* 40 (2007) 975.
- 154) J.D. Bernal, *Nature* 183 (1959) 141.
- 155) S. Ranganathan, A. Inoue. *Acta Mater.* 54 (2006) 3647.
- 156) D.V. Louzguine-Luzgin, A.R. Yavari, G. Vaughan, A. Inoue. *Intermetallics* 17 (2009) 477.
- 157) M. Wakwda, Y. Shibutani, *Acta Mater.* 58 (2010) 3963.
- 158) Y.L. Sun, J. Shen, *J. Non-Crystal. Solids* 355 (2009) 1557.
- 159) G.A. Almyras, D. Papageorgiou, C. Lekka, N. Mattern, J. Eckert and G. Evangelakis, *Intermetallics* 19 (2011) 657.
- 160) N. Mattern, A. Schoeps, U. Kuehn, J. Acker, O. Khvostikova, J. Eckert, *J. Non-Cryst. Solids* 354 (2008) 1054.
- 161) D.V. Louzguine-Louzgin, K. Georgarakis, A.R. Yavari, G. Vaughan, G. Xie, A. Inoue, *J. Mater. Res.* 24 (2009) 274.
- 162) K. Georgarakis, A. Yavari, D.V. Louzguine-Luzgin, J. Antonowicz, M. Stoica, Y. Li, M. Satta, A. LeMoulec, G. Vaughan and A. Inoue, *Appl. Phys. Lett.* 94 (2009) 191912.
- 163) J. Antonowicz, A. Pietnoczka, T. Drobiazg, G.A. Almyras, D.G. Papageorgiou, G.A. Evangelakis, *Philos. Mag.* 92 (2012) 1865
- 164) J. Antonowicz, A. Pietnoczka, W. Zalewski, R. Bacewicz, M. Stoica, K. Georgarakis, A. Yavari, *J. Alloys Compd.* 509 (2011) S3437.
- 165) J.P.K. Doye, L. Meyer, *Phys. Rev. Lett.* 95 (2005) 063401.
- 166) A.R. Yavari, A.L. Moulec, A. Inoue, N. Nishiyama, N. Lupu, E. Matsubara, W.J. Botta, G. Vaughan, M.D. Michiel, A. Kvick, *Acta Mater.* 53 (2005) 1611.

- 167) Ch.E. Lekka, G.B. Bokas, G.A. Almyras, D.G. Papageorgiou, G.A. Evangelakis, J. Alloys and Comp. 536S (2012) S65–S69.
- 168) Ch.E. Lekka, G.A. Evangelakis, Scripta Mater. 61 (2009) 974.
- 169) Y.Q. Cheng, E. Ma, Prog. Mater. Sci. 56 (2011) 379.